Report
P-18-14
April 2019

Full-scale test of the Dome Plug for KBS-3V deposition tunnels – structural response of the concrete dome

NDT, FE-simulations and evaluation of measurements during the leakage and strength test

Richard Malm
Jonas Enzell
Manouchehr Hassanzadeh

SVENSK KÄRNBRÄNSLEHANTERING AB

SWEDISH NUCLEAR FUEL
AND WASTE MANAGEMENT CO

Box 3091, SE-169 03 Solna
Phone +46 8 459 84 00
skb.se

SVENSK KÄRNBRÄNSLEHANTERING

ISSN 1651-4416
SKB P-18-14
ID 1686601
April 2019

Full-scale test of the Dome Plug for KBS-3V deposition tunnels – structural response of the concrete dome

NDT, FE-simulations and evaluation of measurements during the leakage and strength test

Richard Malm, Jonas Enzell, Manouchehr Hassanzadeh
Sweco Energuide AB

Abstract

A full-scale test of the concept for sealing deposition tunnels, intended for the future spent nuclear fuel repository, has been performed at Äspö Hard Rock Laboratory (HRL) since 2013. The planning, installation and the initial operation was previously described by Grahm et al. (2015).

In the current project, the final tests of the dome plug have been performed before demolition. This phase of the project started where the filter was drained of water and a gas leakage test was conducted. After this, the filter was once again pressurized with a water pressure of 4 MPa and was held constant for about 1.5 months. After this, a strength test was performed were the water pressure was increased further so that a water pressure of about 8 MPa was reached. After the strength test was conducted, the pressure was reduced to 4 MPa again. About one month later, the filter was drained and the decommissioning of the plug started.

The purpose with this report is to present the results of the measurements in the concrete dome during the leakage test and strength test that was conducted between 1st of June to 30th of August 2017. In addition, the corresponding results based on numerical simulations are also presented in this report. Finally, the general conclusions from the non-destructive testing (NDT) are presented.

Four types of NDT were performed after the plug was unloaded: Ultra-sonic pulse-echo concrete tomography (MIRA), Ground Penetrating Radar (GPR), Impact Echo (IE), and Impulse Response (IR). Force Technology planned and executed all the non-destructive (ND) tests. The aim of these tests was to detect manufacturing defects such as cavities, honeycombing and material segregation. The ND tests did not reveal any manufacturing defects or cracks. However, it is not known whether the structure contained such defects or not, but no such defects where observed during core drilling and demolition. Therefore, it is not possible to conclude that any of the applied ND methods are able to reveal and locate the manufacturing defects. Although, there are indications that MIRA and GPR could reveal manufacturing defects, but it has not been proven that these are reliable methods for detection of manufacturing defects and cracks in this type of massive structure.

A large cavity was detected when cores were drilled out from the upper part of the concrete plug. The cavity was not detected during the NDT, but the area of the plug containing the cavity was never targeted. It is deemed unlikely that the cavity could have been detected even if it was targeted due to the limited range of the NDT-methods.

The concrete dome was instrumented with several sensors, most of them were embedded inside the concrete dome. The strain gauges, temperature sensors, and joint meters inside the concrete dome and the LVDT meters (measuring displacements) at the downstream surface was evaluated. One additional temperature sensor failed or malfunctioned during the strength test and that one of the joint meters was compressed to its limit. The measured results showed that the response of the concrete dome was in good agreement with the initial predictions with numerical analyses. Based on the measurements from the leakage and strength test, it could be seen that the sensors that measure the global behaviour, i.e. LVDT-sensors show differences before and after leakage or strength tests which indicates cracking in the dome. The sensors that measured the local behaviour varies to some extent before and after a variation in pressure, depending if they were close to areas with cracking or loss of bond. The strength test of the full-scale test was successful in proving that the dome concrete dome can withstand its theoretical design loads, without being subjected to significant cracking.

As a part of the pressurization test, finite element simulations (FE-simulations) were performed and analysed. The simulations indicated that loss of bond or cracking could occur during the lowering of the pressure, primarily at the top of the plug. The pressure used during the strength test was according to the numerical analyses, far from resulting in a potential failure. However, the analyses showed that there was a risk of limited cracking close to the top of the dome near the abutment in one of the simulations. The results from the FE-simulations were also compared with the measurements from the full-scale test. In general, the structural behavior of the FE-model coresponds well with the measurements, even though the material models lack nonlinearities. The comparison of strain between the measurements and the simulations indicates that cracking or loss of bond toward the edge of the dome occurred during the pressure test.

Sammanfattning

Sedan 2013 har ett fullskaletest genomförts i Äspölaboratoriet avsett att studera konceptet för försegling av depositionstunnlarna i ett framtida förvar för kärnavfall. Planeringen, installationen samt drifttagning beskrivs i Grahm et al. (2015).

I föreliggande projekt har ett sista test av pluggen utförts innan rivning. Testet utgjordes av att vattentrycket sänktes av och filtret dränerades i syfte att genomföra ett gastäthetstest. Efter detta, ökades återigen vattentrycket till samma nivå som innan gastäthetstestet, 4 MPa, och hölls konstant i ca 1,5 månader. Därefter utfördes ett hållfasthetstest, där vattentrycket ökades tillfälligt till 8 MPa. Efter hållfasthetstestet reducerades vattentrycket återigen till 4 MPa i ungefär en månad, varefter filtret dränerades och rivningen av pluggen inleddes.

Syftet med denna rapport är att presentera mätresultat från betongpluggen under läckage- och hållfasthetstestet som utfördes mellan 1 juni och 30 augusti. Resultat från FE-simuleringar och jämförelser av dessa med mätresultat kommer också att presenteras. Resultat från den oförstörande provningen kommer att sammanfattas och slutsatser angående detta presenteras.

Fyra olika oförstörande provningsmetoder utfördes i samband med gastäthetstestet: Ultra-sonic pulse-echo concrete tomography (MIRA), Ground Penetrating Radar (GPR), Impact Echo (IE), och Impulse Response (IR). Force Technology planerade och utförde alla oförstörande prover. Målet med de oförstörande proverna var att hitta eventuella produktionsfel såsom hålrum och materialseparation. Den oförstörande provningen hittande inga sprickor eller produktionsfel. Det är dock, inte är känt om några sådana fel existerade i betongen, men inga observationer avseende dessa typer av defekter kunde observeras vid kärnborrning och rivning. Det går utifrån dessa test därmed inte att avgöra om de oförstörande proverna kan upptäcka dessa typer av defekter eller ej. Det finns dock indikationer på att MIRA och GPR kan upptäcka sprickor och produktionsfel, men det har inte bevisats att dessa metoder är tillförlitliga för detta vid denna typ av massiva konstruktioner.

Under kärnborrningen upptäcktes ett stort hålrum i pluggens övre del. Hålrummet upptäcktes inte under den oförstörande provningen. Dock undersöktes aldrig området där hålrummet upptäcktes under den oförstörande provningen. Även om det området skulle ha undersökts anses det inte troligt att hålrummet skulle ha upptäckts på grund av mätutrustningens begränsade räckvidd.

Betongpluggen instrumenterades med ett flertal sensorer, de flesta var ingjutna i betongen. I den här rapporten utvärderas temperaturgivarna, töjningsgivarna, töjningsgivarna i övergången mellan berget och betongen, och LVDT-mätarna, vilka ger total nedströms förskjutning vid pluggens yta. Under hållfasthetstestet gick en temperaturgivare sönder samt en relativ förskjutningsgivare (i skarven mellan berg och betong) uppnådde sin maximala deformation. LVDT-mätarnas utslag visar på ökad förskjutning nedströms, både efter läckage- och hållfasthetstestet, en sådan förskjutning indikerar sprickbildning i pluggen. Vissa av töjningsgivarna indikerade sprickbildning, beroende på om de var nära ett område med sprickbildning eller förlorad vidhäftning. Hållfasthetstestet visade att pluggen kan motstå de dimensionerande lasterna utan att utsättas för signifikant uppsprickning.

Som en del av läckage- och hållfasthetstestet utfördes och analyserades finita elementsimuleringar (FE-simuleringar). Simuleringarna visade att sprickbildning skulle kunna uppstå eller vidhäftning förloras vid trycksänkningen, framförallt i pluggens övre del. Enligt de numeriska beräkningarna så var det vattentryck som användes under hållfasthetstestet långt ifrån att orsaka en potentiell brottmod i betongpluggen. Analyserna visade dock att det fanns viss risk för sprickbildning i pluggens övre del. Resultaten från FE-simuleringarna jämfördes också med mätningarna från trycktestet. Pluggens beteende i simuleringarna stämmer väl överens med det verkliga beteendet, trots att materialmodellen saknar olinjärt beteende. Jämförelsen mellan mätningar och simuleringar i töjningsgivarna indikerar att sprickbildning mot pluggens kanter eller förlorad vidhäftning mellan berget och betongen uppstod vid läckage- och hållfasthetstestet.

Contents

1 Introduction

1.1 Background

A full-scale test of the concept for sealing deposition tunnels in the future repository has been performed at Äspö Hard Rock Laboratory (HRL) since 2013. This project has previously been described by Grahm et al. (2015).

The plug consists of several material layers, each with its specific purpose, see Figure 1-1. The main parts of the plug are; filter, bentonite seal and a concrete dome. The filter is needed to control ground water inflow during casting and hardening of the concrete dome through drainage pipes. The bentonite seal is intended to be the water-tight seal of the plug and thereby prevent that leakages occur from the backfilled deposition tunnel to the adjacent main tunnel. The concrete dome constitutes the mechanical resistance intended to transfer the loads from swelling pressure of bentonite and the hydrostatic water pressure to the surrounding rock. The concrete dome is unreinforced and built with a specially developed concrete mix that is intended to have a lower pH than conventional concrete, see Vogt et al. (2009) for more information regarding the concrete mix. Between these material layers, different delimiters are installed only to separate the materials. The delimiter closest to the concrete dome consists of concrete beams.

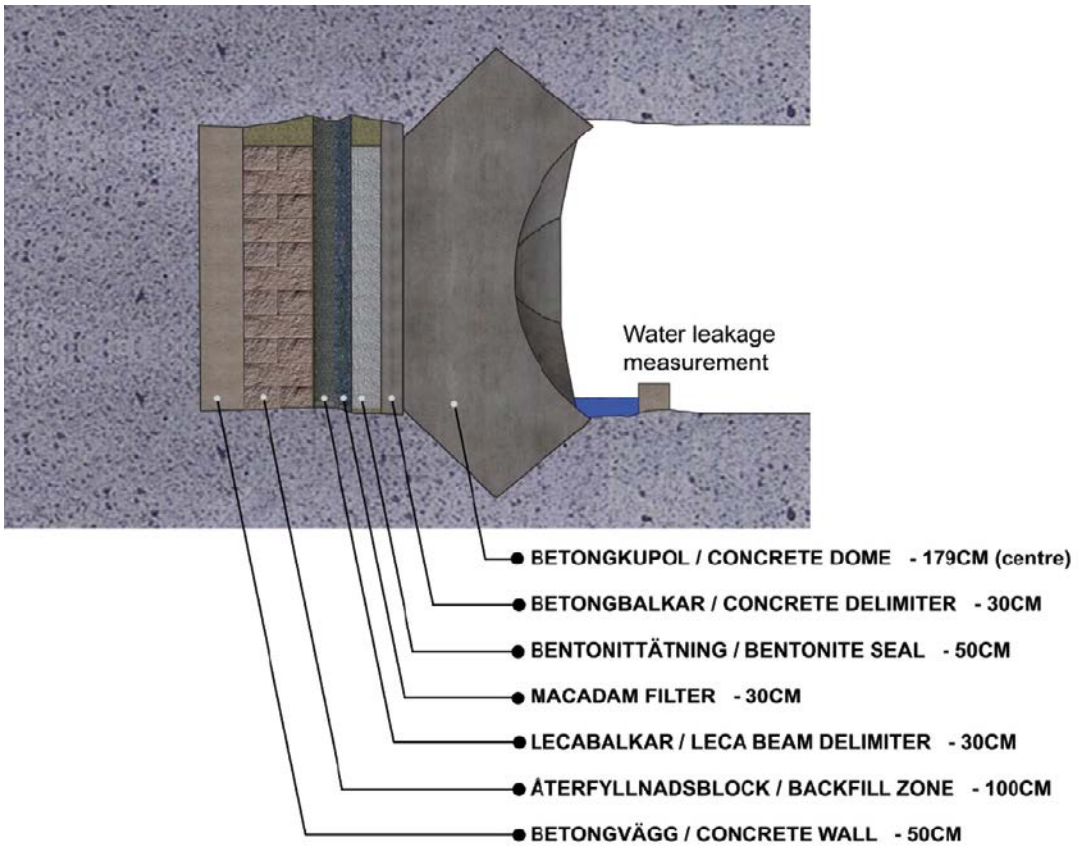

Figure 1-1. *Illustration of the plug used in the full-scale test.*

The cement reactions during the early age hydration process results in increasing temperature within the concrete. Due to the increasing temperature, the concrete starts to expand and at the same time hardens. In later stages, the rate of the cement reaction and corresponding heat development decrease when it starts to adapt to the ambient temperature of its boundaries which leads to contraction of the concrete. The cement reactions also lead to autogenous shrinkage which to some extent can be added to the contraction of concrete during cooling. The autogenous shrinkage and contraction due to cooling may together or alone lead to a gap between the concrete dome and the rock. If the displacement of the concrete is prevented, cracks may appear in the concrete and/or in the concrete-rock interface. A gap between the concrete dome and the rock is not desirable because it may lead to leakage.

Cooling pipes were installed in the concrete dome to control the concrete temperature during hardening and thereafter to cool down the hardened concrete to force it to release the rock. The continued cooling after hardening would allow a gap to be completely developed between the dome and the rock. After development of the gap, the gap was injected while the concrete was kept cooled. After the hardening of the grout, the cooling system was shut down to allow the concrete to gain thermal equilibrium with its surroundings.

Theoretically, the described process would lead to the formation of a gap of up to 4 mm in certain places (especially in the higher sections) between concrete and rock. It would facilitate the injection of the grout and make it easier for the grout to fill the gap. After hardening of the grout, the hardened expanding concrete would induce compressive stress on the hardened grout.

The purpose of the full-scale test was firstly to verify that the installation could be made and to ensure that it was possible to build the plug according to the design specifications. In addition, the purpose was also to evaluate that the design acted as expected during hardening of concrete and homogenization of the bentonite seal but also during the serviceability state when it is subjected to hydrostatic pressure. Finally, the purpose was also to estimate the water tightness of the plug.

In this project, the final tests of the dome plug have been performed. This phase of the project started where the filter was drained of water and a gas leakage test was conducted. After this, the filter was once again pressurized with water pressure of 4 MPa and was held constant for about 1.5 months. After this a strength test was performed were the water pressure was increased further so that a water pressure of about 8 MPa was reached. After the strength test was conducted the pressure was reduced to 4 MPa again and then about one month later, the filter was drained and the decommissioning of the plug started.

1.2 Purpose

The purpose with this report is to present the results for the concrete dome during the leakage test and strength test that was conducted between 1st of June to 30th of August 2017. This includes presenting the measured results from the sensors embedded in concrete and mounted on the dome during this period. In addition, the corresponding results based on numerical simulations are also presented in this report. Finally, the general conclusions from the non-destructive testing are presented. This report thereby aims to describe parts of the work that has been performed within the KBP1006 project at Äspö HRL.

2 Non-destructive testing (NDT)

2.1 Introduction

The concrete dome is a massive and thick concrete structure. The concrete mix of the concrete dome was carefully designed to achieve low heat development during hydration and low pH and autogenous shrinkage after hardening. Due to the boundary conditions of the concrete dome drying shrinkage is not expected to occur during the life-lime of the structure. The concrete dome is unreinforced, but contains cooling pipes made of copper. The concrete dome contains also cables connected to measuring devices, which were placed in the form before casting. When using non-destructive testing methods, it is important to remember that all these embedded materials may affect the possibility to see into the concrete dome.

The concrete mix was designed to have good casting properties and the casting proceeded smoothly. No defects such as honeycombing, settlement cracks or segregation of the mix constituents were expected.

The aim of a Non-Destructive Test (NDT) series should be assessment of the execution of work such as detection and quantification of the defects, which may occur during casting, cooling to create the gap, injection of grout and stopping the cooling to let the concrete dome to gain thermal equilibrium with its environment. A thorough non-destructive examination of the concrete dome structure should contain following parts as shown in Figure 2-1:

A) Characterization of the gap between the concrete dome and the rock. The aim should be
   – to detect areas with poor contact between the concrete dome and the rock,
   – to detect areas with not sufficiently filled gaps and,
   – distinguish between water filled (leaking parts) and dry parts of the gap.

B) Calculations indicate that a crack plane occurs at relatively high pressures inside the dome. The approximate location of the crack is shown in Figure 2-1. In cases where the bearing capacity and tightness of the dome is tested, the existence of such a crack should be verified by NDT.

C) At the abutment surface, the concrete dome presses against the rock. The pressure can cause stresses and cracks in the both concrete dome and the rock. The cracks may be formed both parallel and perpendicular to the transition zone between the concrete dome and the rock. In cases where the concrete dome's bearing capacity and tightness is tested, the existence of the cracks should be verified by NDT.

D) Manufacturing defects such as cavities, honeycombing and material segregation that may occur during production. The existence of the manufacturing defects should be verified by NDT.

E) Location of cooling pipes and the quality of the concrete around the pipes should be determined by means of NDT.

The NDT methods which were available can be divided in following groups:

- Ultra-sonic pulse-echo concrete tomography, MIRA.
- Ground Penetrating Radar, GPR.
- Impact Echo, IE.
- Impulse Response, IR.

All instruments based on the above-mentioned principles are to some extent able to detect the defects/details presented in Figure 2-1. However, the specific shape and rather large thickness of the structure limit the ability of the instruments to detect the defects/details shown in the figure. Concrete limits the penetration of the waves by consuming their energy. Therefore, it is difficult for the waves to penetrate deep into concrete. Since, the consumption of the energy increases with decreasing wave length, it is more difficult for waves with short wave length to penetrate the concrete in comparison with waves with larger wave length. Therefore, the resolution performance of the instruments decreases with increasing depth since the resolution decreases with increasing wave length.

In the tests which are presented in Kristensen (2018), the target was to detect Type D defects presented above, i.e. "*Manufacturing defects such as cavities, honeycombing and material segregation that may occur during production*". The other types of defects/details were disregarded.

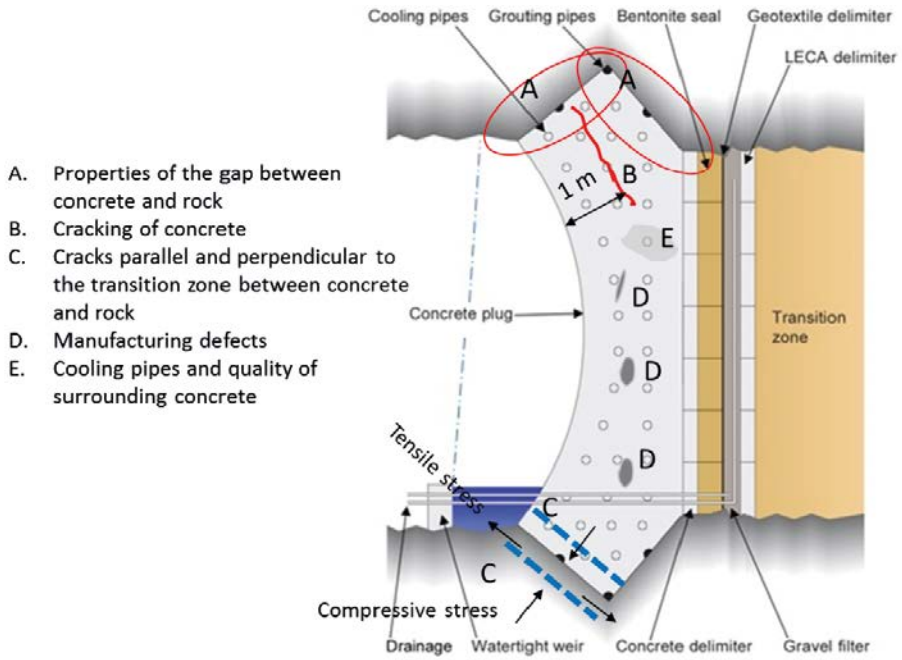

Figure 2-1. *Summary of events and their location on the concrete dome.*

Force Technology planned and executed all the NDT referred in this section. All results including method descriptions are presented in the Force Technology's report, Kristensen (2018). This section presents a summary of the Force Technology's report including a few comments made by the author of this section and method descriptions from other literature sources.

It should be noted that a rather large cavity was detected when cores were drilled out from the upper part of the concrete plug, Figure 2-2. Preliminary investigation indicated that the cavity was caused by the fact that the mould was not top filled. The photograph in Figure 2-2b is taken inside a Ø 150 mm bore hole ending in the top of the plug. The cross section of the cavity is almost triangular with a base edge on the concrete and two side edges, whereas one on the downstream face and the other one on the upstream face of the rock slot respectively. The height of the cross section was approximately 0.20 m. The cavity was extended along with the upper edge of the concrete plug.

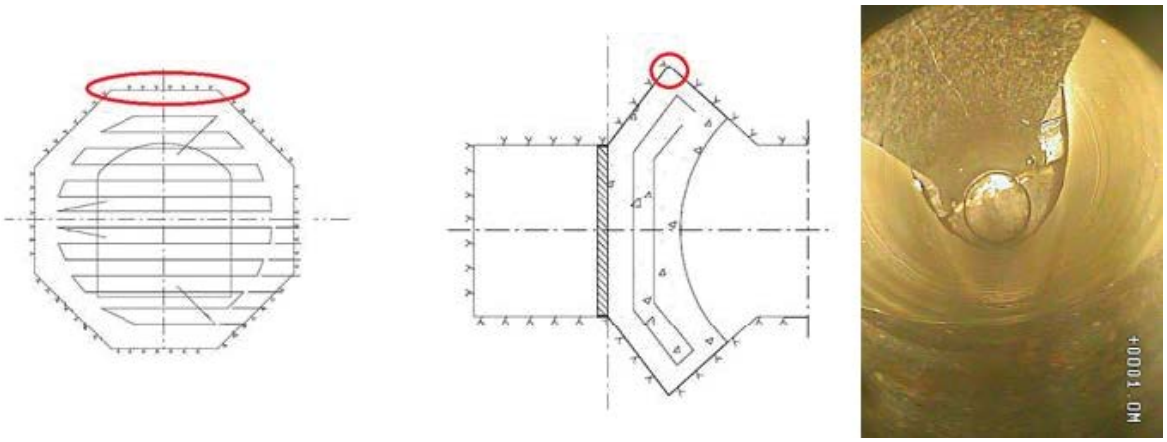

a) Location and the extension of the cavity between the concrete plug and the rock on the top of the plug. The height of the triangular formed cross section of the cavity was 0.2 m and it was extended along with the upper side of the plug.

b) The photograph is taken inside a bore hole ending in the top of the section shown in a).

Figure 2-2. *The cavity between the concrete plug and the rock.*

As it is mentioned above the area where the cavity was detected, was not targeted during the NDT-examinations. Although, cavities were searched in the mass of the plug, no attentions were payed to neither the areas close to the edges of the plug nor to the transition zones between the concrete and the rock. However, the following questions have been raised:

- Could the cavity be detected if the area was targeted during the conduction of NDT?
- If the answer is no, what are the reasons?
- Is the disability of the NDT to detect the cavity, due to the geometry of the plug?
- Is the disability of the NDT to detect the cavity, due to NDT methods?
- Is it possible to modify the existing methods such that similar defects could be detected?

Those who performed the NDT has addressed the questions afterwards. Their comments with some modifications are given below:

- The area is more or less impossible to inspect with NDT. The defect is located in a depth of 2 meters. In this depth the inspection wave is not concentrated in a focus spot. It is more an average of a wide area. The best reflections from defect are when measurements are made in the area around the defect. With this kind of defect, measurements can only be made in front and not directly over the defect or behind/past it. When getting close to an edge of a plate reflections from the side of the plate may be received as well. Hence, it will be difficult to determine whether the reflections are from a defect or a from the sides of the plate. In this case neither the location of the cavity nor the geometry of the structure have been advantageous for the measurements.
- It is not easy if not impossible to detect this kind of defects by means of NDT method. Hence, it will not matter if the area was targeted during testing. Furthermore, 3–4 pipes were coming out from the interface in the top making it difficult to get access to the area of interest.

2.2 Summary of used methods

2.2.1 Ultra-sonic pulse-echo concrete tomography, MIRA

The ultra-sonic pulse-echo tomography was performed by the instrument A1040 MIRA concrete tomographer. The instrument consists of 4 × 12 individual transducers. The transducers are capable to transmit and receive ultra-sonic pulse echo. The transducers are spring loaded to conform to an irregular surface. The transducers do not need any coupling medium and can be operated in dry conditions (Kristensen 2018).

The transducers can introduce pressure and shear stress-wave pulses. In this case shear waves pulses, within an adjustable range of nominal center frequency of 25 to 85 kHz, were used. The pulse is composed of waves with different frequencies. The center frequency is the main wave, which has the highest amplitude. For instance, a pulse with the center frequency of 50 may be composed of waves with frequencies ranging from a few kHz up to 100 kHz. At a given amplitude, the waves with lower frequency penetrate deeper than the waves with higher frequencies, but the resolution of the instrument decreases with decreasing frequency (Germann Instruments 2018).

As it was mentioned above, MIRA's transducers are arranged as 4 rows × 12 columns matrix. When MIRA is used for scanning, the columns are oriented in the direction of the scanning line. During the scanning, the MIRA is placed on the predefined points along with the scanning line. At each point a row of transducer (4 transducers) acts as a transmitter, i.e. they introduce stress-wave pulse, while the other 11 transducers receive the reflected pulses. The time from start of the pulse until arrival of the echo is measured. If the speed of the wave is known the location/depth of the reflecting surface can be calculated. At each point the transmitting column of transducers are shifted from column 1 to column 11, i.e. 11 columns consisting of 4 transducers will (one by one) introduce shear wave pulses. Totally 66 ray paths are involved during a measurement at one test location (a scanning point). It takes less than 3 seconds to complete data acquisition and data processing at each location (Germann Instruments 2018).

The measurement at the test location (under the antenna) in combination with a specific signal processing technique gives a 2-D image of the reflecting interfaces in the region below the antenna. By repeating the measurements along with several parallel (equidistant) scanning lines and data processing

with a 3-D visualization software a 3-D image of the structure can be produced. The 3-D image shows the detected defects, damages, cast-in details, etc. For detailed description of the method, its applications and limitations, the reader is referred to Germann Instruments (2018) and Kristensen (2018).

Figure 2-3 shows an example of a MIRA 3-D model. Consider the illustration to the right in the figure. The scanning lines are directed in the direction of the X-axis. The MIRA is placed as it is shown on a scanning line and moves from one location to other in the X-direction. The measurement takes place at each location. After completed test and processing, "*a B-scan provides an 'end view' of the reflectors. The B-scan views are the same images created at each test location by the MIRA. The D-scan provides a side view of the reflectors. The user can look at specific 'slices' through 3-D model by defining the Z-coordinate for a C-scan image, the Y-coordinate for a B-scan image, and the X-coordinate for a D-scan image"* (Germann Instruments 2018).

2.2.2 Ground Penetrating Radar, GPR

Ground Penetrating Radar (GPR) applies similar principles as MIRA. The major differences between MIRA and GPR are that GPR uses a high frequency radio signal (electro-magnetic waves) and that the GPR antenna do not need to be in contact with the surface of the object. The antenna unit includes both transmitting and receiving devices. When the radio waves penetrate a material, they continue to travel inside the material until they meet areas, surfaces or details with dielectric constants differing from the mass material. The greater the difference between the dielectric constants the greater the reflection of the waves. "*The dielectric constant is a measure of the capacity of a material to store charge when an electric field is applied. The dielectric constant of concrete is between 4–11. Air has a constant of 1 and water one of 81. The dielectric constant of metals is infinite.*" (Kristensen 2018). Therefore, the metals cast in concrete can be detected by GPR and concrete cover protecting the reinforcement can be measured. However, delamination's, honeycombing and cracks are difficult to detect when they are dry due to the low difference between the dielectric constants of concrete and air. Water filled delamination, honeycombing and cracks can be detected more easily. The thickness of a concrete element can be measured when the rear surface of the element is in contact with water or other materials with differing dielectric constant.

The ability of the radio waves to find and locate the embedded materials and defects in concrete depends on the depth and the size of the detail, and the frequency of the wave. The smaller the embedded material or defect is, the higher frequency is needed. The deeper the material is located; the lower frequency must be used to penetrate to the required depth. Therefore, the resolution of the method decreases with decreasing size and increasing depth of the imbedded material or defect. In practice, different antenna frequencies are used. In this project antennas with frequencies of 400 MHz, 900 MHz, and 1 600 MHz have been used.

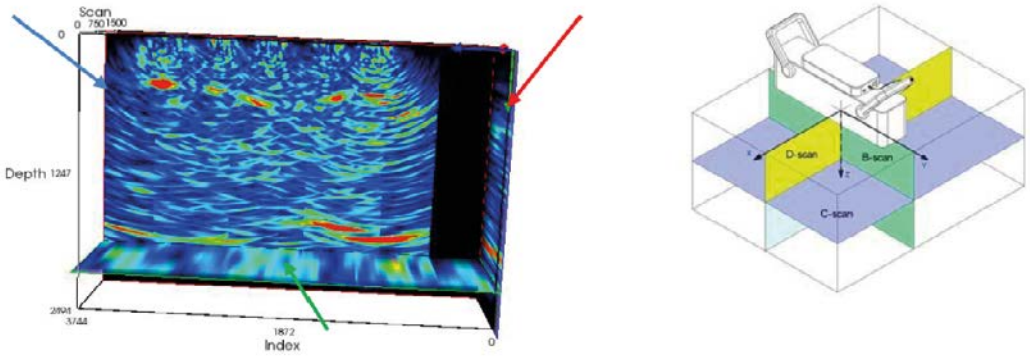

Figure 2-3. *To the left, an example of a MIRA 3-D model shown as 3 slices in the model. XY plane (blue arrow) is called B-scan. YZ plane (red arrow) is called D-scan and XY plane (green arrow) is called C-scan. This is also illustrated in the figure to the right, but with the difference that a horizontal antenna position is used, hence the difference in B/D-scan terminology, figure and figure text are from Kristensen (2018).*

Figure 2-4 shows a B-scan produced by a 400 MHz antenna at the middle of the dome. A B-scan is composed of several measurements along with a line. The illustration of the right side of the Figure 2-4 shows the principle of detecting and locating a reinforcing bar.

The GPR scanning is performed through B-scanning of the object's surface. The B-scan lines are normally parallel to the X- and Y-axis of the object's surface. By composing the B-scans a C-scan image, 3-D image, is created. The C-scan shows the imbedded details' and defects' location in the mass material.

2.2.3 Impact Echo, IE

The Impact Echo (IE) method is based on use of transient stress waves generated by an elastic impact (Sansalone and Streett 1998). The elastic impact produces a short duration mechanical pulse, which generates stress waves. The stress waves travel through the material and are reflected back and forth by the flaws, boundaries of the structure, the imbedded materials or other detectable imperfections several times. These multiple reflections generate transient resonances, which can be related to the flaws, boundaries or cracks through amplitude versus frequency relations (spectra). The spectrum is produced by transforming the recorded surface displacement versus time function. The displacement normal to the surface is recorded by a transducer placed adjacent to the impact location.

The difference between IE and MIRA is that in IE the stress waves are produced by an impactor, while in MIRA the stress waves are produced by a transmitter. Furthermore, in the application presented in section 2.2.1 the displacement is in plane (shear) displacement, while in the IE the displacements are normal to the surface.

The typical wave lengths in IE applications are between 0.07 m and 2 m according to Kristensen (2018). The wave lengths of the stress waves generated by the impact is larger than the constituents of concrete, i.e. regarding the application of IE concrete can be considered as a homogenous material. Assuming a wave speed of 4 000 m/s the above-mentioned wave lengths correspond to 43 kHz and 2 kHz. The mentioned frequencies should be compared with MIRA's nominal center frequency of 25 to 85 kHz.

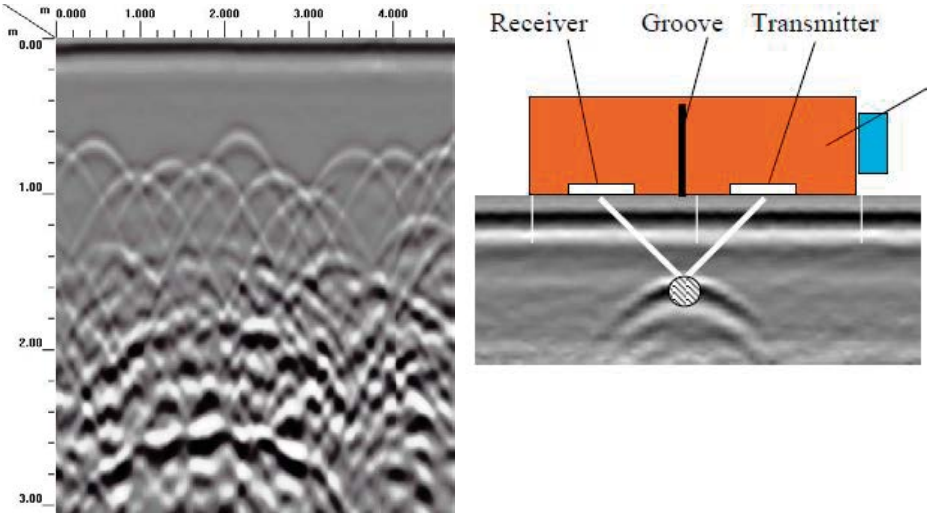

Figure 2-4. *To the left, example of B-scan made with 400 MHz antenna at the middle of the dome, from bottom to top. Horizontal scale is length of B-scan and vertical scan is depth to reflection. To the right is illustration of an antenna detecting a metal object. Figure and text from Kristensen (2018).*

The diameter of the impactor has big influence on the contact time between the impactor and the surface. Small diameter leads to short contact time, which leads to higher wave frequencies and lower penetration depth. For the concrete dome construction with a thickness of 1.8 m, a frequency of 1.11 kHz is needed to make it possible for the wave to travel to the end of the structure and back. To produce a wave with a frequency of 1.11 kHz, an impactor with a diameter of 200 mm is needed, which is not practical. In the application within this project, an impactor with the diameter of 50 mm and weight of 1 kg was used. The theoretical contact time between the impactor and the surface was 215 ms. The maximum applicable frequency and the minimum detection depth were 4.7 kHz and 430 mm respectively (Kristensen 2018).

Another important factor in IE applications is the ratio between the width of the anomaly and the depth to the anomaly. The ideal condition is when the ratio is greater than 1.5. If the size of anomaly is small compared to the depth it does not reflect sufficient energy to set up a resonance condition related to its depth (Kristensen 2018).

The IE tests are performed on the surface at predefined intersection points of a 500 mm × 500 mm grid. The results are presented as e.g. contour plot showing the dominant frequencies.

2.2.4 Impulse Response, IR

The method is based on measurements of the mobility plot, which shows the mobility ((m/s)/N) of the surface versus frequency. The mobility is the ratio of the velocity of the surface to applied force. The force is applied by a sledgehammer with a built-in load cell. The movement of the surface is recorded by a velocity transducer (geophone). The impact generated by the sledgehammer and the velocity are recorded by a datalogger. The result is transformed to a mobility plot as shown in Figure 2-5.

The IR is performed on surfaces with predefined grid. The average mobility is determined at each intersection point of the grid and the results are presented as a contour plot.

According to Kristensen (2018); "*The IR examination cannot be used alone to evaluate a concrete structure. The method is primarily considered a relative method used for screening of large surfaces. The method does not give exact responses in each point that can be compared to guidelines. The response in each point should instead be compared to the remaining points tested at the structure*."

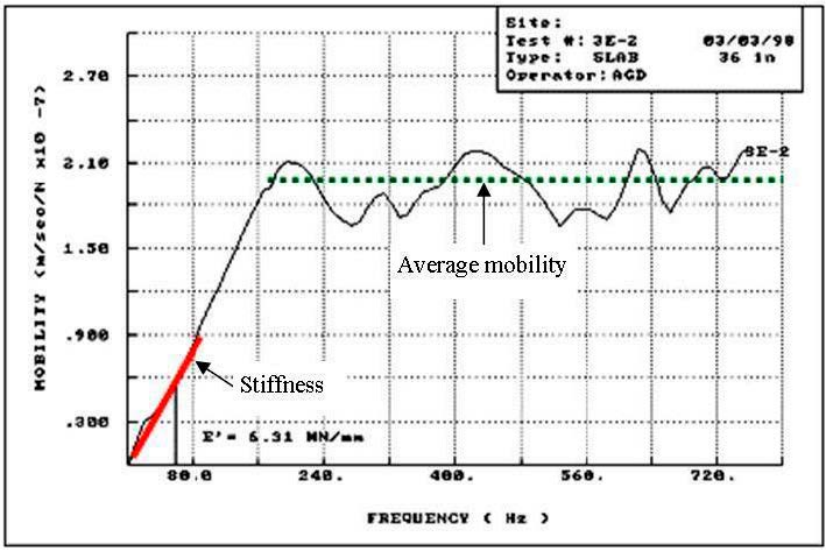

Figure 2-5. *Example of mobility plot from an IR test, from Kristensen (2018).*

2.3 Results

2.3.1 General

The execution of tests and results are thoroughly presented and discussed by Kristensen (2018). In this section, only samples of results including the Force Technology's comments and conclusions are presented.

2.3.2 Ultra-sonic pulse-echo concrete tomography, MIRA

A sample of results is presented in Figure 2-6. As can be observed the ultra-sonic pulse-echo has penetrated the concrete dome and has been reflected back. The solid red line in the figure indicates the rear surface of the structure. The ultra-sonic pulse-echo located the cooling pipe zone as well, dashed red line. No defects, cracks, honeycombing have been detected. It has been concluded that if such anomalies were existed, they could have been detected. There are also some results which show reflections from the concrete/rock interfaces in the rear part of the concrete dome. The results indicate that the waves can penetrate deep into the structure and be reflected from its boundaries. The results, however, do not reveal any anomalies, or can characterize the condition of the boundaries.

Some of the lesson learned and conclusions as they appear in the report of Force Technology are given below:

Performance

- The test has shown that it is possible to penetrate the full thickness of the concrete dome.
- It is possible to roughly locate the position of the rack and the cooling pipes.
- It is possible to roughly locate the transition between reflections from the concrete dome/membrane and the concrete/rock interface on the upstream side of the dome. In some cases, there is a difference in the density of the reflection and in other cases that transition zone can only be noticed due to the physical change in the concrete dome geometry.

Challenges

- The geometry of the exposed surface of the dome complicated the interpretation of the data.
- The contact surface between the MIRA and the concrete must be as good as possible to obtain quality data, especially for the deep parts.
- The spacing/density of the data points of great importance, especially with regards to the deeper objects. A spacing of 500 mm × 500 mm is not sufficient to reveal finer variations and to compensate for statistical variations in the processing software.
- A sufficient spacing in the given structure would have to be about 100 mm × 100 mm.

Defects

- The physical principle in the MIRA system utilizes shear waves. Shear waves cannot penetrate air or liquid filled cracks. Since no distinct reflectors have been observed, that prevents signals from underlying structures to be detected, it is the conclusion that the concrete dome is intact.

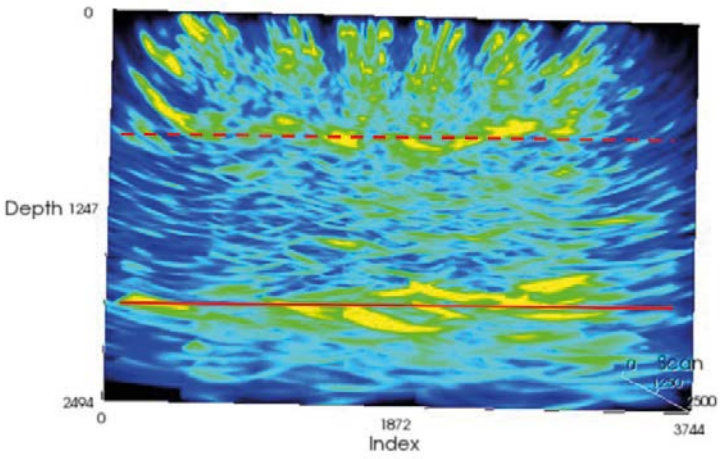

Figure 2-6. *A B-scan (X/Z plane). Indication of backside reflections may be seen at a depth of 180–205 cm (red line). The cooling pipe zone may be seen at a depth of 70–75 cm (red dashed line). Figure and text from Kristensen (2018).*

2.3.3 Ground Penetrating Radar, GPR

The radio waves have been able to penetrate the concrete. As expected, the lower frequency the deeper penetration. Figure 2-7 shows B-scans with three different frequencies. The lowest frequency could penetrate deep and through the structure to reveal its boundary and details behind that. In the result of the 400 MHz antenna the hyperbola at the depth 180–220 cm is the reflection from the upstream side of the dome where a geotextile is installed. The hyperbola at the depth 250–300 cm is the reflection from the second geotextile. Even 900 MHz frequency wave could penetrate deep, but not as deep as 400 MHz frequency, into the structure and reveal the upstream side of the dome. The resolution obtained by the 900 MHz frequency was better than that of 400 MHz frequency. The 1 600 MHz frequency could not penetrate as deep as the other frequencies.

Figure 2-8 shows a C-scan of a part of the dome. As it is observed in figure the GPR is able to reveal the cooling pipes which are embedded in the concrete. The pipes are, however, reflected in the curved form, which is not the case. It has been explained: "*The reason for the curved form is a change in concrete cover to the cooling pipes. The measured cover to the cooling pipes might also be affected by the curve of the dome. The breaks in the pipes in the C-scan, where the concrete cover decreases is where the cooling pipes bend, as seen in the picture to the right in the figure above.*" (Kristensen 2018).

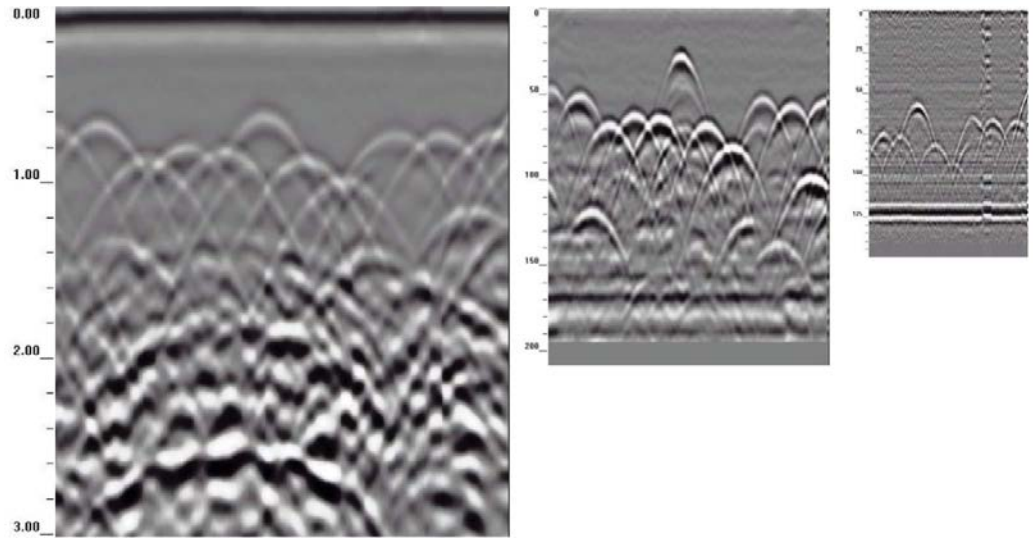

Figure 2-7. *Examples of scans made during test of different antennas. From the left: 400 MHz, 900 MHz and 1 600 MHz. Figure and text from Kristensen (2018).*

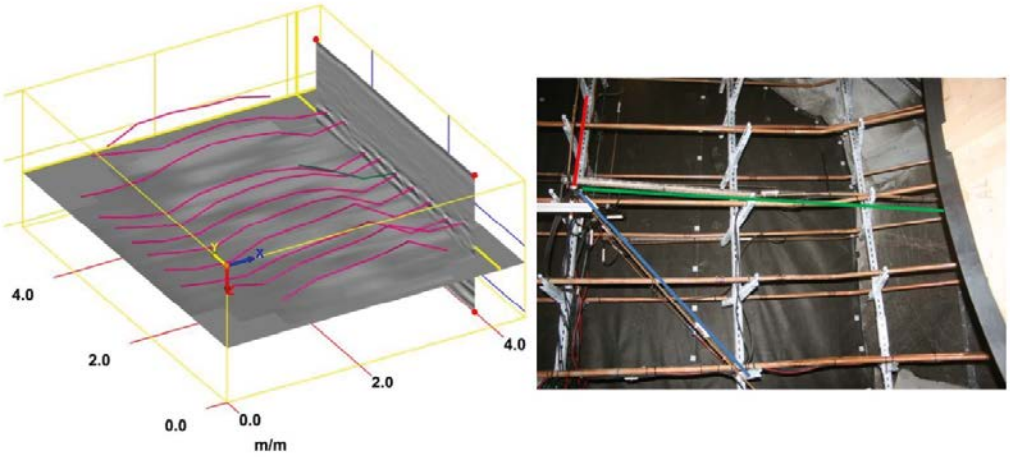

Figure 2-8. *To the left. C-scan of vertical scans, seen from the side. To the right, a picture of cooling pipes and 3 extra small pipes, probably for cabling and monitoring. Figure and text from Kristensen (2018).*

Some of the lesson learned and conclusions as they appear in the report of Force Technology are given below:

Performance

- Testing of the whole concrete dome in a 50 × 50 cm grid with the 900 MHz antenna took roughly 3–4 hours as it took time to position the lift correctly in order to make straight unbroken scan lines in the full height or width. Scanning in the dense area took roughly 3 hours including small breaks in the measurements to rest, as the antenna and survey wheel is heavy.
- Test with a 400 MHZ antenna has shown that it is possible penetrate the full thickness of the concrete dome and get a clear reflection from the backside.
- It is possible to locate the position of the supporting rack profiles and the cooling pipes, both with 400 and 900 MHz antennas.
- It is possible to locate the transition between the tunnel and the rock wall on the upstream side of the dome. The reflections are clearest at the sides and top.

Challenges

- The geometry of the exposed surface of the dome complicated the interpretation of the data, especially when looking at a C-scan with B-scan lines in two directions perpendicular to each other.
- The contact surface between the survey wheel on the antenna and the concrete must be as good as possible to obtain a proper position of the data, which affects the straightness of reflections in the C-scan but also the possibility of pointing out anomalies in the physical structure after data analysis. It has proven difficult to drag the antenna along the surface with the used type of survey wheel as the equipment is heavy. A lighter survey wheel should be used and if possible, a more automated scanning device.

Defects

- No reflections have been observed from any form of anomalies, and therefore it is the conclusion that the concrete dome is intact.

2.3.4 Impact Echo, IE

The IE tests conducted during this work have not verified the applicability of the method to structures such as the concrete dome. Therefore, no examples of the results will be given in this section. However, the reader is referred to Kristensen (2018) for detailed information about the results. Some of the lesson learned and conclusions as they appear in the report of Force Technology are given below:

Performance

- The coarse grid test on the whole structure per 50 × 50 cm took approximately 1–2 hours.
- The test has shown that it is very difficult to get a strong and clear reflection from the backside of the structure.
- It was not possible to use an automated Impact Echo scanner.

Challenges

- When impacting the dome, it was noted that the ball hammer left deep marks in the surface. It is believed that the outer part of the dome might be a bit soft, which will affect and dampen the impact.
- If the IE method is to be applied in the future, an effort should be made to find a transducer that has a lower resonance frequency. Further tests with larger diameter balls should be made.
- If the above challenges with the transducer and impactor are solved, a finer grid should be used to get a more detailed 2-D contour and to rule out some of the points that contain too much noise.

Defects

- No anomalies were detected with the impact echo method. It should however be kept in mind that in order to be able to detect the anomalies, they need to be fairly large.

2.3.5 Impulse Response, IR

The IR tests conducted during this work have not verified the applicability of the method to structures such as the concrete dome. Therefore, no example of the results will be given in this section. However, the reader is referred to Kristensen (2018) for detailed information. Some of the lesson learned and conclusions as they appear in the report of Force Technology are given below:

Performance

- The test has shown that it is possible to scan the dome relatively fast. The test time was approximately 1 hour.
- The test gives good results for all the analyzed parameters. There are no areas that are clearly distinct from the rest of the dome.
- The test was not affected by the surface as in the case of the IE measurement. The tip of the sledgehammer is flat and did not leave marks in the surface.

Challenges

- No tests have been performed on similar structures in the past, and therefore no comparison can be made between different domes. If the test is used in the future, it would be easier to make an interpretation of the result when the response for more domes can be compared.

Defects

- No anomalies were detected with the impulse response method. The literature does not contain much information on the size of defects that are possible to detect with the IR method. It is assumed that the defects should be large in order to affect the mobility of the structure. Especially if the defects are deeper in the domes.

2.4 Conclusions

As it was stated in Section 2.1, the target of the tests was to detect manufacturing defects such as cavities, honeycombing and material segregation. The NDT results presented in this chapter Kristensen (2018) didn't reveal any manufacturing defects or cracks. It is not known whether the structure contains such defects or not. Therefore, it is not possible to conclude that any of the applied ND methods are or are not able to reveal and locate the manufacturing defects. Although, there are indications that MIRA and GPR could reveal manufacturing defects, it has not been proven that they are reliable methods for detection of manufacturing defects and cracks.

The conclusions stated in Kristensen (2018) are presented.

Based on measurements carried out with the following non-destructive test methods:

- Ultra-sonic concrete tomography, MIRA.
- Ground Penetrating Radar, GPR.
- Impact Echo, IE.
- Impulse Response, IR.

It is concluded that:

- No anomalies have been detected in the concrete which could indicate that the dome should contain any large defects such as delamination, voids or honeycombing. It should be noted that the size of defects should increase with increasing depth to be able to detect them.
- There is an indication in both MIRA and GPR measurements that there might be a slip between the dome and the rock, especially observed at both sides of the dome.
- A combination of data from MIRA and GPR provides good information of the quality of the concrete and the position of embedded parts.
- IR is good for a fast scan of the dome, but due to the lack of data from a reference case the interpretation of the data is difficult.
- IE has not been found to give good and conclusive results. Primarily due to the limitation of the method on thick structures, but also due to the surface of the concrete dome.
- Data collection on the dome has been time consuming, and it has been difficult to obtain quality data with a high position accuracy, especially for GPR measurements. The data collection requires a large boom lift and two inspectors. The alternative could be an industrial robot arm, capable of reaching the entire dome surface. The equipment should be modified to better suit the geometry and challenges at the surface.

3 Measurements

3.1 Summary of installed sensors

The concrete dome was instrumented with several sensors, most of them were embedded inside the concrete dome. Some sensors were only used for a shorter period, such as measuring the pressure on the formwork, while the others were used to monitor the behaviour from the hardening process and continued for about five years.

The different types of recordings were; temperature in the concrete dome and the ambient air, strain in the concrete dome, displacement sensors measuring the displacement of the dome and the joints between concrete and rock. In total, the response of the concrete dome was measured 62 with recorded signals where the following types of sensors were used:

- 5 Pressure sensors (Wika S11) – pressure on the formwork.
- 6 Joint meters (TML type KJA-A) – relative displacement between concrete and rock.
- 3 LVDT (HBM type WA) – displacement of the concrete dome.
- 14 Strain gauges (TML type KM-AT) – strain and temperature in the concrete dome.
- 10 Strain gauges (TML type KM-A) – strain in the concrete dome.
- 4 Strain gauges (Geokon 4 200) – strain and temperature in the concrete dome.
- 2 Temperature sensors (PT 100) – ambient air temperature.

In Figure 3-1, a photo of installed strain gauges and cooling pipes is shown in addition to a sketch illustrating the placement of sensors.

The installation of the sensors and the equipment used has been described in detail by Malm (2015a) and the measured results from installation up to the point where this project started have previously been reported in Malm (2015a, b, 2016, 2017). The instrumentation and previous measured result are also summarized in the report by Grahm et al (2015).

In this report, the measured results starting from June 1st, 2017 and up to October 1st, 2017 will be presented. During this period, the leakage test was performed where the water pressure was reduced to zero and after this the strength integrity test was performed where the water pressure was increased up to about 8 MPa. The purpose of this chapter is thereby to present the result during these two final tests that were conducted on the concrete dome before the demolition work started.

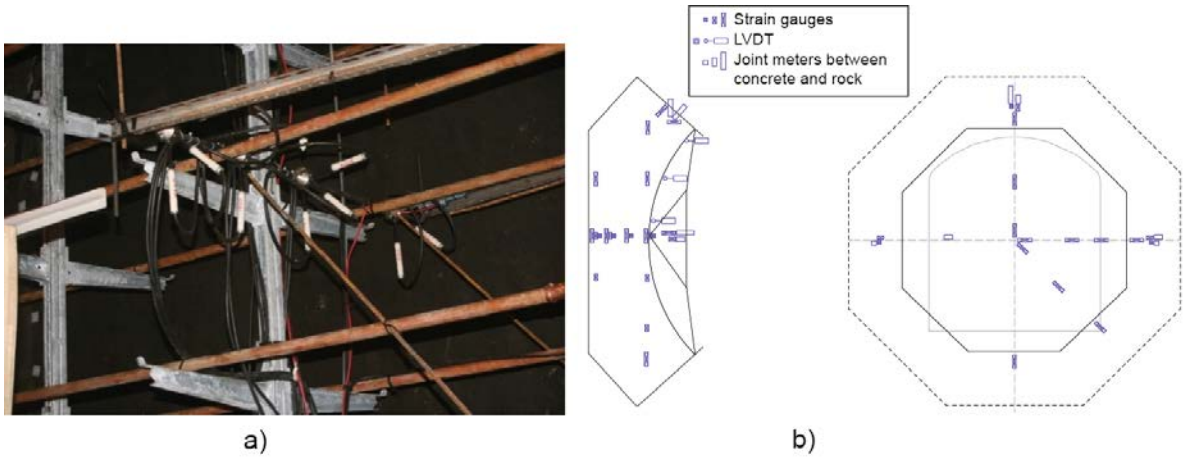

Figure 3-1. *Installed sensors, a) strain gauges in the centre, b) placement of sensors.*

3.2 Summary of conclusions from previous measurement evaluations

One of the most difficult tasks in the evaluations of the concrete dome was to determine if it had released from the rock or not during the initial cooling.

According to the simple hand calculations made in Malm (2012) and the results from the numerical FE model presented in Grahm et al. (2015), a gap of 4.8 mm would occur prior to grouting near the top if the dome released completely from the rock.

Six joint meters were installed to monitor the relative displacement between the concrete and the rock. Two in the top and two on the left- and right-hand side respectively. These sensors did not show any significant gap opening between concrete and rock. The maximum measured relative displacement was 0.1 mm according to the joint meters. The relative displacements were in general so small, and thereby corresponded most likely to elastic strains in the concrete. However, all joint meters showed a slightly larger value after grouting than before, which would indicate that at least some parts of the slot have been grouted.

Based on the difference in strain before and after the cooling in connection to the contact grouting, the extent of thermal pre-stress could be calculated. If the dome had released completely, then the full temperature variation during cooling would result in a thermal pre-stress of the dome. Therefore, the difference in strain compared to the theoretical maximum thermal pre-stress based on the temperature variation was calculated for all sensors, as seen in Figure 3-2. Almost all strain gauges showed lower pre-stress compared to the theoretical maximum where the average utilization was 53 %. Thereby, based on the calculated effect of thermal pre-stress it can be concluded that the concrete dome had partially released from the rock and it is likely that the upstream side of the slot released to a greater extent than the downstream side (i.e. where the joint meters are located).

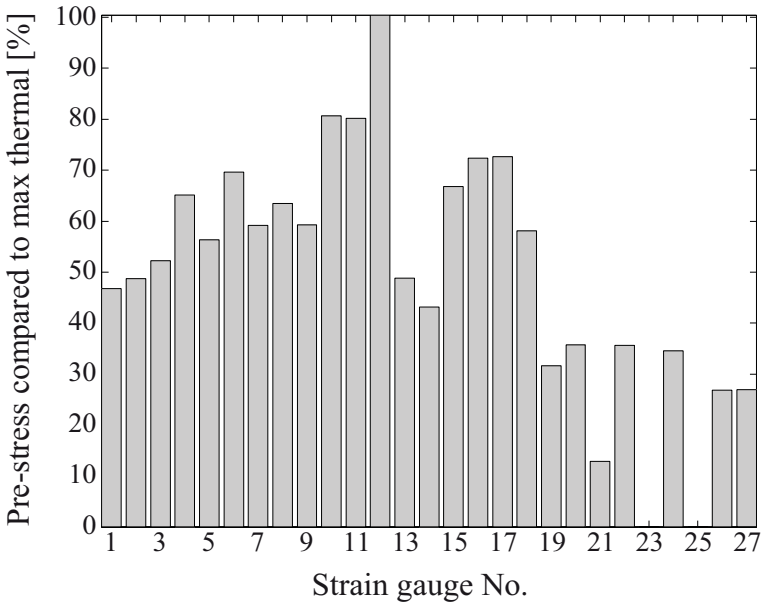

Figure 3-2. *Estimated achieved thermal pre-stress in the dome compared to maximum.*

During the increasing water pressure, up to 4 MPa hydrostatic pressure, the two joint meters in the top of the dome were significantly compressed. This occurred as an abrupt change in the measured behaviour as seen in Figure 3-3. The only possible explanation for this behaviour is that the dome released on the upstream side of the slot near the crest. Thereby, all forces on the dome were transmitted to the downstream side instead.

After the pressure of 4 MPa was reached in February 2014, it was maintained at a constant value for a bit more than 3 years, until 1st of June 2017. During this period, all sensors shows some time dependent increase in response. The reason for this increase is of course to some extent due to time dependent effects in the concrete, such as shrinkage and creep deformations of the dome. One other important factor is the swelling pressure in the bentonite clay. The saturation of the bentonite clay takes long time and as a result of the saturation, the swelling pressure of the bentonite clay occurs. According to Grahm et al. (2015) the swelling pressure in the bentonite seal closest to the concrete dome was between 0 and 0.75 MPa about one year after pressurization. Subsequent measurements have shown that the swelling pressure continued to increase and was between 0 and 1.2 MPa prior to the leakage test.

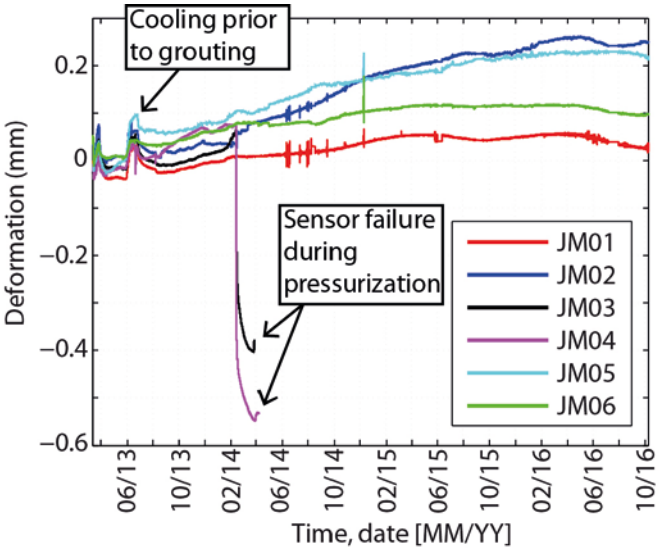

Figure 3-3. *Measured relative distance between concrete and rock.*

3.3 Results

The measured results based on the concrete dome sensors during the leakage test and the strength integrity test are presented in the following sections. The pressurization sequence is shown in Figure 3-4, below. As it can be seen in the figure, the water pressure was successively reduced to zero starting from June 1st, for the leakage test. The pressure was after this increased up to 4 MPa again after the leakage test had ended, where the target pressure of 4 MPa was reached 21st of June. After this, the pressure was maintained at this level until July 27th where the pressure was successively increased to 8 MPa, which was reached at 15th of August. After this the pressure was rapidly decreased and reached 4 MPa once again on the 18th of August.

3.3.1 Temperature

In Figure 3-5 and Figure 3-6 the measured temperature variation for all sensors in operation are shown. One additional sensor, denoted ST05T, failed recording during the strength test. The same sensors were used for both strain and temperature measurements, and thereby the placement of all temperature sensors can be seen in Figure 3-13.

During the leakage and strength test, no special activities occurred that would influence the temperature in the concrete dome. As it can be seen in the figures, all sensors show a seasonal variation where the temperature in the concrete dome varies due to the ambient temperature in the tunnel system. As seen in Figure 3-6, the temperature in the tunnel varies from between +12 °C and +16 °C where the maximum temperature occurs in August/September and the coldest temperature in February/March. The temperatures in the concrete dome shows, as expected, similar variation (but with slightly smaller amplitudes) and is also delayed about 1–2 months in time (i.e. max occurs about in October and min occurs in April).

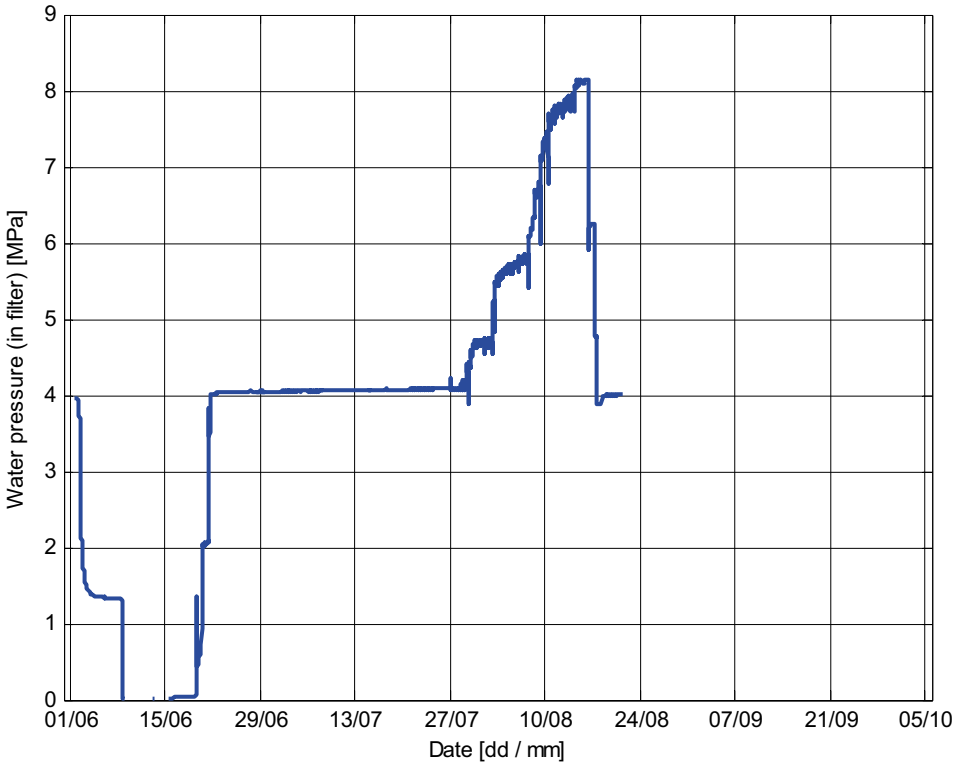

Figure 3-4. *Pressurization sequence during leakage and strength test.*

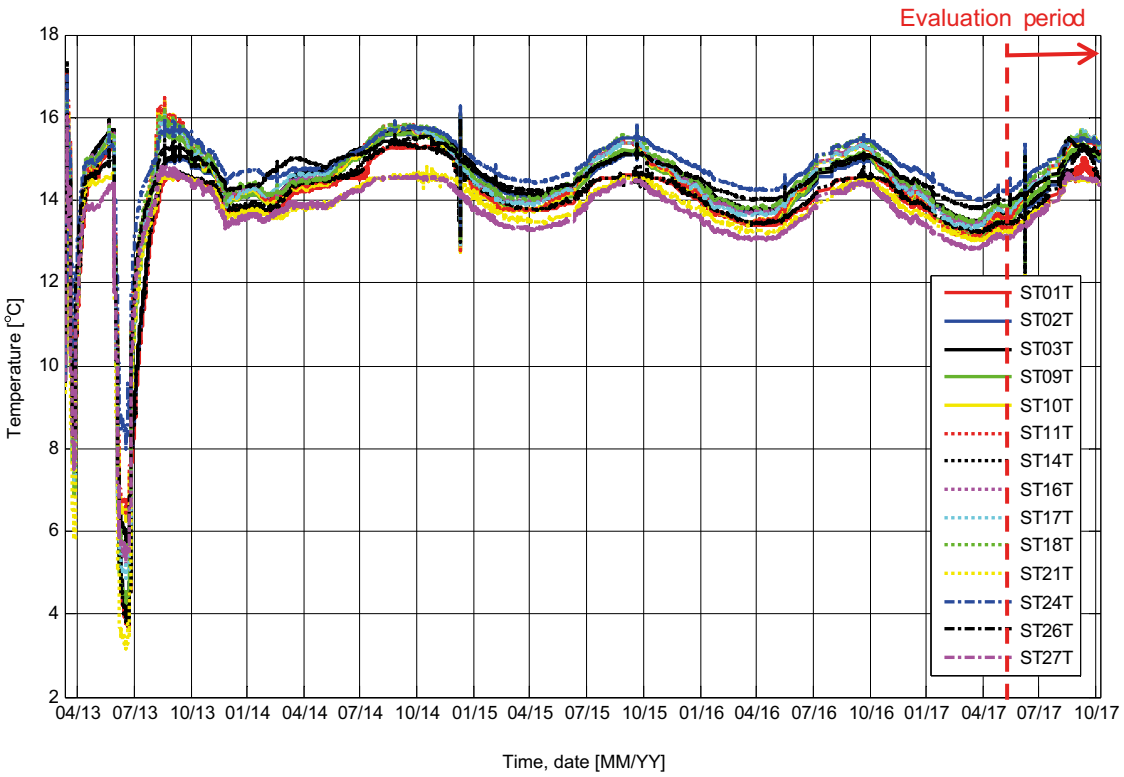

Figure 3-5. *Measured temperature variation for all temperature sensors in operation.*

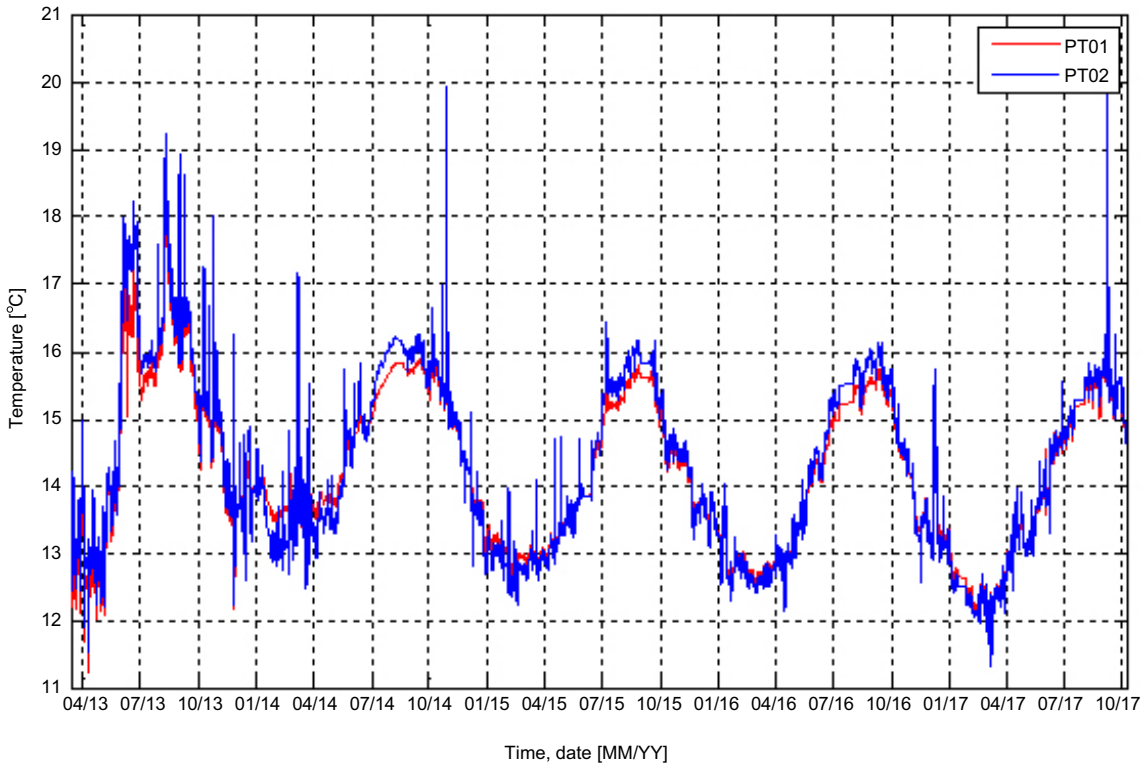

Figure 3-6. *Measured temperature variation for the two ambient air temperature sensors.*

When studying the zoomed in recordings of the temperature sensors, as seen in Figure 3-7, it can however be seen that some sensors shows some strange behaviour starting from 1st of August. It is especially sensor ST27T that gives significantly larger peak than expected and the peak also occurs earlier than expected. This sensor is placed on the right-hand side mounted near the downstream side of the slot, see Figure 3-13. In this case, the increase in temperature is about 0.5 °C higher than expected at 15th of August (i.e. the day when the pressure reached 8 MPa). This effect may occur from two reasons; leakage or confined pressure. If a leakage occurs in the interface between concrete and rock at this location, then the temperature of the flowing water would influence the temperature in the concrete. Unfortunately, the temperature of the water used for pressurization was not measured. However, it is considered unlikely that the temperature of the flowing water was higher than the tunnel temperature, and therefore this is not considered as a probable cause. Otherwise, in a confined space, when the pressure increases, the temperature can increase if the pressure increase is relatively rapid so that the temperature distribution does not have time to distribute to the whole surroundings.

3.3.2 Displacements

Only one of the original LVDT-displacement sensors, was in operation during the leakage and strength test. The other LVDT-sensors had stopped recording reliable displacements earlier, most probably due to moisture and dust that had dripped on these sensors. The displacement sensor still in operation, denoted LVDT02, was placed in near the quarter point as seen in Figure 3-8.

The measured displacement for the whole period is shown in Figure 3-9. As seen in the figure, the displacement increased about 1 mm during the initial pressurization to 4 MPa (i.e. from 2016-10-01 to 2017-05-30) and continued to increase further up to about 1.6 mm just prior to the strength test. This time dependent increase occurs mainly due to increasing swelling pressure of the bentonite seal and due to creep caused from the sustained water pressure load. In addition, it is also possible to detect small influences from the seasonal variation in temperature in the measured displacement.

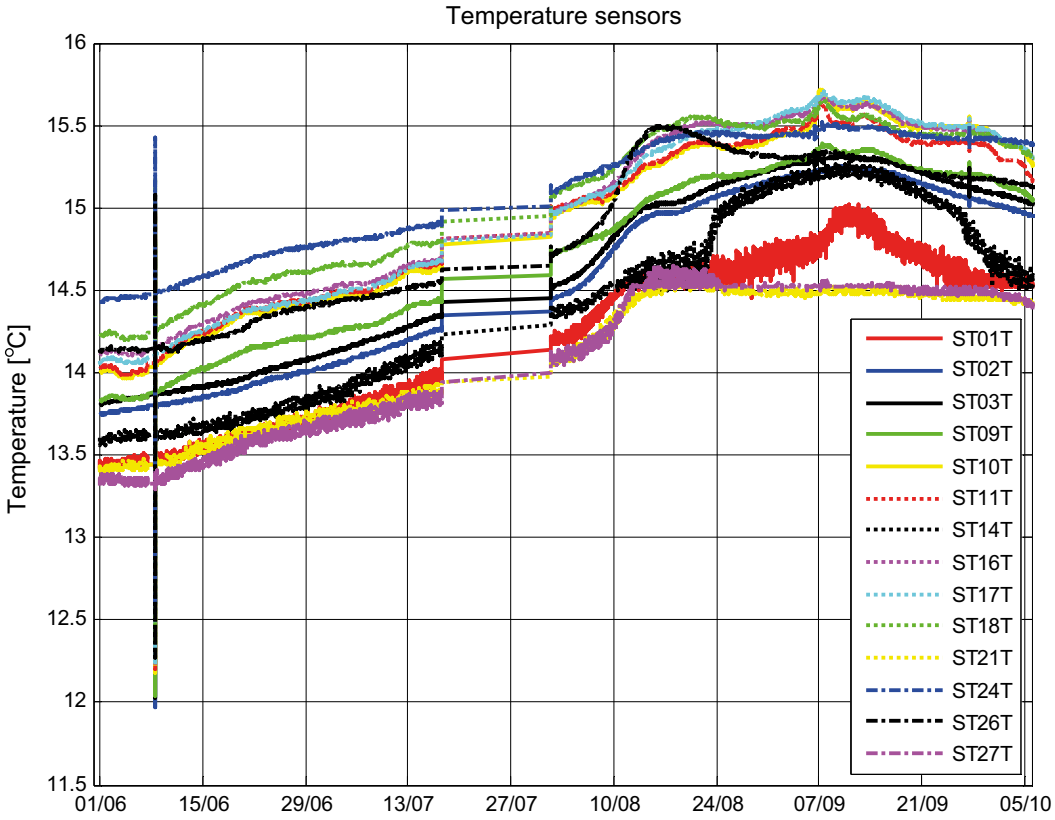

Figure 3-7. *Measured temperature variation for the two ambient air temperature sensors.*

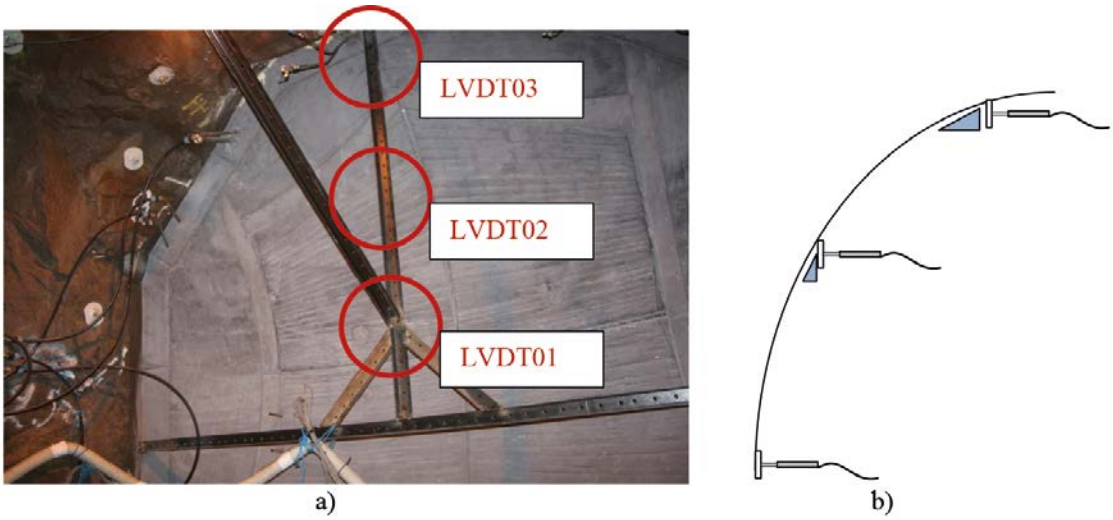

Figure 3-8. *Scaffolding used for mounting the LVDT sensors, and their approximate position.*

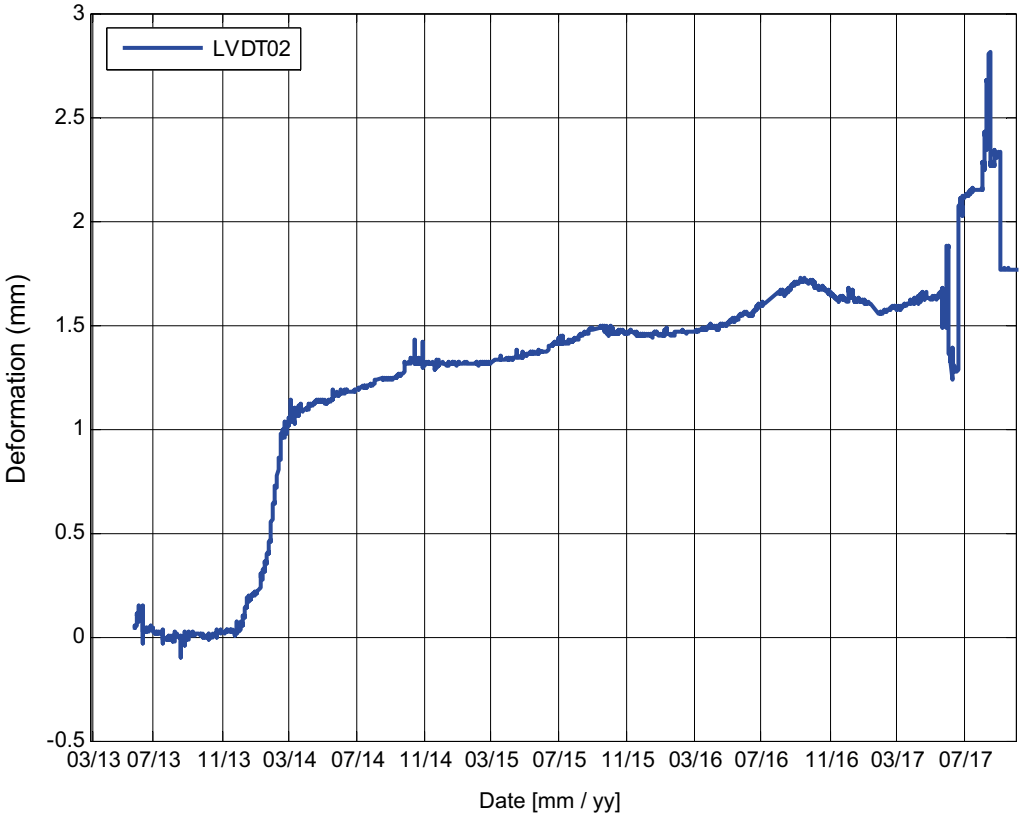

Figure 3-9. *Displacement in the downstream direction, measured with LVDT02.*

During the leakage test, the displacement decreases about 0.3 mm (to 1.3 mm), which is much less than the previous increase of about 1.0 mm during pressure increase in 2013/2014. The reason for this is to some extent due to creep where the instantaneous displacement decrease is 0.3 mm but if the leakage test would have been on-going for a longer period then the displacement would reduce further. It is however unlikely that the total deformation would be about 1.0 mm even if continued for a long time. The reason is that irreversible deformations occurs as a result of cracking and that the swelling pressure of bentonite (< 1.2 MPa) also contributed to some displacements.

During the pressure increase after the leakage test, the displacement is about 2.1 mm. It can clearly be seen that there is a difference in displacement before and after the leakage test and this is likely caused by cracking of the dome or loss of bond that occurs during the leakage test. As later shown in Section 4.2, reducing the water pressure leads to higher risk of cracking in the dome, especially in the region close to the upstream side of the slot.

During the strength test, the displacement increases almost 0.7 mm as the pressure increase from 4 MPa to 8 MPa. It can also be seen that the displacement after the strength test was higher than before the strength test, which indicates further cracking and thereby permanent deformations. Finally, the water pressure was removed completely in the beginning of September. The final permanent deformation was about 1.8 mm when the test ended.

Considering that only one LVDT sensor was in operation, additional sensors were installed prior to the leakage test. These sensors only measure the relative displacements compared to the time when these were installed, thereby the total deformation will not be possible to obtain from these. However, these sensors can be used to compare the results during the leakage test and the strength test compared to the original LVDT-sensor. The positions of the new LVDT-sensors are illustrated in Figure 3-11.

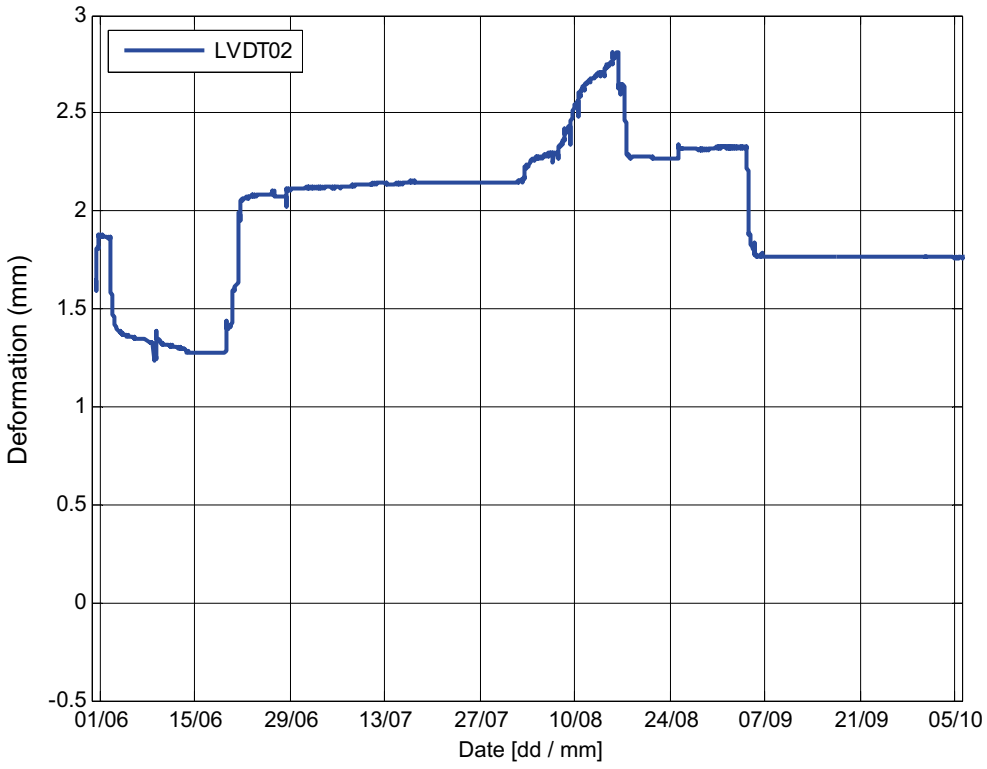

Figure 3-10. *Measurements of LVDT02, during the leakage and strength tests.*

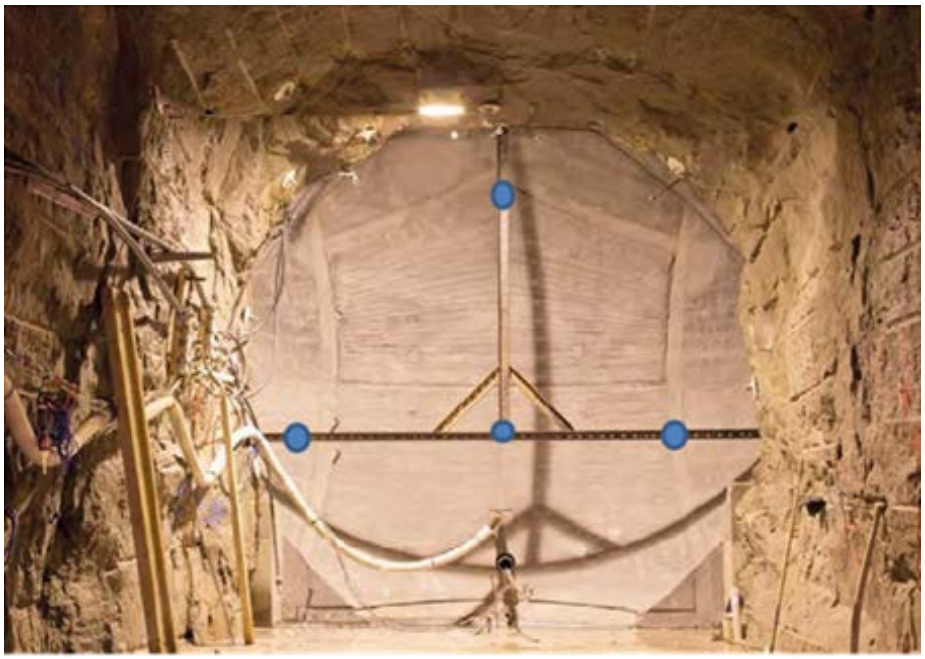

Figure 3-11. *Illustration of additional LVDT sensors installed prior to the leakage test.*

The initial displacement of all newly installed LVDT-sensors should be different since the dome has a curved deformed shape before the leakage test. Since these initial values are unknown, all newly installed sensors are adjusted with one value, 2.0 mm, in order for the results to be more comparable with the measured results from LVDT02. The results from all LVDT sensors is shown are shown in Figure 3-12. As it can be seen in the figure, the newly installed LVDT sensors gives the same behaviour as the original sensor. Based on the placement of the sensors and the expected deformed state, the displacement at the sensors called "Upper", "Left" and "Right" should all give less deformation than LVDT02 and the sensor called "Middle" should give larger displacements than LVDT02.

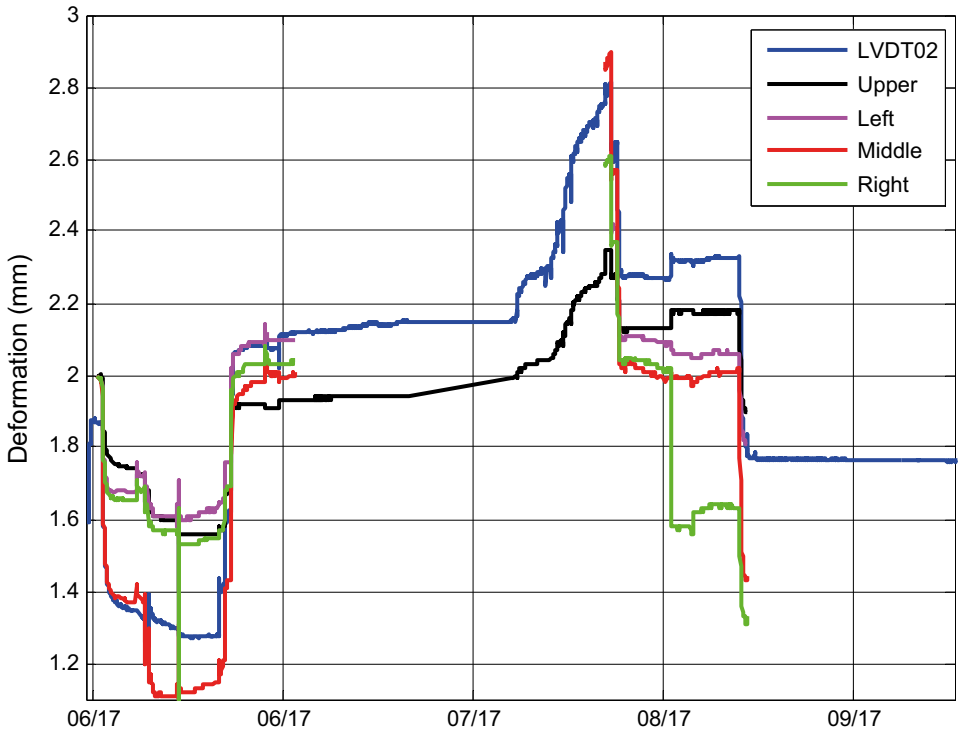

Figure 3-12. *Comparison of the original LVDT02 and the newly installed LVDT sensors.*

3.3.3 Strain gauges

The strain in the concrete was measured with 27 strain gauges, and their placement was presented in Malm (2015a) and illustrated in Figure 3-13.

During the drainage and strength test, i.e. after 2017-06-01, it can be seen that the strain varies due to the changes in the water pressure, see Figure 3-14. During the drainage test where the water pressure is decreased from 4 to 0 MPa, it can be seen resulting in an increase in strain of about 100–120 μS. This means that the compressive forces in the dome reduced. Assuming an elastic modulus of 33.9 GPa according to Vogt et al. (2009), this corresponds to a variation in stress of about 3.3 to 4.1 MPa.

After the drainage test, the pressure was increased to 4 MPa again and maintained for a short period. After this, the strength test was performed where the water pressure was increased in steps up to 8.1 MPa. During this period, the strain reduces, i.e. compressive forces increases in the concrete dome. The total variation in strain was about 100–150 μS when the water pressure was 8.1 MPa instead of 4 MPa. Assuming an elastic modulus of 33.9 GPa according to Vogt et al. (2009) this corresponds to a variation in stress of about 3.3 to 5.1 MPa.

It can also be seen that the strain level is about the same before and after the drainage test or the strength test, this indicates that the behaviour of the dome is primarily linear elastic based on the results of these local sensors.

3.3.4 Joint-meters

The relative displacement between concrete and rock was measured with six joint-meters, and their placement is presented in Malm (2015a) and illustrated in Figure 3-15.

During the drainage test and the strength test that started after 1st of June, only small variations in relative displacement can be detected for 3 of the 4 joint meters in operation. This indicates that the bond between concrete and rock is still intact in these regions. However, as mentioned earlier the joint meter denoted JM06 placed at 3 o'clock and perpendicular to the rock surface shows rapid decreasing displacement during the strength test. This behaviour is similar to what happened to the sensors JM03 and JM04 when the water pressure was initially applied. This behaviour is believed to be caused by local loss of bond on the upstream side of the slot which would cause increased compressive stresses in this region.

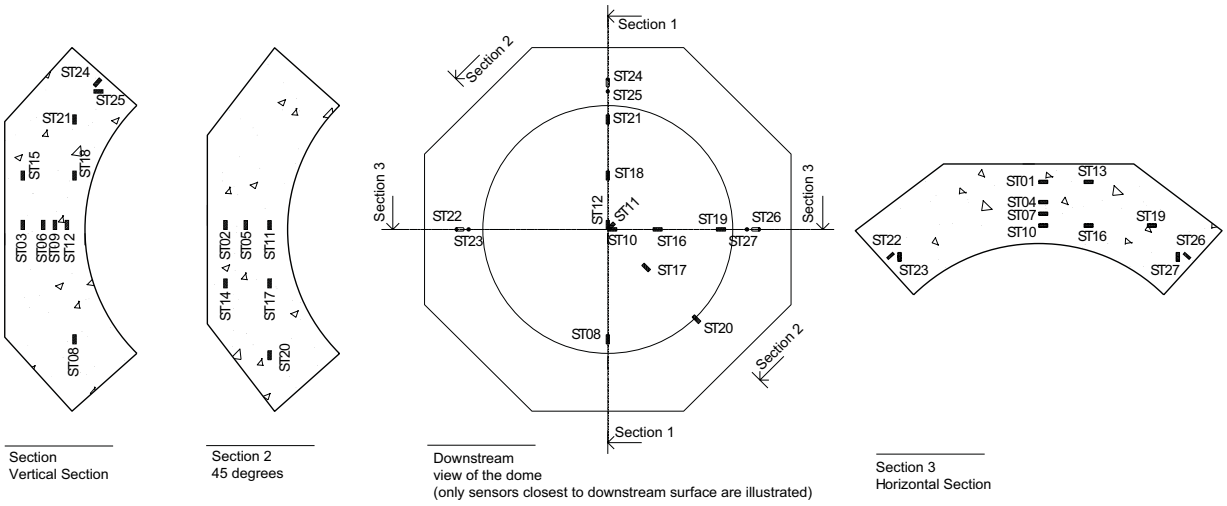

Figure 3-13. *Placement of strain gauges.*

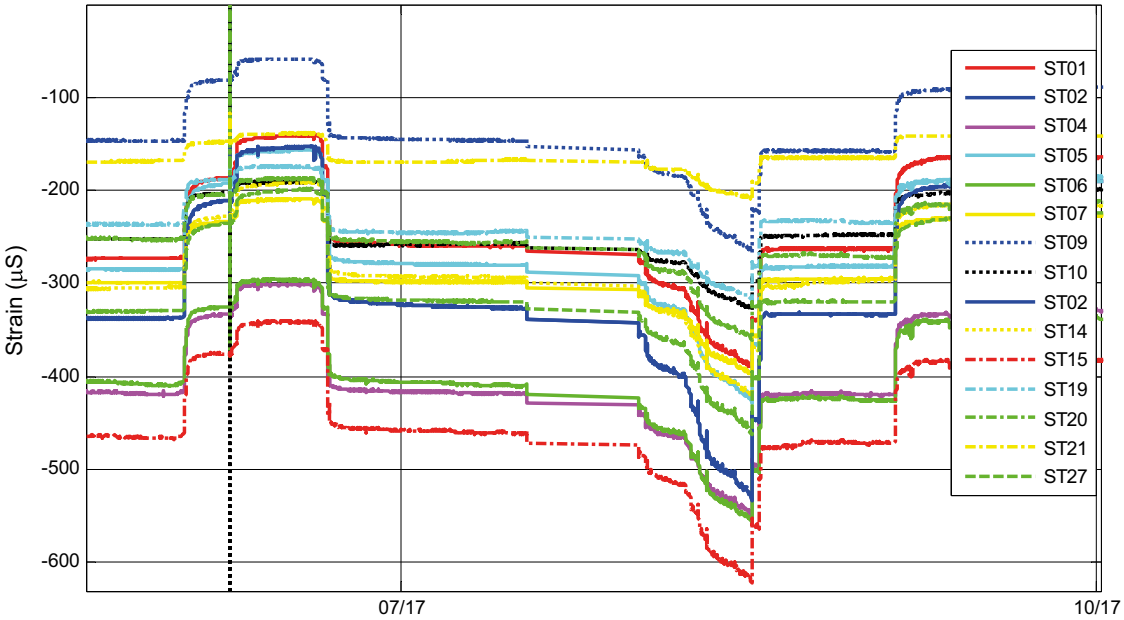

Figure 3-14. *Measured variation in strain from all strain gauges in operation, zoomed in on the period for the drainage and strength test.*

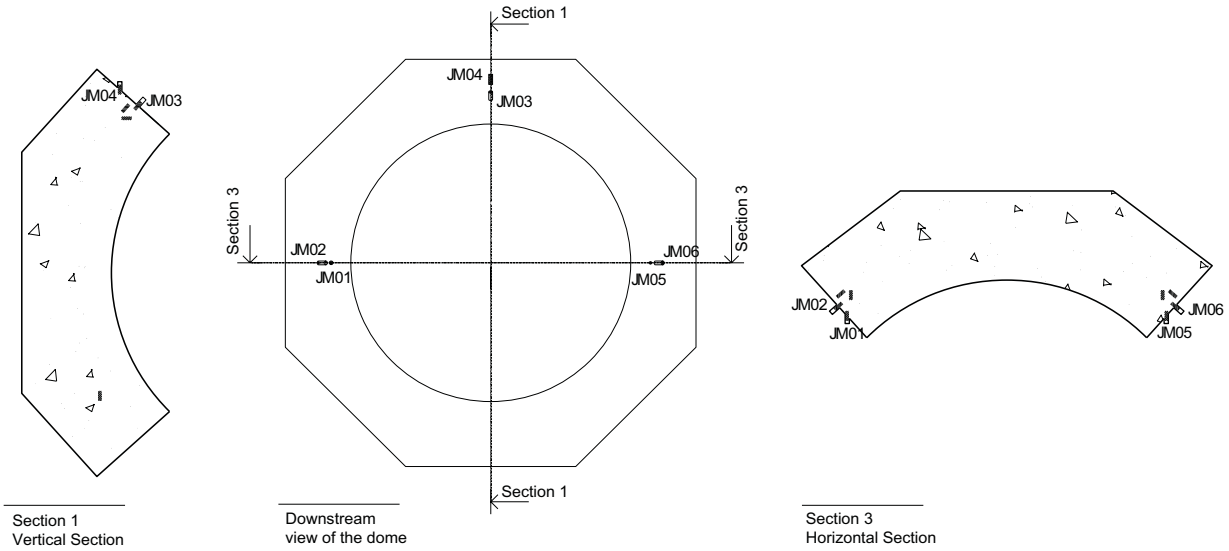

Figure 3-15. *Placement of joint-meters.*

It can be seen from the figure, that the joint-meters still in operation does not go back to zero deformation when the filter is drained, i.e. the hydrostatic pressure is removed. This shows that some permanent deformations may have occurred in the concrete dome. Of course, the swelling pressure is still active even though the water pressure is removed, but the reduction of the displacement during unloading is to small and thereby the influence from swelling pressure cannot be the main reason for these permanent deformations.

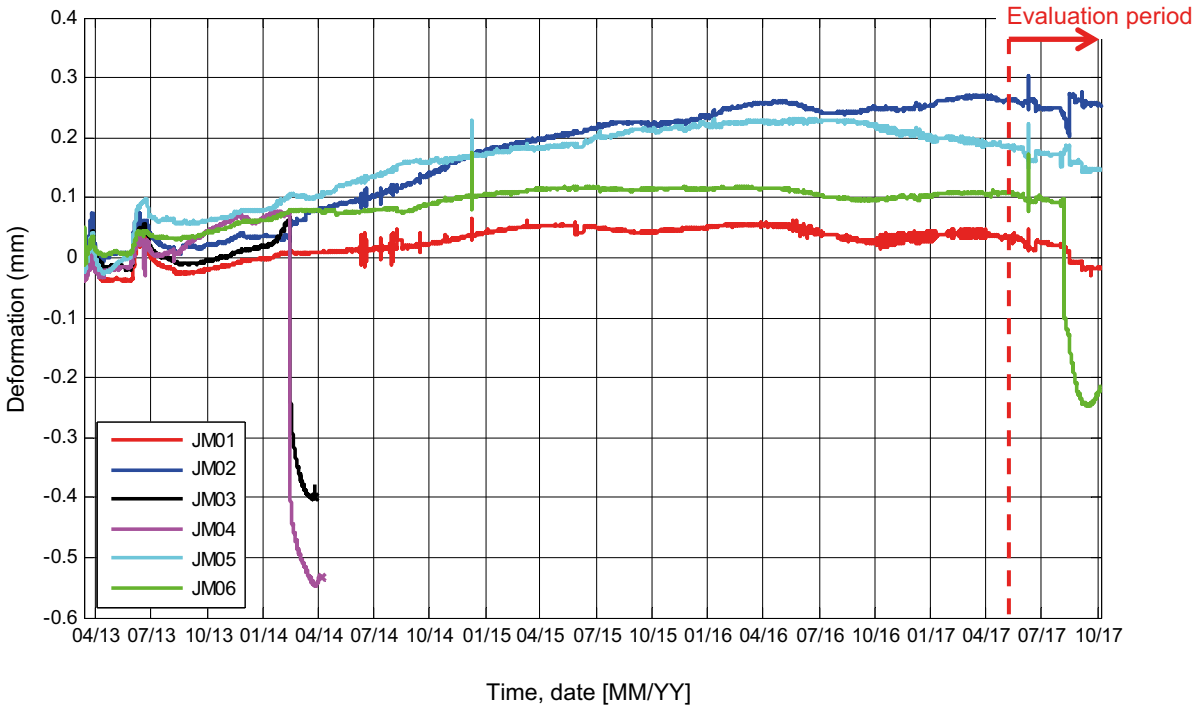

Figure 3-16. *Measured variation in relative displacement between concrete and rock from all joint-meters. (JM03 and JM04 failed during increasing water pressure in April 2014)*

3.4 Conclusions

The result shows that one additional temperature sensor failed or malfunctioned during the strength test and that one of the joint meters was compressed up to its limit.

Thereby, the following sensors could monitor the behaviour of the concrete dome during the whole test period from 2013 to 2017, as shown in Table 3-1. The sensors that stopped recording prematurely mainly failed during increasing the water pressure to 4 MPa in 2013 and it was mainly sensors close to the rock (i.e. those that were installed on reinforcement bars attached to the rock) that failed, see Malm (2015a).

Table 3-1. Sensors in operation.

Type of Sensor	Installed	In operation 2014-09-30	In operation 2015-09-30	In operation 2017-10-05
Joint meters (TML type KJA-A)	6	4	4	4
LVDT (HBM type WA)	3	1	1	1
Strain gauges (TML type KM-AT)	24	11	11	11 (10*)
Strain gauges (Geokon 4200)	4	4	4	4
Temperature sensors (PT 100)	2	2	2	2

* it is only the signal from the thermocouple that failed, the strain was still recorded by this sensor.

In Figure 3-17, the failed strain gauges are illustrated with red colour. The strain gauges still in operation are illustrated with black colour (TML sensors) or blue colour (Geokon sensors). By comparing the number of failed sensors, it can be seen that primarily the TML strain gauges has failed. One should however remember that these were placed in more critical section compared to the Geokon sensors, i.e. close to the upstream surface and near the slot in the top of the dome. In general, it is therefore not possible to say that one sensor was more robust than another. However, some of the Geokon sensors were placed relatively close to the TML sensors that failed, which indicate that these may be more robust for this application.

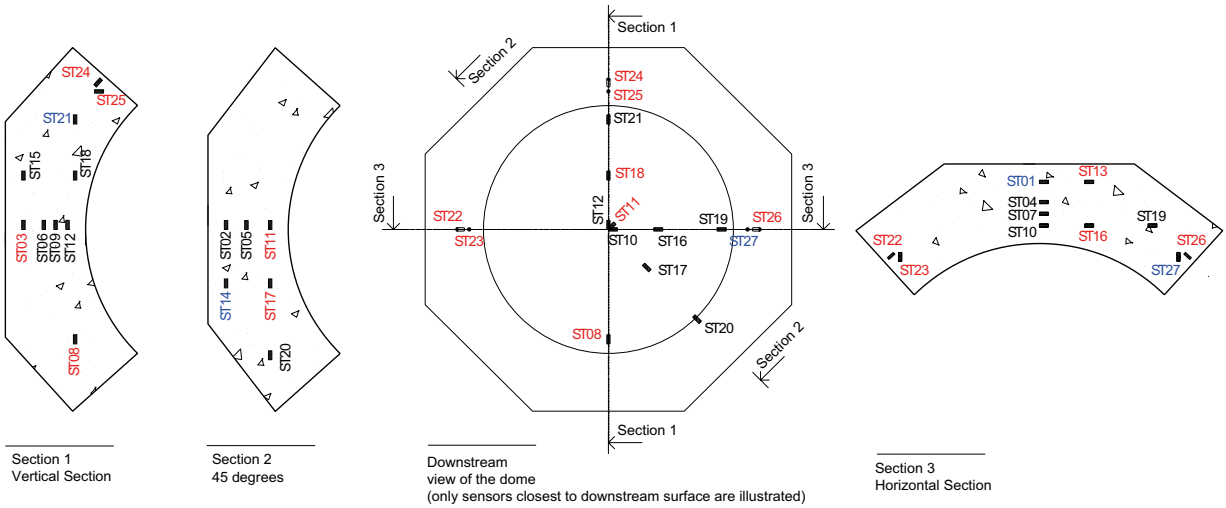

Figure 3-17. *Sketch of placement of strain gauges. Strain gauges with black colour are TML sensors still in operation, blue colour represent Geokon sensors in operation and sensors with red colour represent TML sensors that malfunctioned/failed.*

The results show that most sensors have worked as intended for a long period of 4.5 years embedded in the concrete dome. The sensors made it possible to monitor the behaviour of the dome from casting and during the increasing water pressure up to 4 MPa which was kept constant for a long period and finally during the drainage and strength test. When the dismantling of the dome initiated, all sensors cables were cut and thereby not monitoring anymore.

Based on the results from the leakage and strength test, it could be seen that the sensors that measure the global behaviour, i.e. LVDT-sensors show differences before and after leakage or strength tests which indicates cracking in the dome. The sensors that measure the local behaviour varies to some extent depending if these show these differences before and after a variation in pressure. The reason is of course if these sensors are mounted close to the area of cracking or where the loss of bond occurred. The strength test of the full-scale test was successful in proving that the dome concrete dome can withstand its theoretical design loads.

4 FE-Simulations

As a part of the pressurization test, finite element simulations (FE-simulations) were performed and analyzed. The results from the FE-simulations were also compared with the measurements from the full-scale test. The FE-simulations were based on the models and techniques developed in Grahm et al. (2015).

Previous models were used for modeling but the analysis time was extended to include the entire life time of the plug, including the pressurization test. Therefore, the design premises and conditions used in the previous models still apply. They will be summarized in the next section. The applied pressure is based on measurements from pressure sensors installed in the filter of the plug.

4.1 FE-model

4.1.1 Model

The models used in this project are identical to the models used in Grahm et al. (2015), see Figure 4-1. A summary of the model will be presented in this report.

The calculations are performed in two stages. The first stage is a transient thermal analysis to determine the temperature distribution in the structure. The temperature distribution is dependent on ambient temperature, heat production during the hydration of the concrete and the cooling sequence. The second stage is a mechanical analysis to calculate the stresses, strains and deformations in the concrete dome due to temperature, time dependent variables (creep, shrinkage and strength development) and structural loads, such as hydrostatic pressure and dead weight.

The mechanical simulations were also divided into steps to simulate different sequences of the construction and loading.

The three-dimensional model represents half the concrete dome with a symmetry plane along the center of the model, as seen in Figure 4-1. The model includes:

- The surrounding rock.
- Concrete dome (unreinforced).
- Cooling pipes (only in the thermal model).
- Embedded strain gauges (only in the mechanical model).

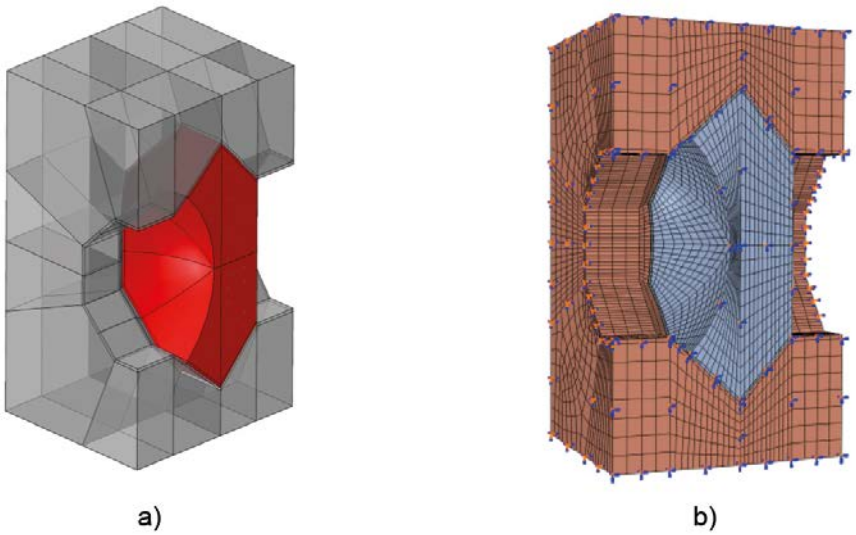

Figure 4-1. *Illustration of the FE-model used in previous analyses (Grahm et al.2015).*

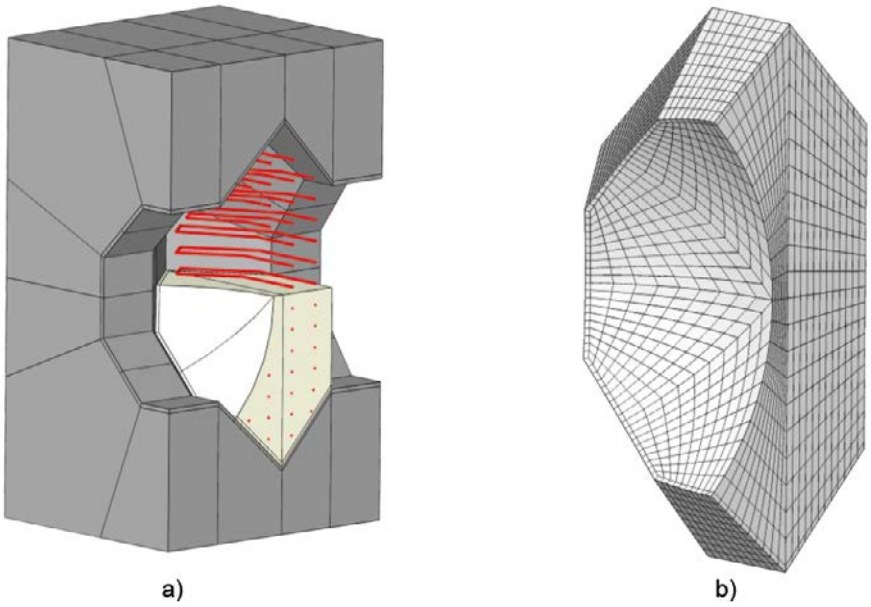

Figure 4-2. *a) Geometry, including cooling pipes and b) Mesh (Grahm et al. 2015).*

In Figure 4-1, the geometry of the concrete dome with the embedded cooling pipes and the FE-mesh is depicted. The element types are presented in Table 4-1.

Table 4-1. Summary of the mesh in the thermal and mechanical model

	Thermal model		Mechanical model	
	Element ID	Number of elements	Element ID	Number of elements
Rock	DC3D8	18944	C3D8/C3D20	17228/1716
Concrete	DC3D8	10076	C3D8/C3D20	8360/1716
Cooling pipes	DC1D2	710	-	-

4.1.2 Material properties

The material properties are identical to those used in Grahm et al. (2015) and are summarized in Table 4-2 and Figure 4-3. The behavior of the concrete is based on the findings from Vogt et al. (2009).

Table 4-2. Material properties used in the thermal analysis.

	Density [kg/m^3]	Conductivity [W/(mK)]	Heat capacity [J/(kgK)]
Concrete/SKB R-09-07/	2336	2.1	1000
Rock	2600	3.7	900
Cooling pipes	7800	45	384

4.1.3 Loads and boundary conditions

The simulation is performed for the entire time span of the full-scale test, from casting in 2013 to the pressure test and subsequent end of the test in 2017.

Initially, a thermal analysis was performed where the temperature distribution is simulated from grouting to the pressurization up to 4 MPa. The temperature is assumed to be constant thereafter. The thermal analysis is based on the heat production from the hydration of the concrete and thermal boundary conditions defined for the cooling system and the ambient temperature in the tunnel system.

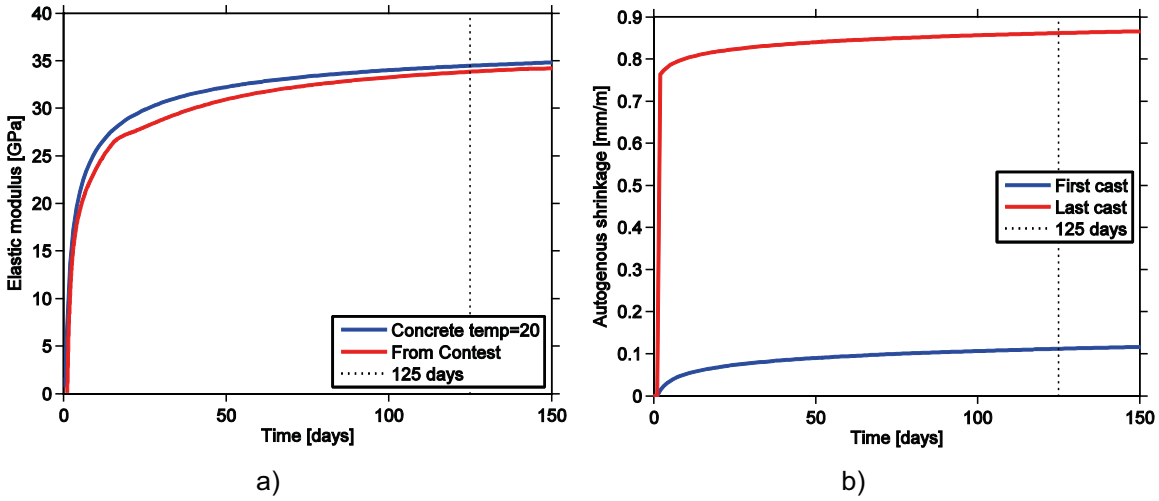

Figure 4-3. *Time dependent material properties, a) Young's modulus b) autogenous shrinkage (Grahm et al. 2015).*

The calculated temperature distribution is used as input in the mechanical analysis where the temperature difference causes volumetric changes. The mechanical analyses also include the weight of the concrete and the applied water pressure. The water pressure is assumed to be fully developed at the vertical upstream face and at the upstream face of the abutment. At the downstream face of the abutment, the water pressure is assumed to be decreasing linearly from full water pressure to atmosphere pressure according to Figure 4-4.

4.1.4 Contact grouting

The model is based on linear elastic properties. Which means that the process when the dome loses contact with the rock cannot be simulated. Because of this, three different models have been used.

- No adhesion between the rock and the concrete dome before the contact grouting, which means that the dome can expand freely during the autogenous shrinkage.
- Full adhesion between the rock and concrete initially.
- The adhesion is broken (only the upstream face of the abutment) during the cooling before the contact grouting.
- The adhesion is broken (only the upstream face of the abutment) just before the water pressure is applied.

The contact grouting is simulated by the introduction of new elements, which connects the dome and the rock. This is described in further detain in Grahm et al. (2015).

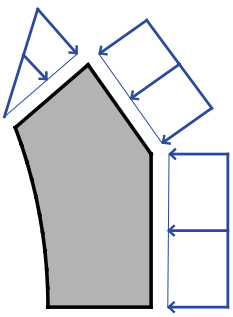

Figure 4-4. *A schematic illustration of the water pressure on the concrete dome (Grahm et al. 2015).*

4.1.5 Sequences of the analyses

The first part of the simulations, the construction process and loading, are performed with the same sequences as Grahm et al. (2015). After the initial loading, an additional three years of constant pressure of 4 MPa is added, to study the steady state. These analyses did not include the swelling pressure of the bentonite. The constant pressure is followed by the load cycle used to perform the gas leakage and strength tests. A curve fit of the loading sequence used in the pressure test is depicted in Figure 4-5.

The loading sequence had two stages. The drainage was first opened to reduce the pressure to zero to perform the gas leakage test. A pressure of 4 MPa was thereafter restored and subsequently increased to 8.1 MPa. The goal was to achieve 9 MPa in total pressure, i.e. water pressure and swelling pressure from the bentonite. During pressurization to this high pressure, excessive leakage occurred in the rock fractures discussed in Grahm et al. (2015). However, considering that this was a strength test, the leakage was not a concern. Before the test was ended, the pressure was returned to 4 MPa. The curve used for the pressure in the simulations (Figure 4-5) was based on measurements from the filter of the plug.

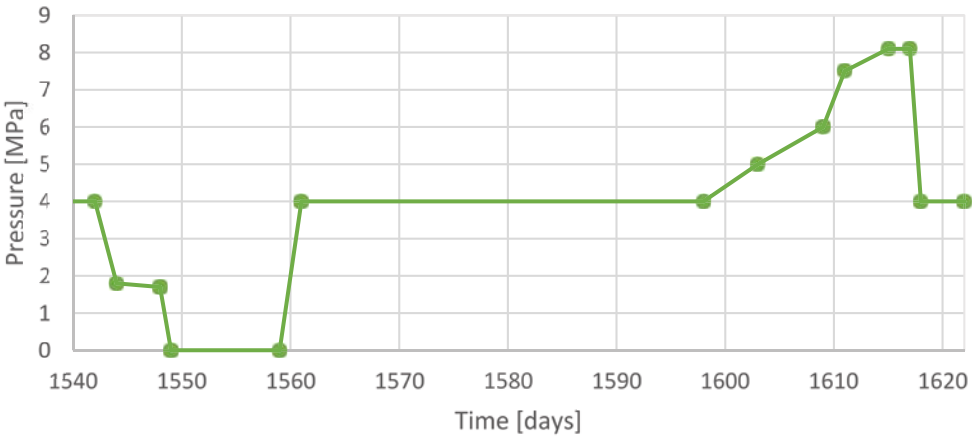

Figure 4-5. *The pressure sequence used in the simulations during the pressure test.*

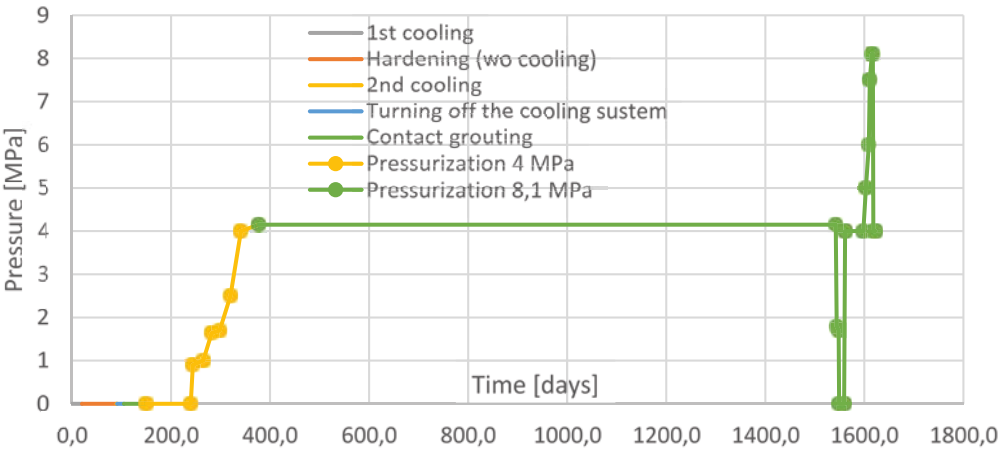

Figure 4-6. *The entire pressure sequence used in the simulations.*

4.2 Simulation results

From casting until pressurization of 4 MPa, identical models were used as in Grahm et al. (2015). These results are already public and will not be presented in this report. In all subsequent figures depicting the stress distribution, tension will be illustrated with red and compression with blue color.

Previous simulation presented the stress distribution before the water pressure was added. These analyses showed that large tensions would arise if the bond was not released before contact grouting. In Figure 4-7 case b and c, the red color illustrates tension which exceeds 20 MPa. 20 MPa is significantly higher than the tensile strength of the concrete. In these two cases, almost the entire concrete dome is exposed to high tensile stresses.

When the water pressure is increased to 4 MPa, the tensile stresses decrease in all models. The decrease is due to the dome shape, which transfers the applied pressure trough compression. The model without bond is only exposed to compressive stresses at 4 MPa hydrostatic load.

During the gas leakage test, the drainage was opened and the pressure was reduced to zero. In the model without bond, the concrete dome was still only exposed to compressive stresses. In the models assuming full initial bond, areas with high tensile stresses occurred. The tensile stresses indicate a risk for cracking or lost bond between the rock and concrete at the downstream face of the abutment.

The measurements of the concrete dome indicate that it has partial bond to the rock, which would represent a combination of the two cases. According to Grahm et al. (2015), the best conformity between the measurements from strain gauges, joint meters and simulations was achieved in the case where the bond is released prior to the application of water pressure (case c in the presented figures). This means that there could be a risk for cracking or a loss of bond between the rock and concrete, which could affect the structure during the subsequent increase of pressure. However, no cracking was identified in this region in the full-scale test, neither via visual inspection, core-drilling or NDT. This indicates partial bonding between the rock and concrete and that the shrinkage in the full-scale test was lower than the assumed value in the simulations.

During the second part of the load cycle, where the pressure was raised, the compressive stresses in the structure increased. The increased compression reduces the risk for cracking. A peak hydrostatic pressure of 8.1 MPa was achieved. This is not enough to cause cracking in the model without bond. In the models with initial bond, however, large tensile stresses occurred at the downstream face of the dome.

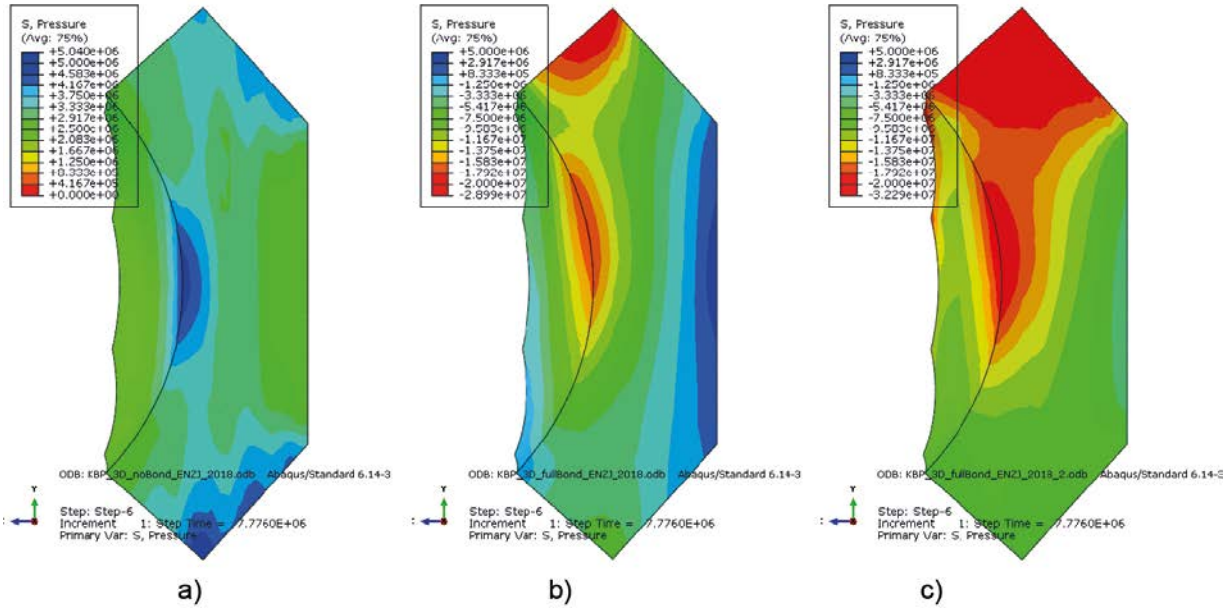

Figure 4-7. *Stress distribution subsequent to contact grouting but prior to the application of water pressure a) no bond before contact grouting, b) initial full bond with release during cooling before contact grouting, c) initial full bond with release when the water pressure is applied.*

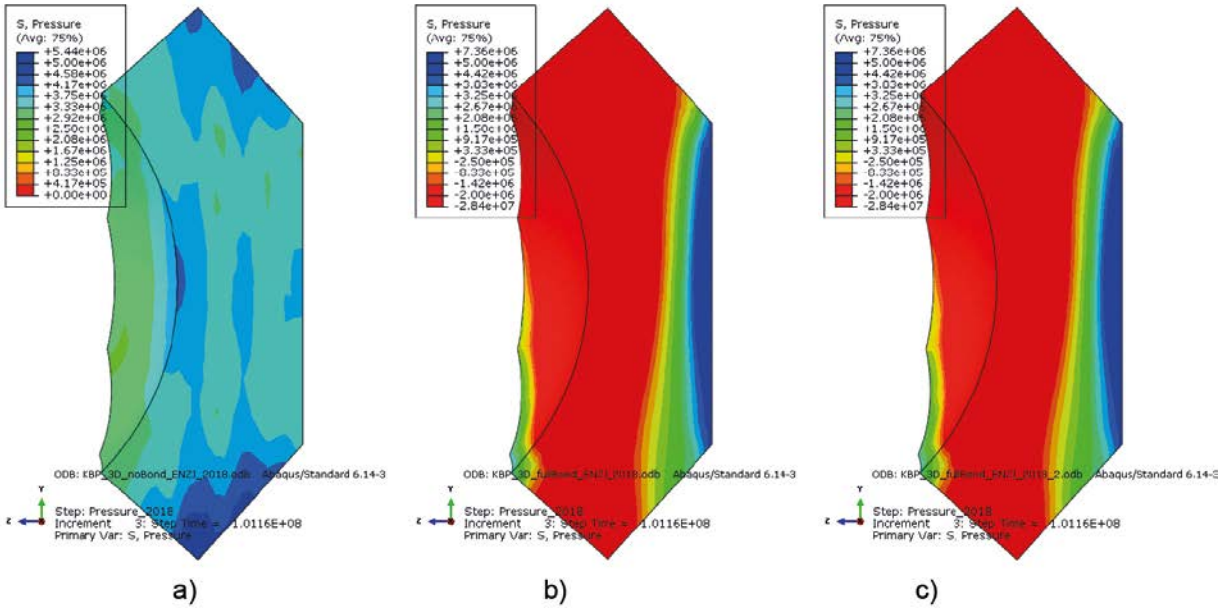

Figure 4-8. *Stress distribution during drainage, before gas leakage test, a) no bond before contact grouting, b) initial full bond with release during the cooling before contact grouting, c) initial full bond with release when the water pressure is applied.*

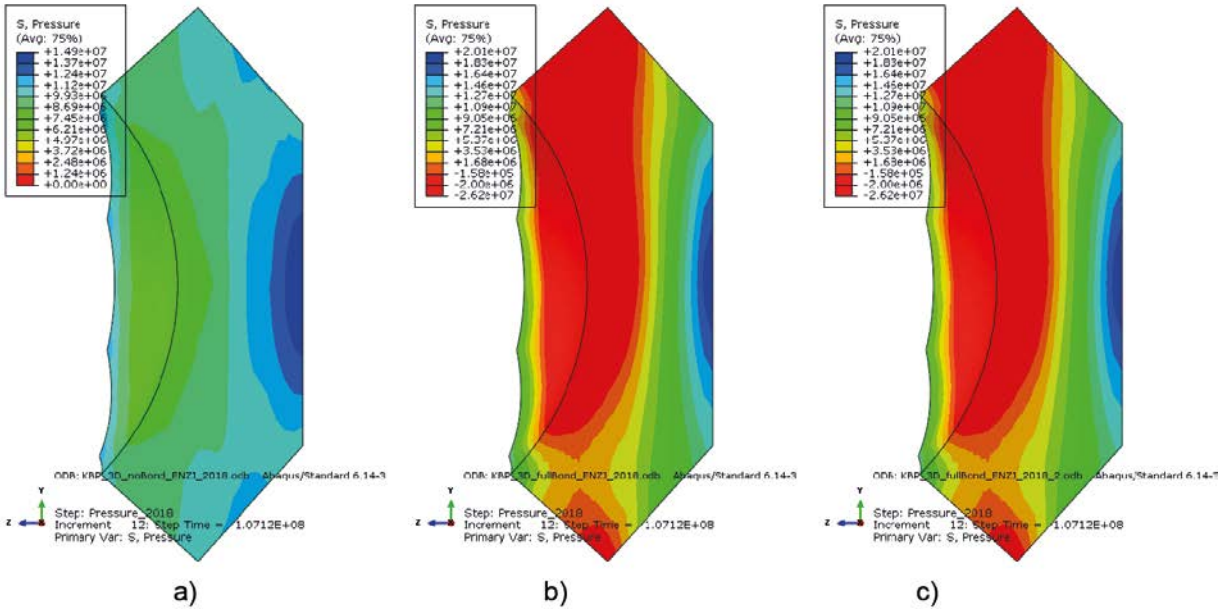

Figure 4-9. *Stress distribution at a hydrostatic pressure of 8.1 MPa, a) no bond before contact grouting, b) initial full bond with release during cooling before contact grouting, c) initial full bond with release when the water pressure is applied.*

There is also a risk for a crack parallel with the downstream face of the abutment in the upper part of the concrete dome, which is illustrated as crack B in Figure 4-10. According to prior simulations, this is the crack which potentially can lead to failure, although considerably higher pressures are required in the backfill (> 20 MPa).

Note that the time when the bond is lost does not influence the results at the later stages of the analyses for the model with initial bond. This is due to the linear elastic material properties, which are not history-dependent.

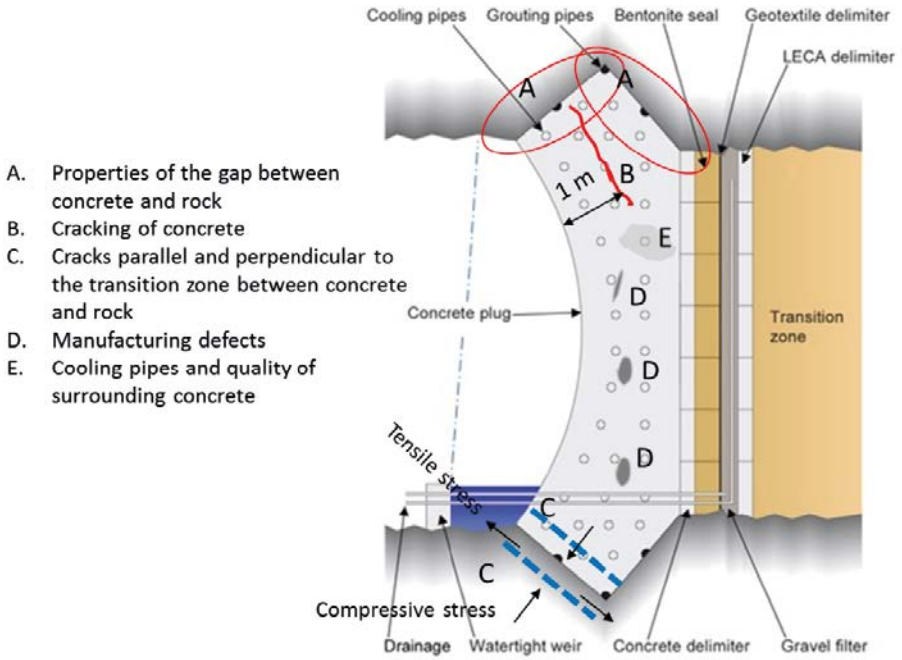

Figure 4-10. *Illustration of potential defects, which could be present or appear in the concrete dome.*

4.3 Comparison to measurements

From the FE-simulations, results have been extracted from the same positions as the various instruments. Previous comparisons have been made between simulations and measurements in e.g. Grahm et al. (2015) and Kristiansson (2014). This report focuses on the period of the gas leakage test and the strength test and will therefore present results from 1 June 2017 to the end of the test. Temperature changes have not been included in the FE-simulations and will not be presented. Comparisons are presented for the strain gauges and the LVDT-meters.

The FE-simulation performed without bond between the rock and concrete before the contact grouting is denoted as noBond. The model with initial full bond that releases during cooling before contact grouting will be denoted fullBond. The model with initial full bond that releases when the water pressure is applied will be denoted fullBond2. Note that the two models with initial full bond will have very similar behaviors after the construction stage and their respective curves will often be on top of each other in the figures presented.

4.3.1 Strain

Initially, 27 strain gauges were installed in the concrete dome. At the time of the tests, 9 strain gauges were still functioning correctly. While comparing measurements and simulations, finding a common zero is difficult. To be able to study the structural behavior better, the simulated strains were therefore normalized to the measurements a couple of days before the test was performed.

The placement of the strain gauges was covered in Section 3.3.3. Only the results of the comparison will be presented here. Comparisons with Strain gauge ST12 and ST21 presented in Figure 4-11 and Figure 4-12 respectively. ST12 is placed in the center of the concrete dome and ST21 is placed closer towards the edge. At the center of the concrete dome, the measurements correlates better with the full bond-simulations during the leakage test. However, the correlation is better with the no bond-simulation during the strength test. This could indicate that cracking has occurred. Toward the edge of the concrete dome, the measurements correlates better with the no bond-simulations for both the leakage and strength tests. Comparisons with the rest of the strain gauges in operation is found in Appendix B.

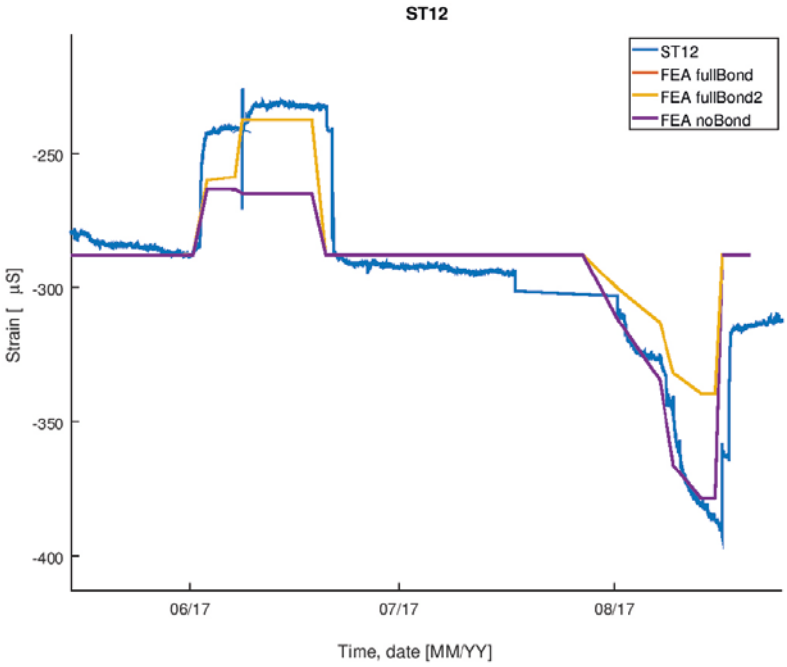

Figure 4-11. *Strain gauge ST12 compared with FE-simulations.*

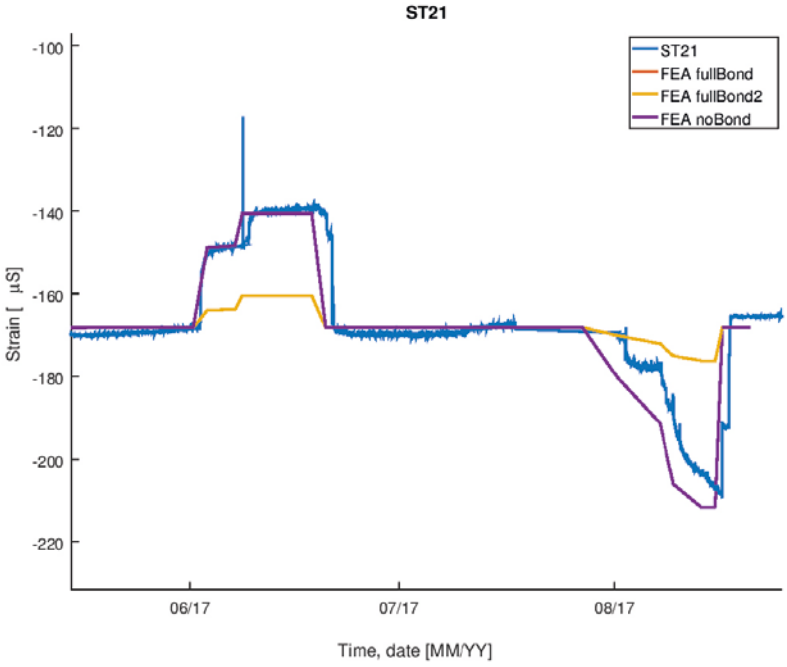

Figure 4-12. *Strain gauge ST12 compared with FE-simulations.*

4.3.2 LVDT

Only one of the original LVDT-sensors was functioning correctly through the entire test time. Four new LVDT-meters was therefore installed for the leakage and strength tests, see Section 3.3.2. However, there was issues with the new meters as well and only one gave recordings through both leakage and strength test. The FE-simulations were normalized to the LVDT-sensors to be able to compare the structural response of the leakage and strength tests better.

A comparison between the simulations and the old LVDT-meter denoted LVDT002 is presented in Figure 4-13 and a comparison with the new LVDT-meter denoted LVDT-Upper is Presented in Figure 4-14. The measurements correlates better with the FE-simulations with initial bond between the rock and concrete. The LVDT-sensors shows increased displacements after the leakage and strength tests, which indicates cracking. The FE-simulations were performed with a linear elastic material model and therefore cannot capture this behavior. Comparisons with the remaining LVDT-sensors in operation can be found in Appendix B.

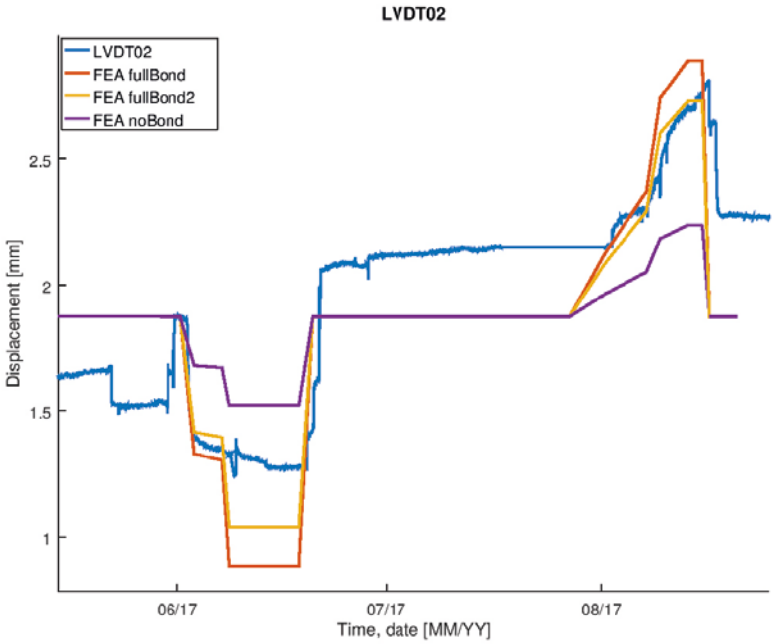

Figure 4-13. *LVTD002 compared with FE-simulations.*

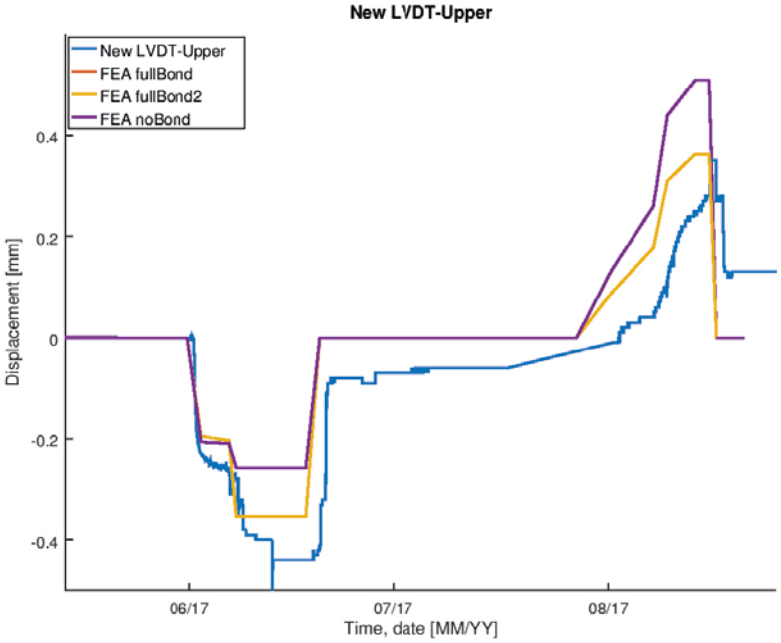

Figure 4-14. *LVDT-Upper compared with FE-simulations.*

4.4 Conclusions

In general, the structural behavior of the FE-model coresponds well with the measurements. However, the swelling pressure of the bentonite and creep in the concrete was included. This was particularly evedent during the comparison with the LVDT-sensors. By including creep and the swelling pressure, the correlation might be improved. A material model that includes the cracking of the concrete, rather than a linear elastic model could possibly improve the model as well.

5 Summary

In this report, the results from measurements and simulations of the concrete dome during leakage and strength tests are presented. This includes, non-destructive testing (NDT) before the leakage test in order to evaluate NDT measurement techniques and to assess potential defects in the dome. In addition, measurements and simulations are presented for the response of the concrete dome during both leakage and strength test.

The NDT tests showed that it will be difficult to find smaller defects inside the concrete dome. The reason for the difficulties are of course the large thickness of the dome but also its shape on the down-stream side and smaller irregularities in the surface from the formwork. Overall, the NDT testing based on the ultrasonic tomography (MIRA) and the ground penetrating radar (GPR) showed most potential and these could be used to obtain results for the whole thickness of the dome. No defects in the dome were observed with these methods.

During the dismantling work of the dome, a larger void was found in the top of the dome. This void was caused by casting had not been able to completely fill the form. This defect was not seen by the NDT tests, but on the other hand was not looked for due to budget restraints. It is not certain that this defect would be possible to detect due to the difficulty to access this area with radar or ultrasound waves.

The measurements show that the concrete dome could withstand the design loads during the strength test without being subjected to significant cracking. The risk of cracking was actually higher in the leakage test since removal of the hydrostatic pressure results in high tensile stresses in the dome. Based on the measurements, it can be seen that the global behaviour shows that the displacements do not go back to zero value when the water pressure. Some influence from the remaining swelling pressure is expected but the permanent deformations are too large to be caused by the swelling pressure alone. The measurements thereby show that there has been some loss of bond, most likely in the upstream part of the slot, at least partially over this surface. Based on the strain gauges, that measure the local behaviour at individual points in the dome does not show this effect with permanent deformations which indicate that the areas where these are located primarily still are connected to the rock.

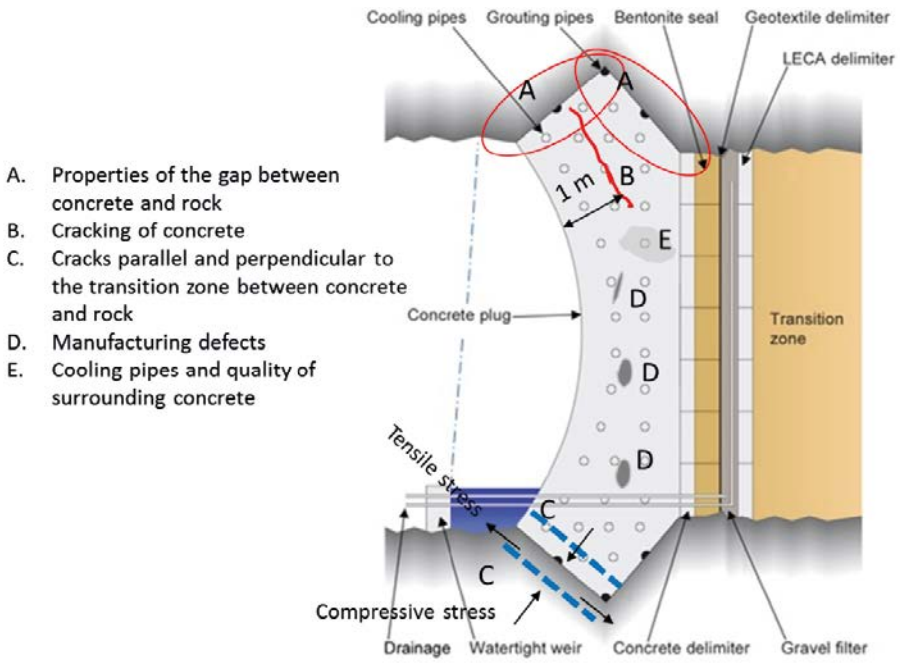

Figure 5-1. *Illustration of the plug and potential defects in the dome.*

The numerical model shows good agreement with the experimental results. The numerical model provides additional information and thereby leads to better understanding of what is happening in the concrete dome during the leakage and strength test. One downside with the numerical model is however that it is not capable to simulate loss of bond during the test. Instead, three different models were used based on different assumptions on the interaction between concrete and rock. When comparing the result from the numerical models with the measured curves, it can be seen that likely additional cracking and loss of bond on the upstream side of the slot occurred during the leakage test but also to some extent in the strength test.

Overall, the full-scale test of the plug has proven to be successful where the concrete dome has been able to withstand the loads, and despite the fact that it did not completely release during the initial cooling still was sufficiently leak tight to allow for the bentonite seal to saturate. It is important to remember that the dome could do this even though the casting could not be made all the way to the top of the dome, thereby leaving a void in the top. This shows that the current design of the concrete dome is robust and that it, despite these defects, still is able to fulfil its purpose.

References

SKB's (Svensk Kärnbränslehantering AB) publications can be found at www.skb.com/publications. SKBdoc documents will be submitted upon request to document@skb.se.

Germann Instruments, 2018. MIRA. Available at: http://germann.org/products-by-application/flaw-detection/mira

Grahm P, Malm R, Eriksson D, 2015. System design and full-scale testing of the Dome Plug for KBS-3V deposition tunnels. Main report. SKB TR-14-23, Svensk Kärnbränslehantering AB.

Kristensen A L, 2018. Revised replacement report – Examination of vault plug. Report 117-30437, Force Technology. SKBdoc 1618653 ver 1.0, Svensk Kärnbränslehantering AB.

Kristiansson A, 2014. Evaluation of a concrete plug – From the Dome Plug Experiment DOMPLU at Äspö HRL. KTH Betongbyggnad.

Malm R, 2012. Low-pH concrete plug for sealing the KBS-3V deposition tunnels. SKB R-11-04, Svensk Kärnbränslehantering AB.

Malm R, 2015a. Instrumentation of the concrete dome plug DomePlu. TRITA-BKN, Report 147, KTH Royal Institute of Technology.

Malm R, 2015b. Evaluation of the concrete dome plug DomePlu – follow-up 2015. TRITA-BKN, Report 156, KTH Royal Institute of Technology.

Malm R, 2016. Evaluation of the concrete dome plug DomePlu – follow-up 2016. TRITA-BKN, Report 161, KTH Royal Institute of Technology.

Malm R, 2017. Evaluation of the concrete dome plug DomePlu – follow-up 2017. TRITA-BKN, Report 167, KTH Royal Institute of Technology.

Sansalone M J, Streett W B, 1998. Impact-Echo: the book. Available at: http://www.ndt.net/article/0298/streett/streett.htm#7

Vogt C, Lagerblad B, Wallin K, Baldy F, Jonasson J-E, 2009. Low pH self compacting concrete for deposition tunnel plugs. SKB R-09-07, Svensk Kärnbränslehantering AB.

Appendix A

Measured curves

A1 Temperature

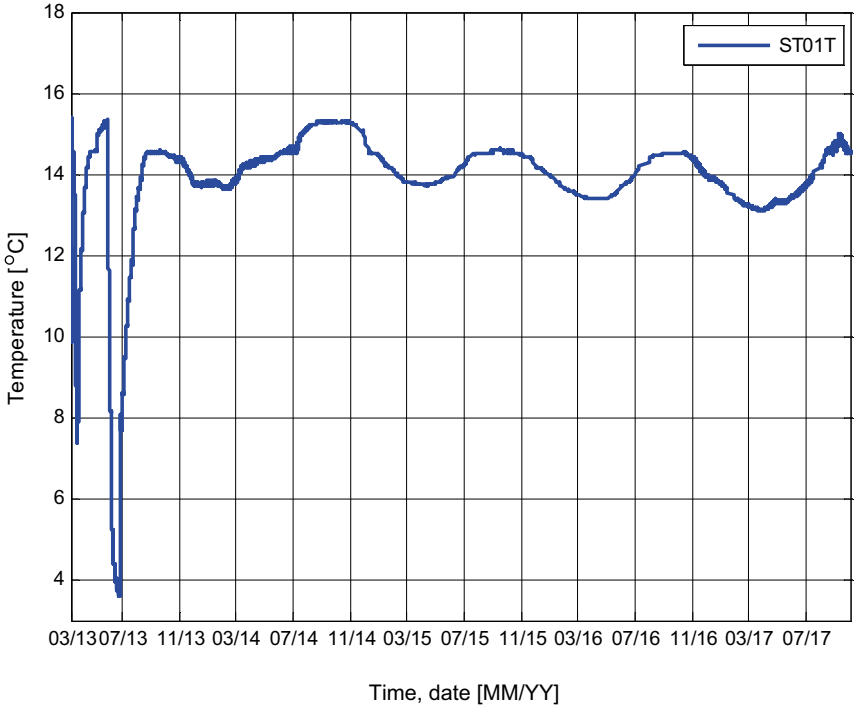

Figure A-1. *Temperature variation in the concrete dome, measured with sensor ST01T.*

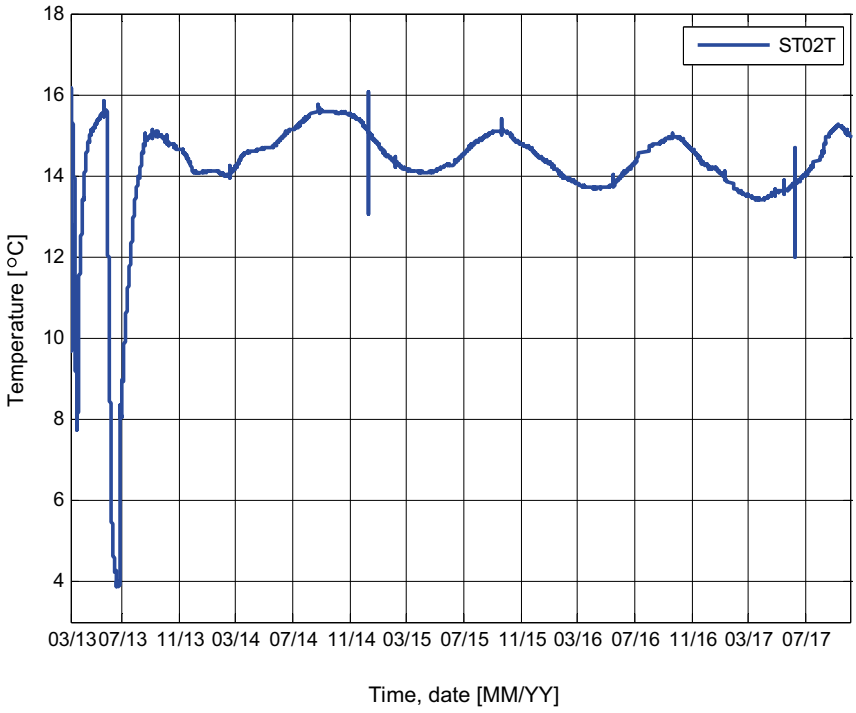

Figure A-2. *Temperature variation in the concrete dome, measured with sensor ST02T.*

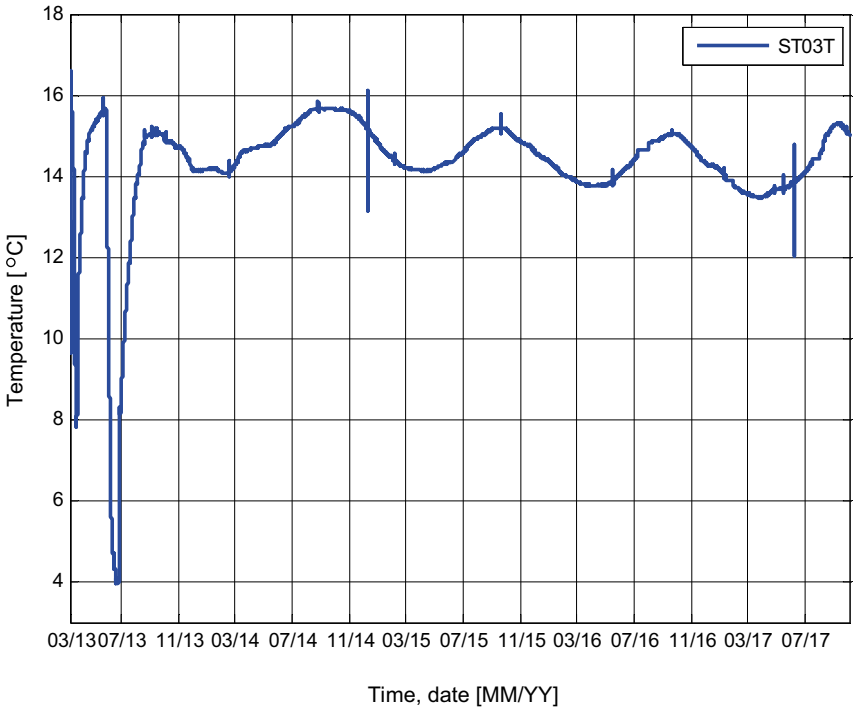

Figure A-3. *Temperature variation in the concrete dome, measured with sensor ST03T.*

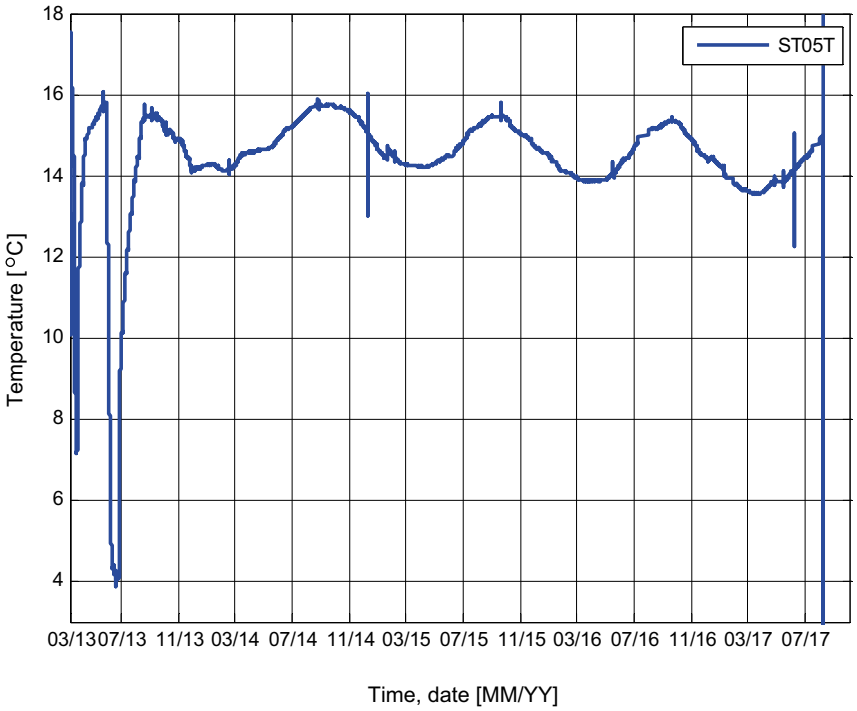

Figure A-4. *Temperature variation in the concrete dome, measured with sensor ST05T (failed during the pressure test).*

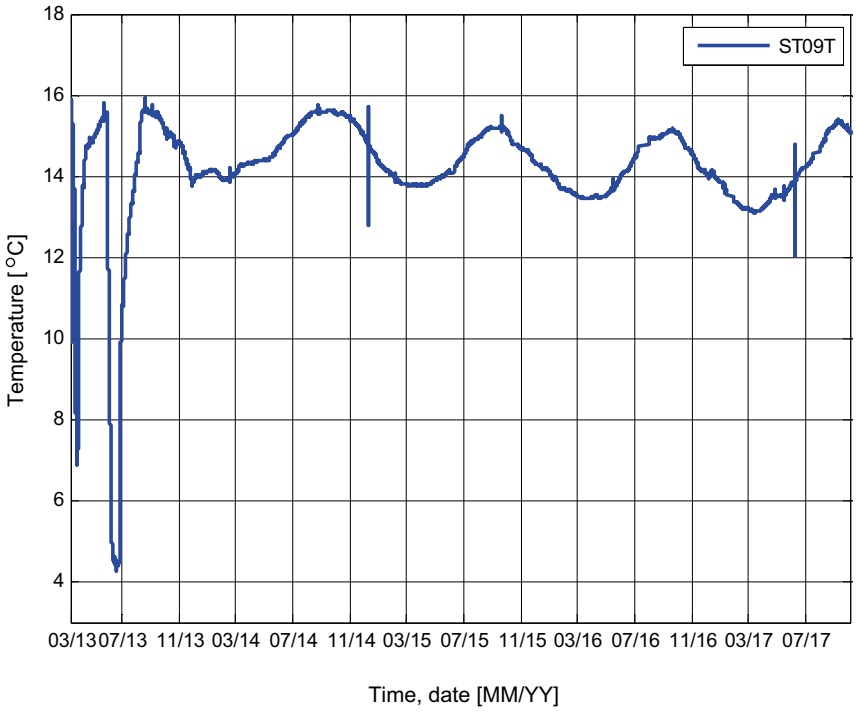

Figure A-5. *Temperature variation in the concrete dome, measured with sensor ST09T.*

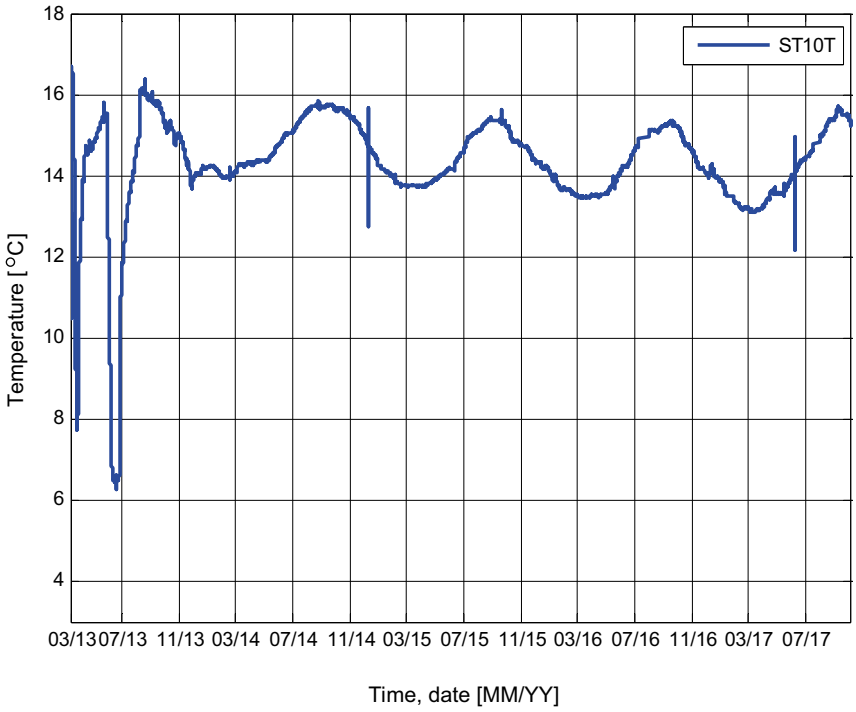

Figure A-6. *Temperature variation in the concrete dome, measured with sensor ST10T.*

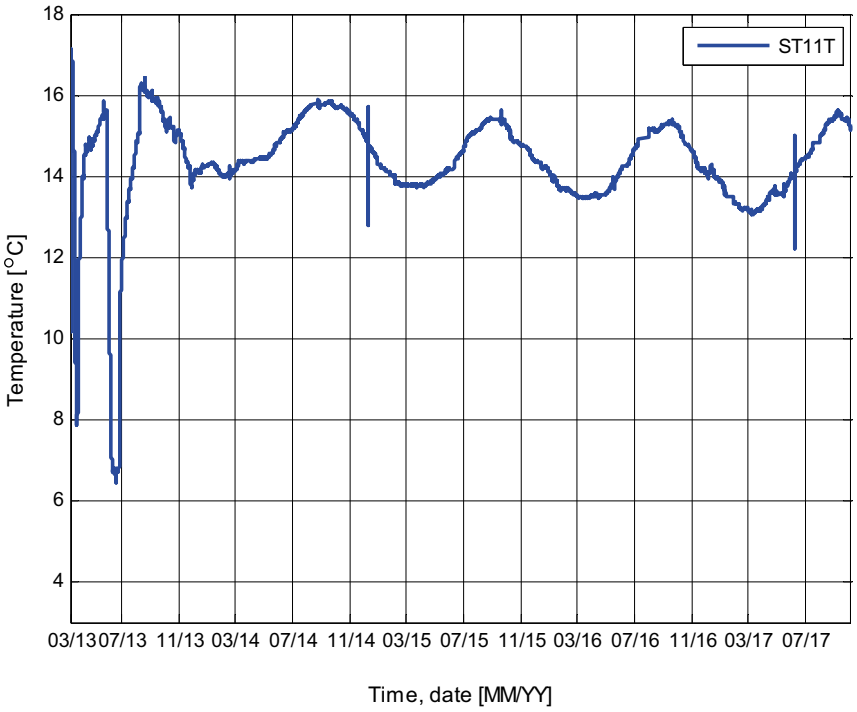

Figure A-7. *Temperature variation in the concrete dome, measured with sensor ST11T.*

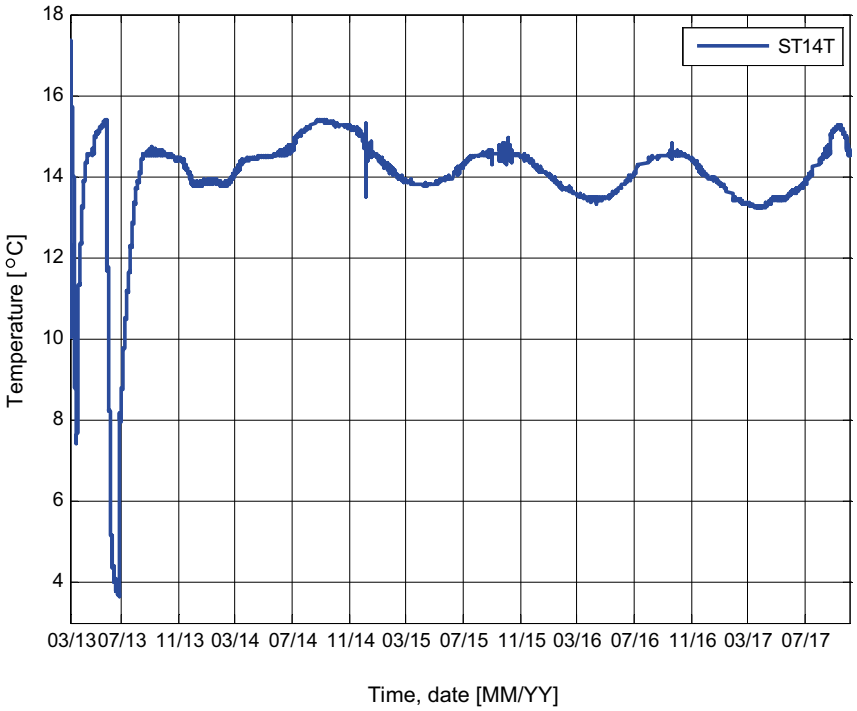

Figure A-8. *Temperature variation in the concrete dome, measured with sensor ST14T.*

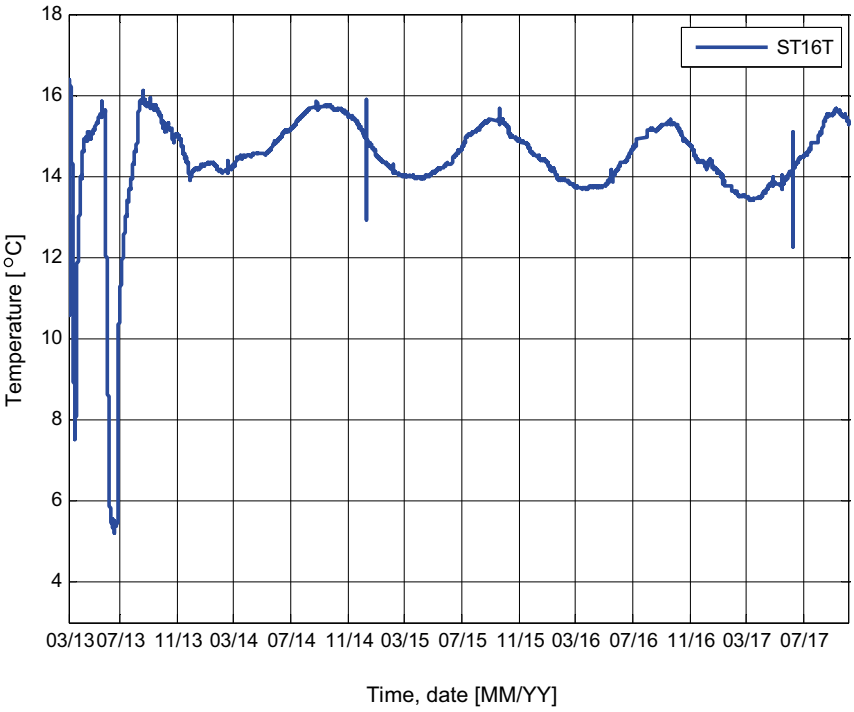

Figure A-9. *Temperature variation in the concrete dome, measured with sensor ST16T.*

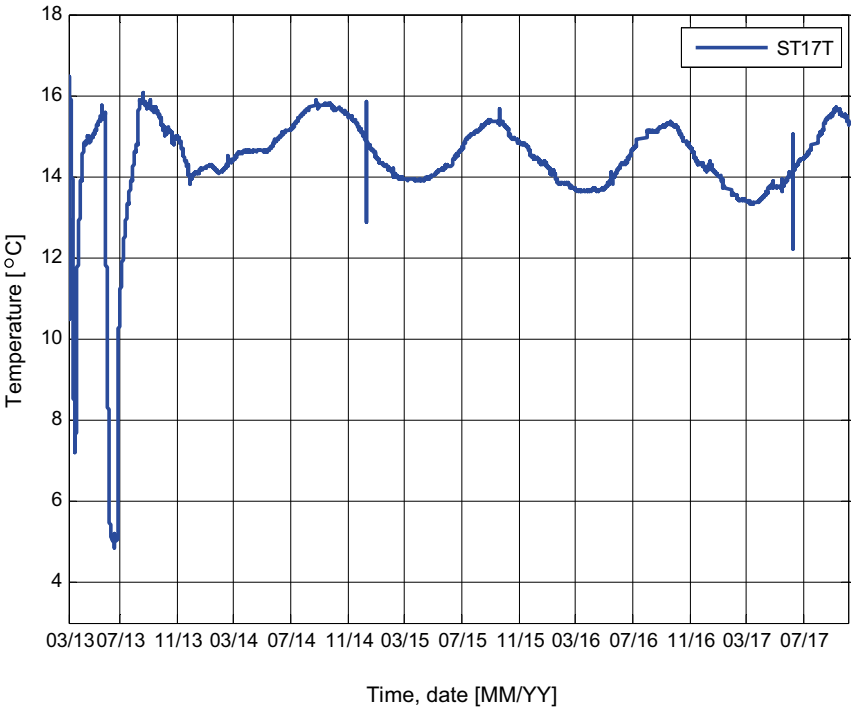

Figure A-10. *Temperature variation in the concrete dome, measured with sensor ST17T.*

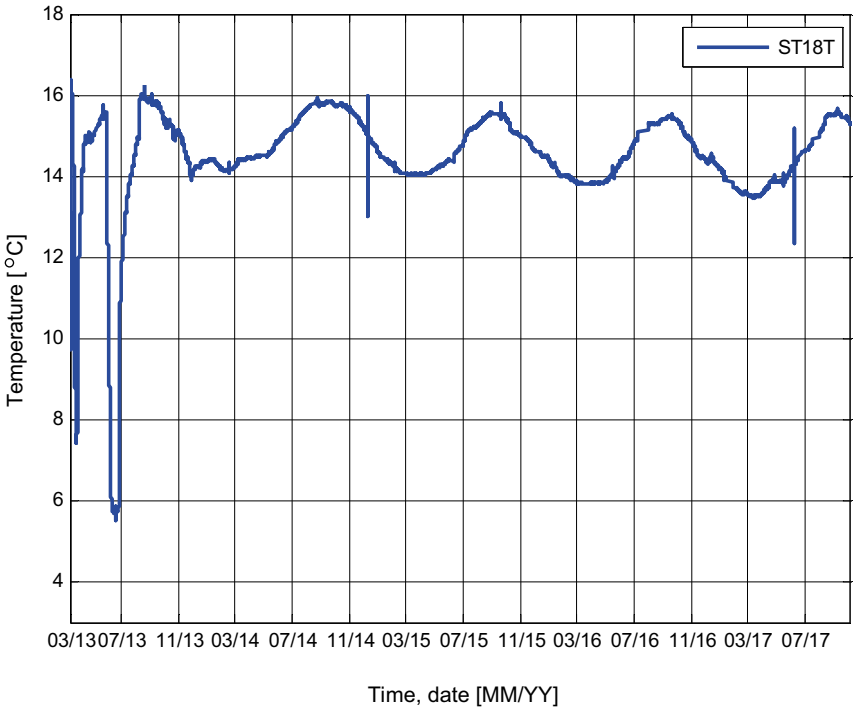

Figure A-11. *Temperature variation in the concrete dome, measured with sensor ST18T.*

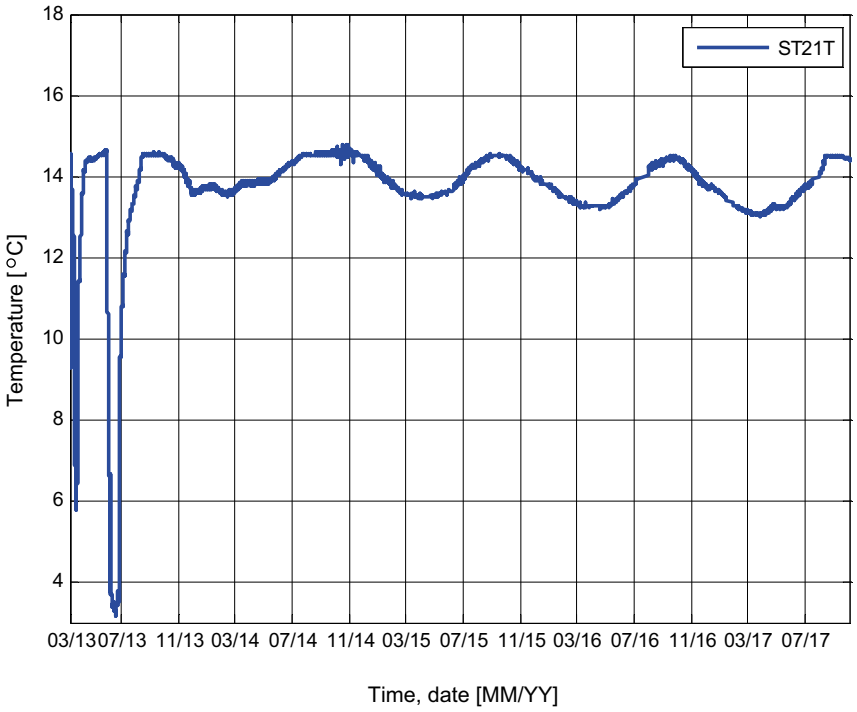

Figure A-12. *Temperature variation in the concrete dome, measured with sensor ST21T.*

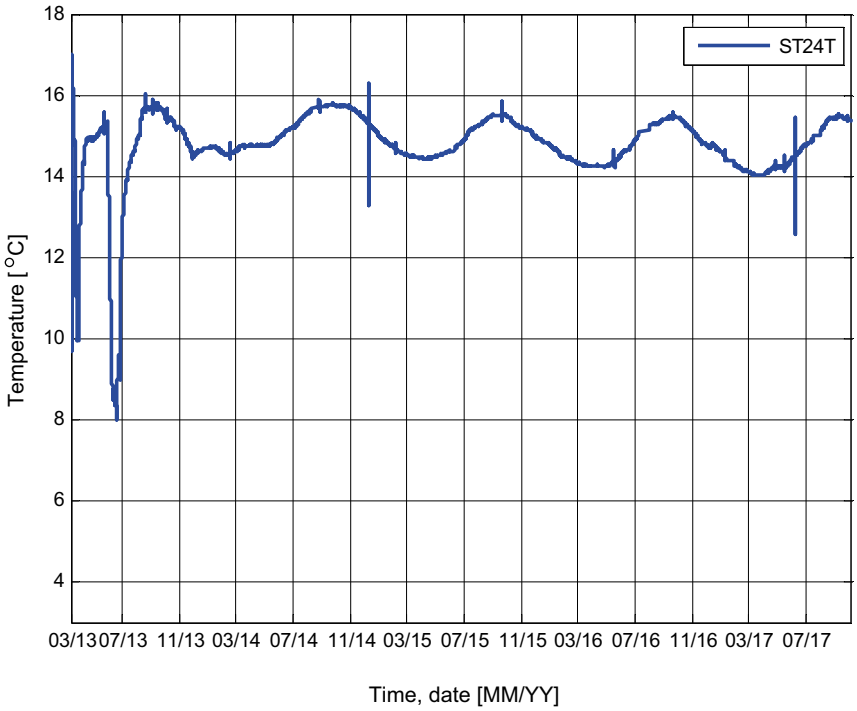

Figure A-13. *Temperature variation in the concrete dome, measured with sensor ST24T.*

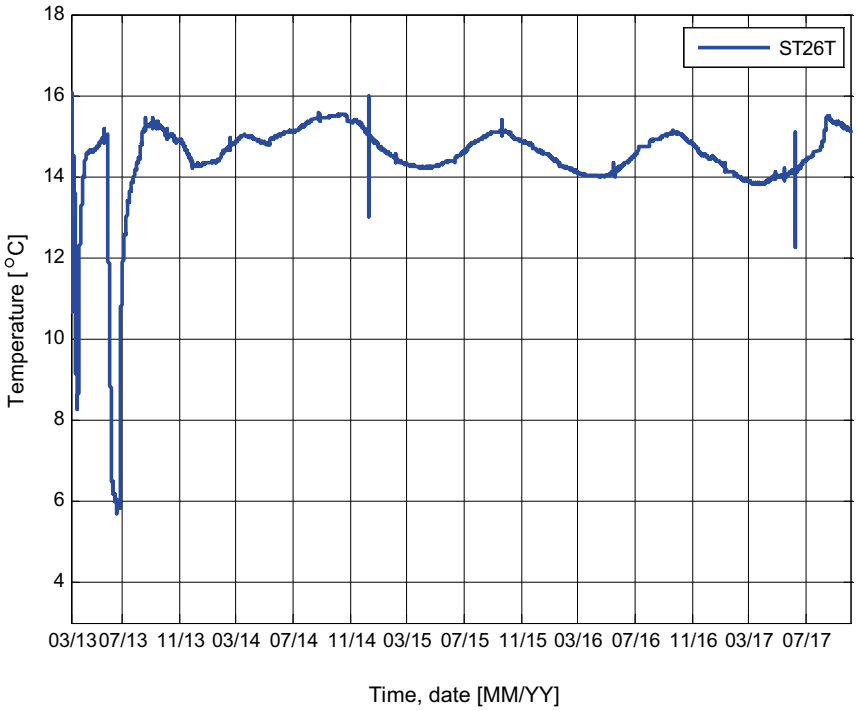

Figure A-14. *Temperature variation in the concrete dome, measured with sensor ST26T.*

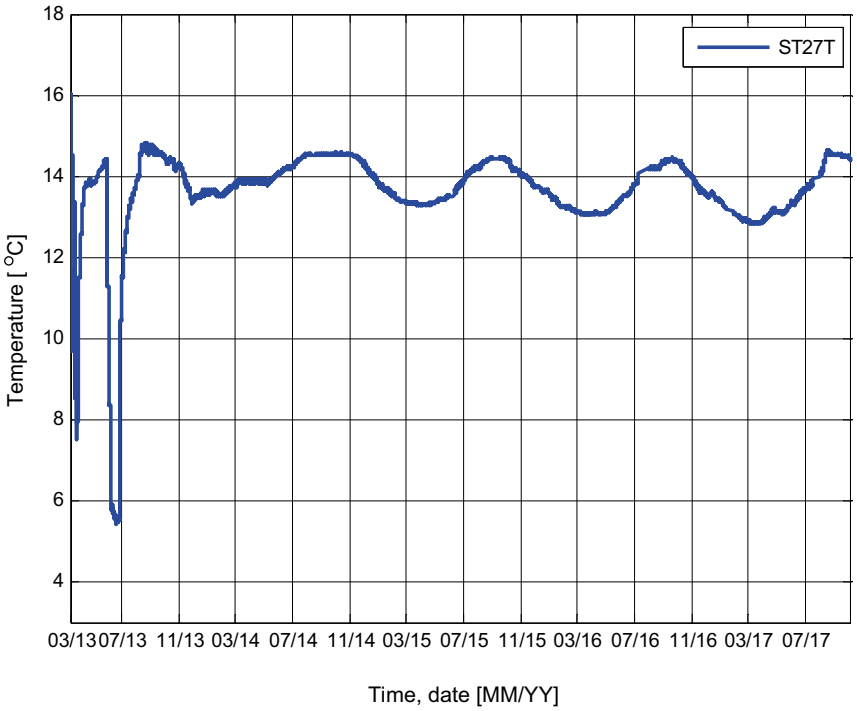

Figure A-15. *Temperature variation in the concrete dome, measured with sensor ST27T.*

A2 Strain

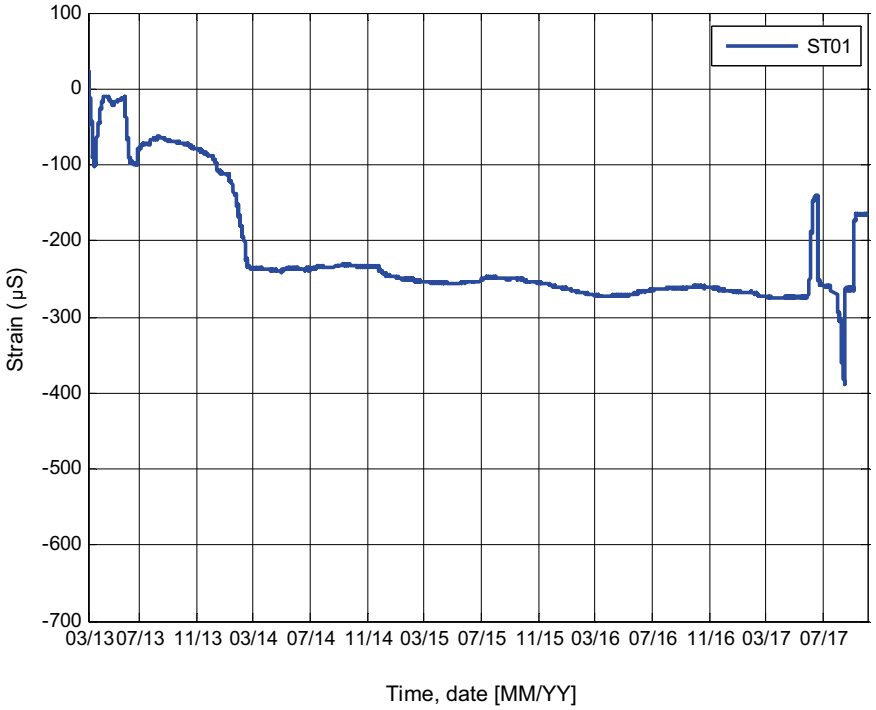

Figure A-16. *Variation in strain, measured with sensor ST01.*

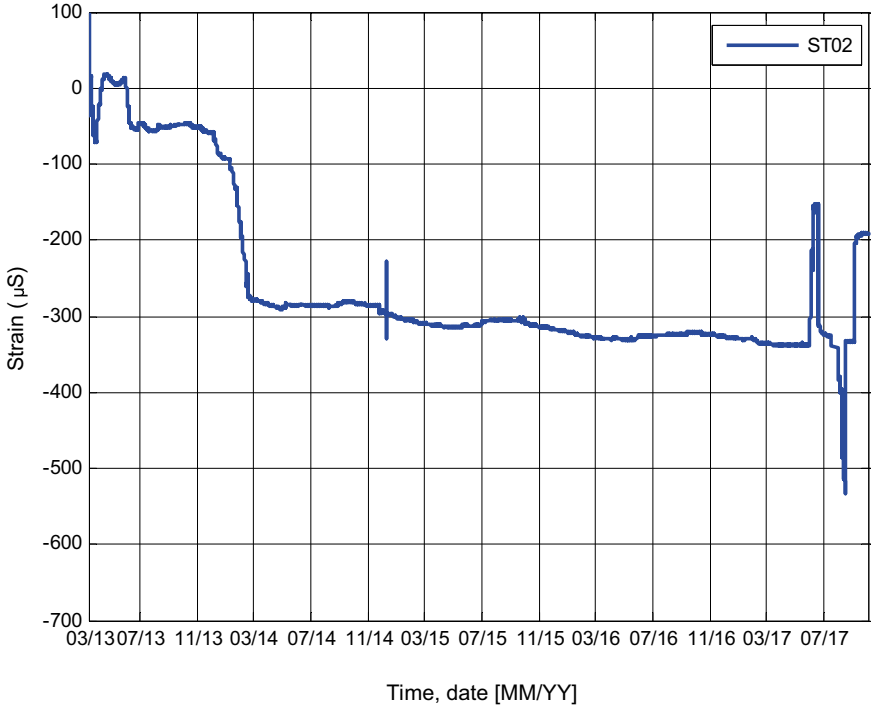

Figure A-17. *Variation in strain, measured with sensor ST02.*

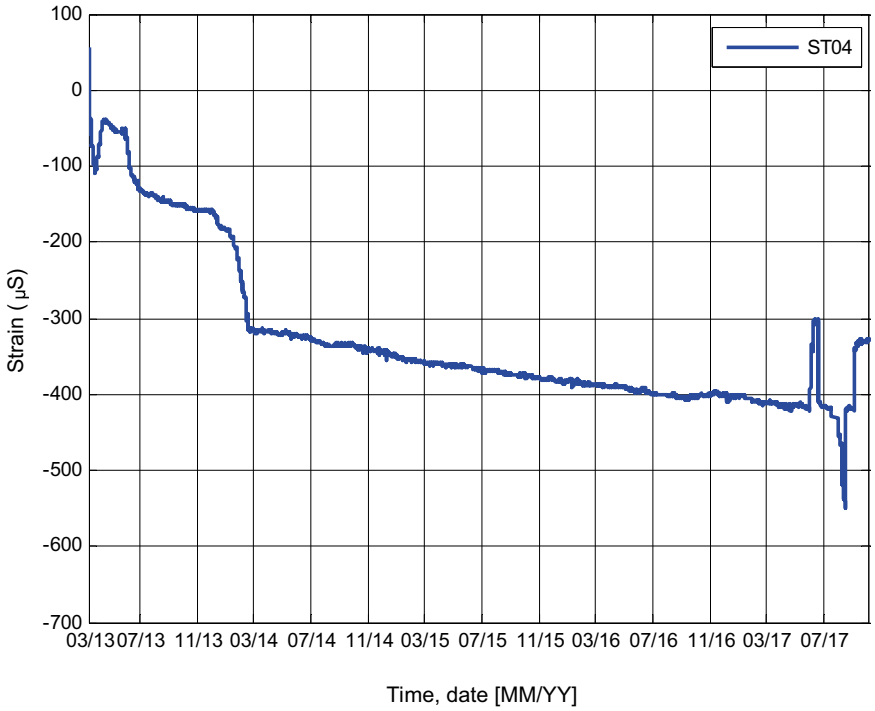

Figure A-18. *Variation in strain, measured with sensor ST04.*

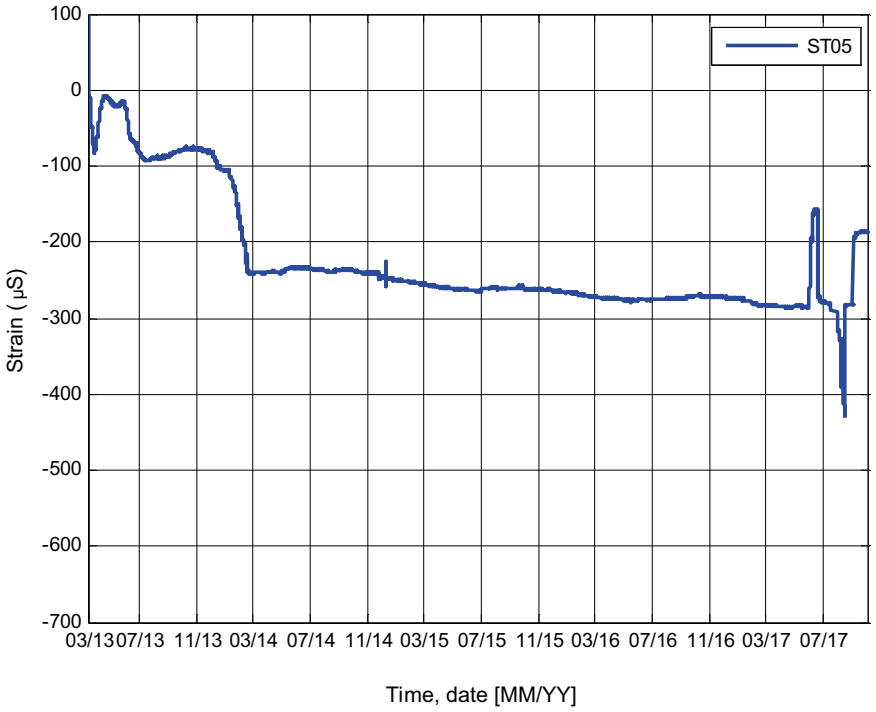

Figure A-19. *Variation in strain, measured with sensor ST05.*

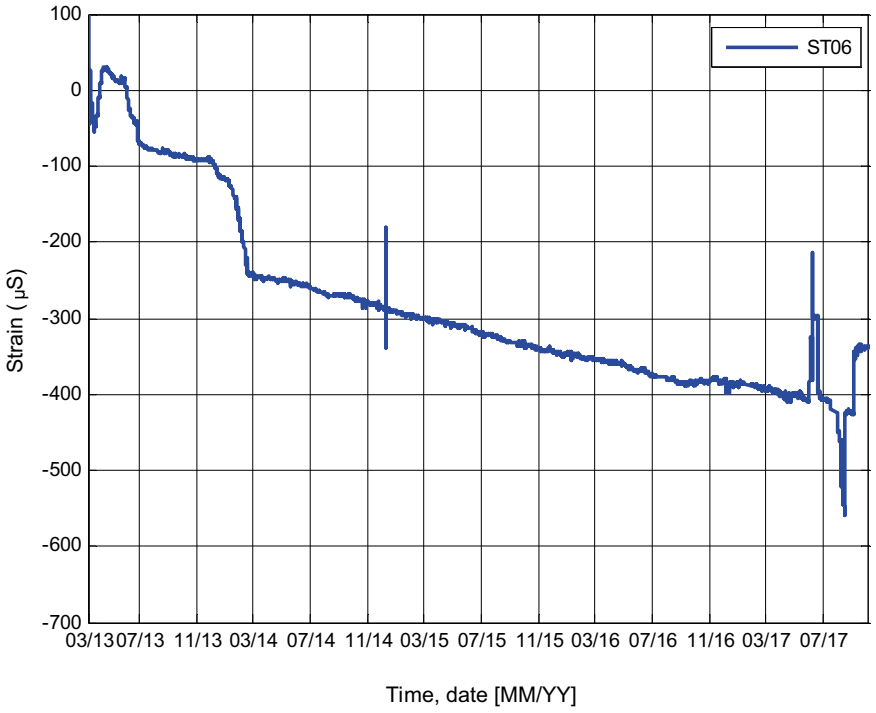

Figure A-20. *Variation in strain, measured with sensor ST06.*

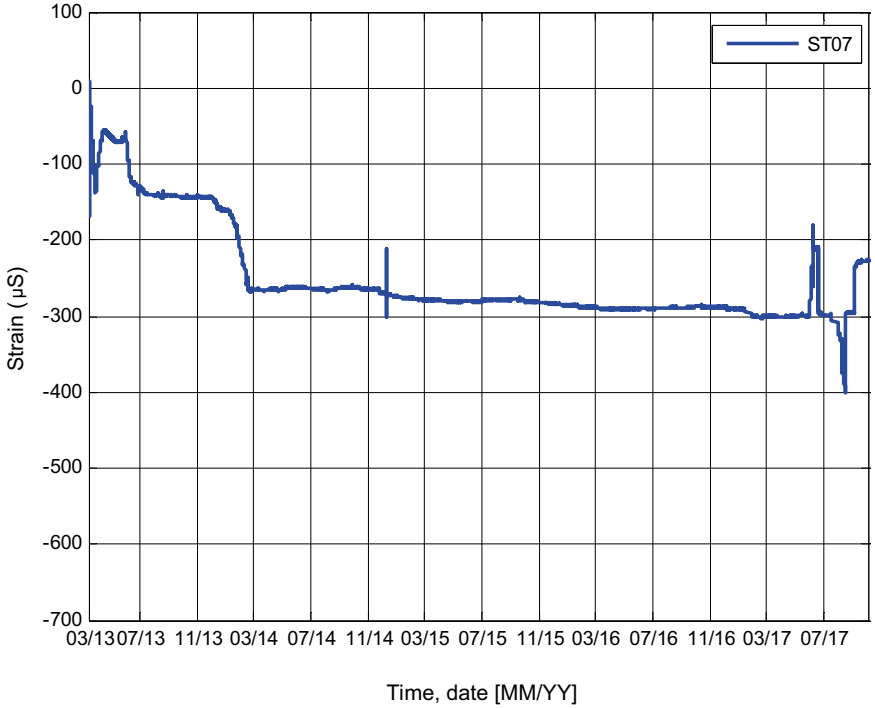

Figure A-21. *Variation in strain, measured with sensor ST07.*

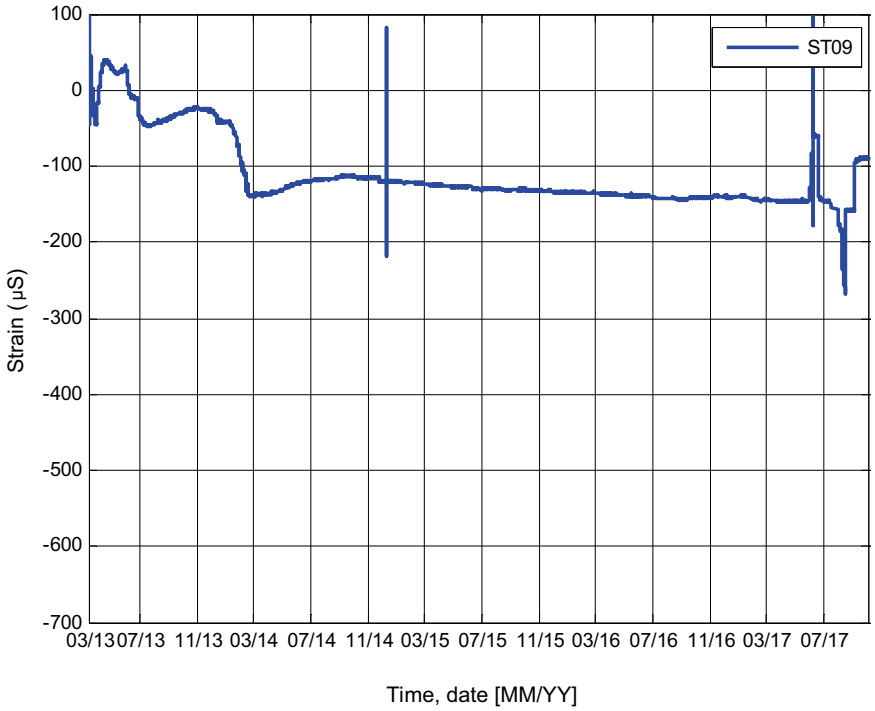

Figure A-22. *Variation in strain, measured with sensor ST09.*

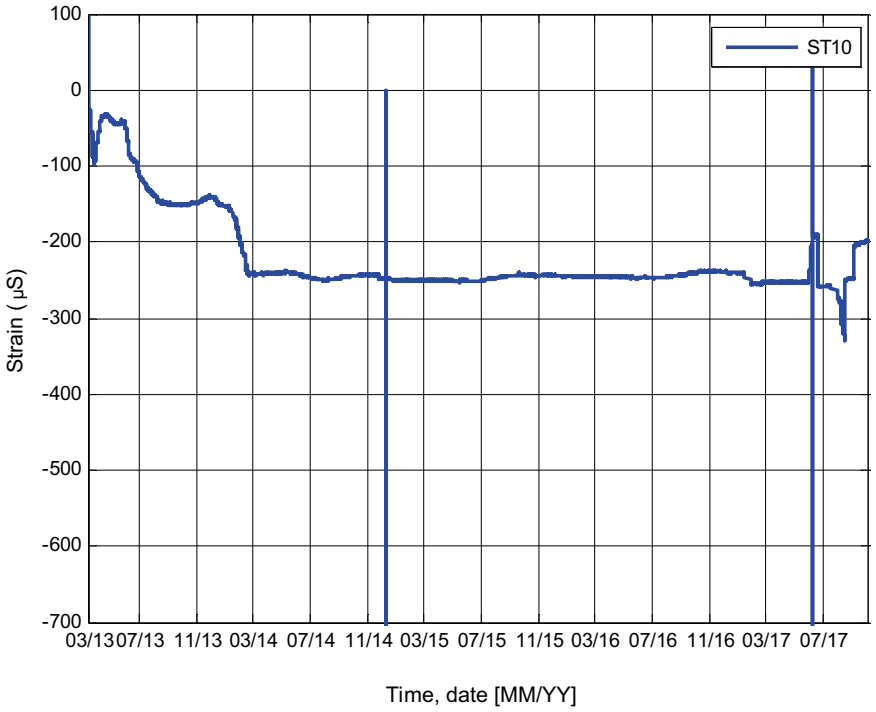

Figure A-23. *Variation in strain, measured with sensor ST10.*

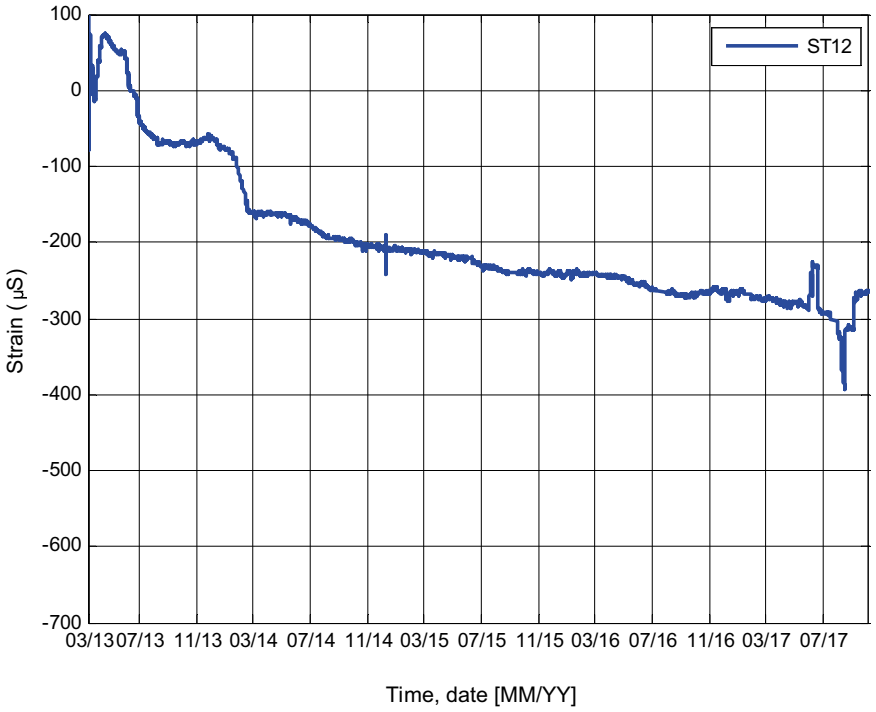

Figure A-24. *Variation in strain, measured with sensor ST12.*

Figure A-25. *Variation in strain, measured with sensor ST14.*

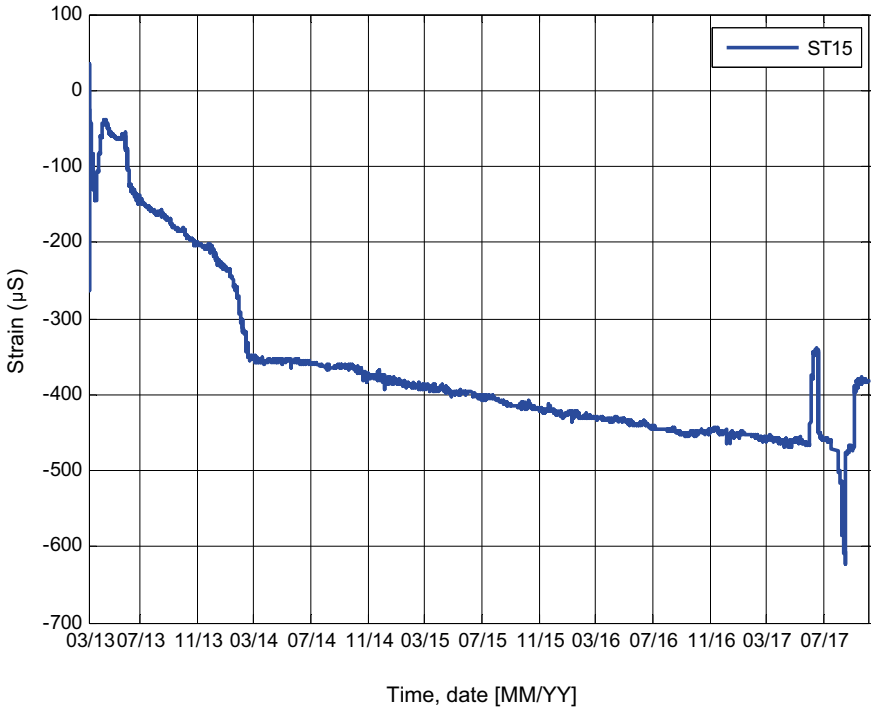

Figure A-26. *Variation in strain, measured with sensor ST15.*

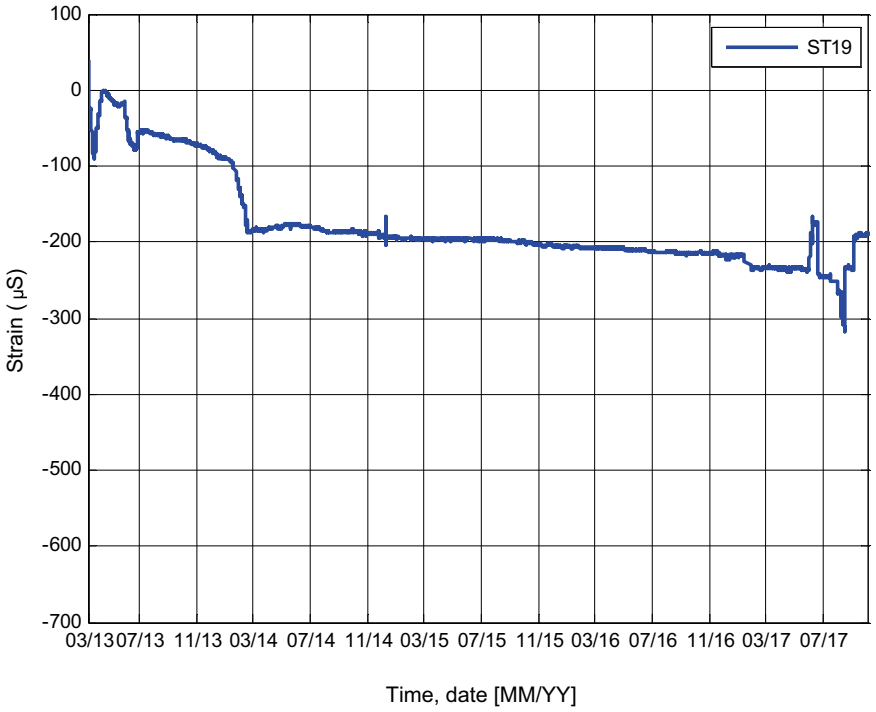

Figure A-27. *Variation in strain, measured with sensor ST19.*

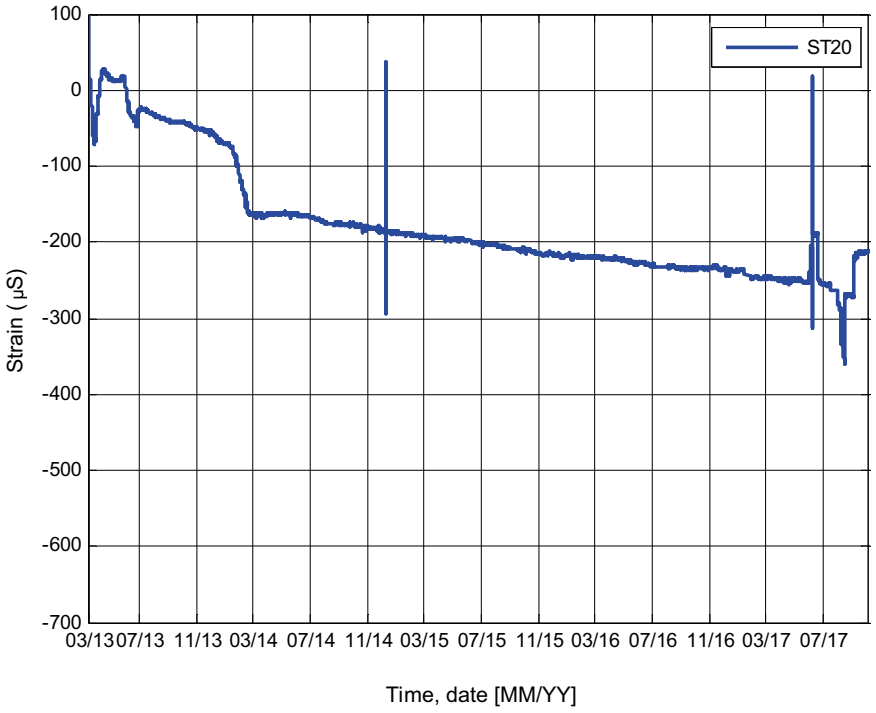

Figure A-28. *Variation in strain, measured with sensor ST20.*

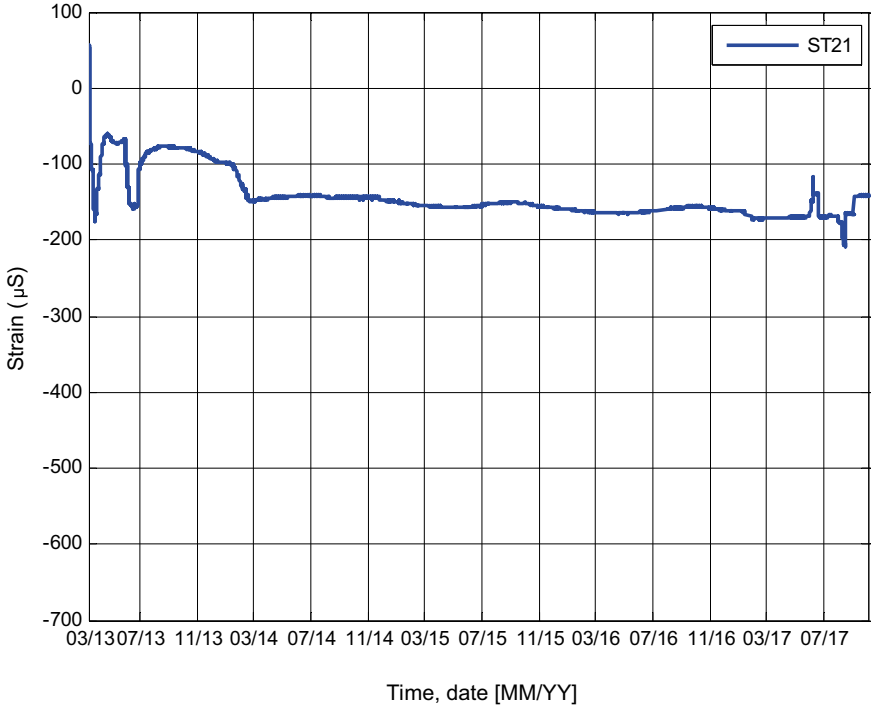

Figure A-29. *Variation in strain, measured with sensor ST21.*

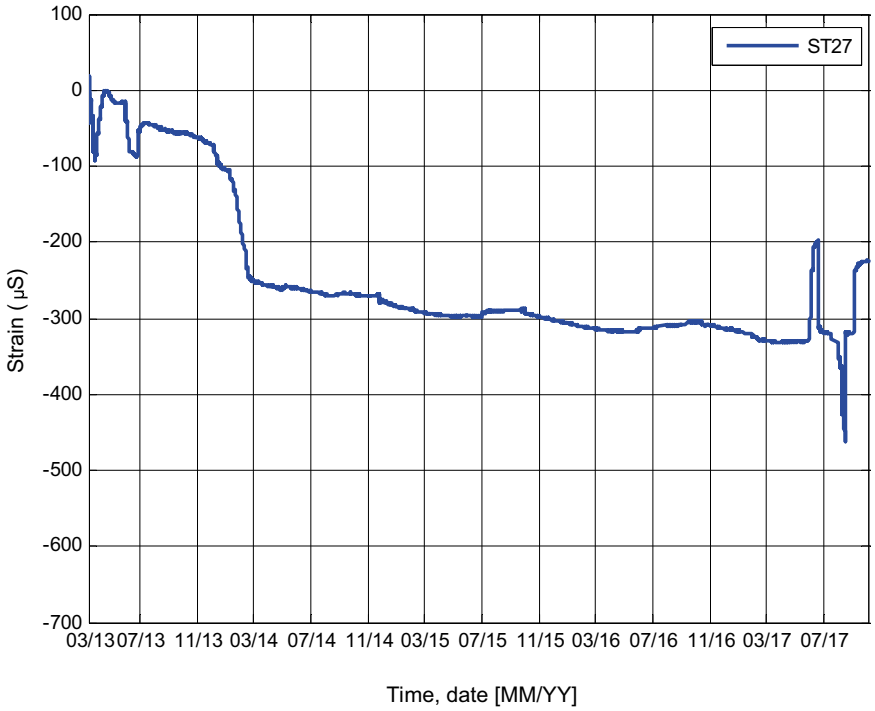

Figure A-30. *Variation in strain, measured with sensor ST27.*

A3 Relative displacement between concrete and rock

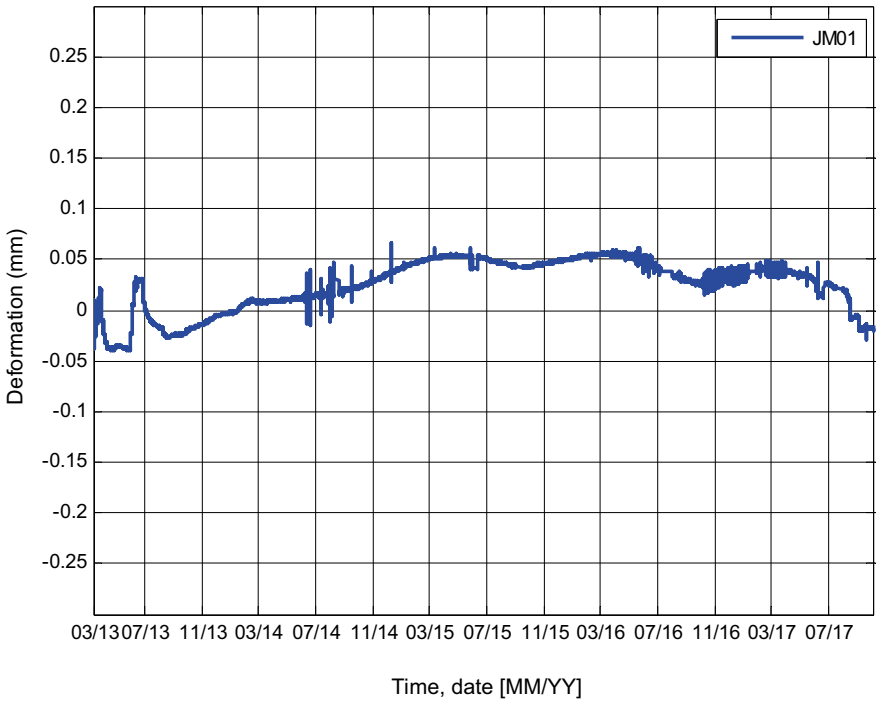

Figure A-31. *Variation in relative displacement, measured with JM01.*

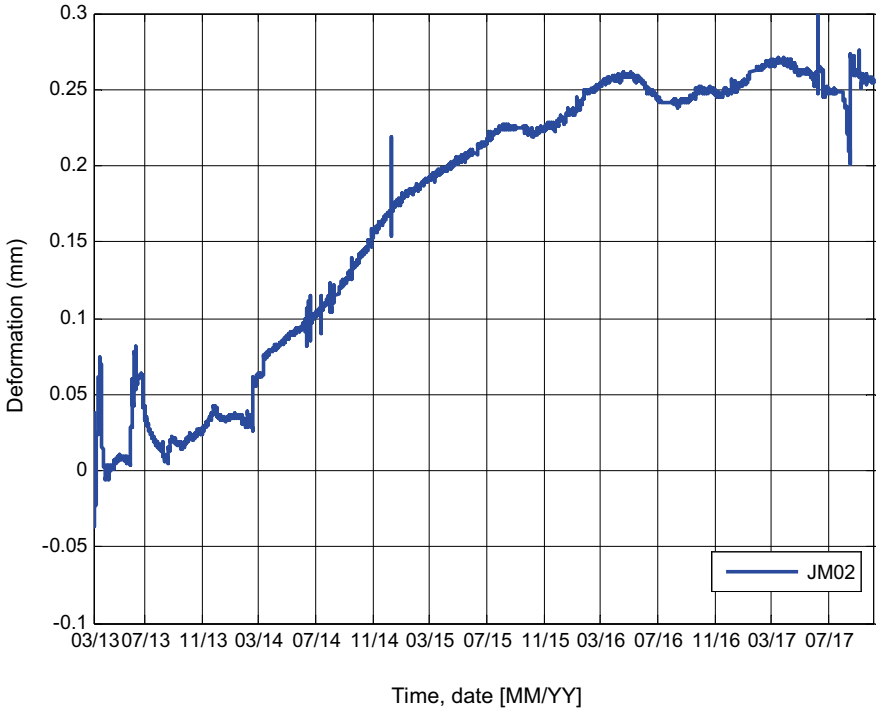

Figure A-32. *Variation in relative displacement, measured with JM02.*

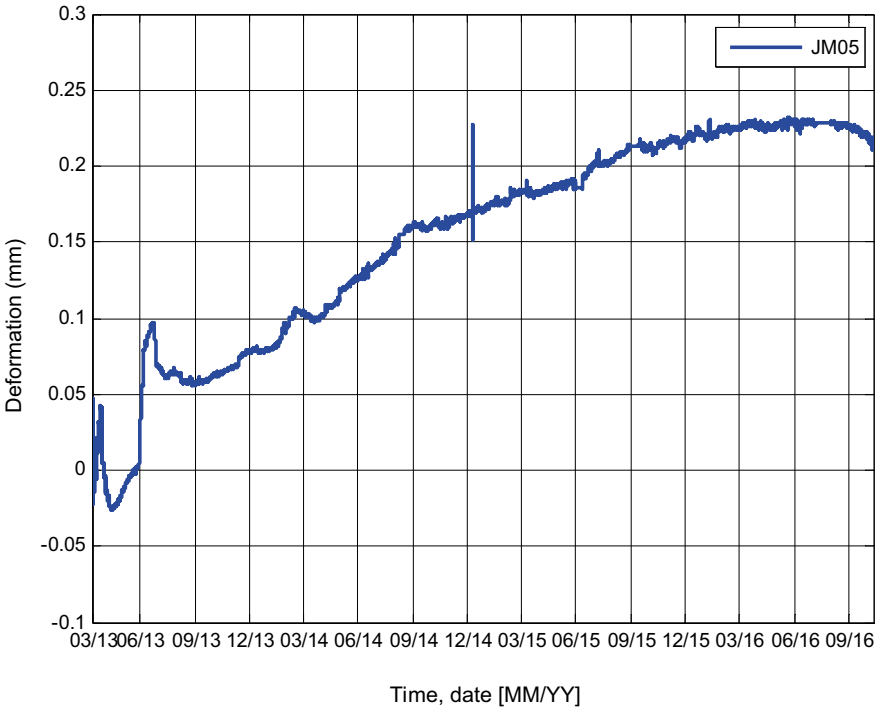

Figure A-33. *Variation in relative displacement, measured with JM05.*

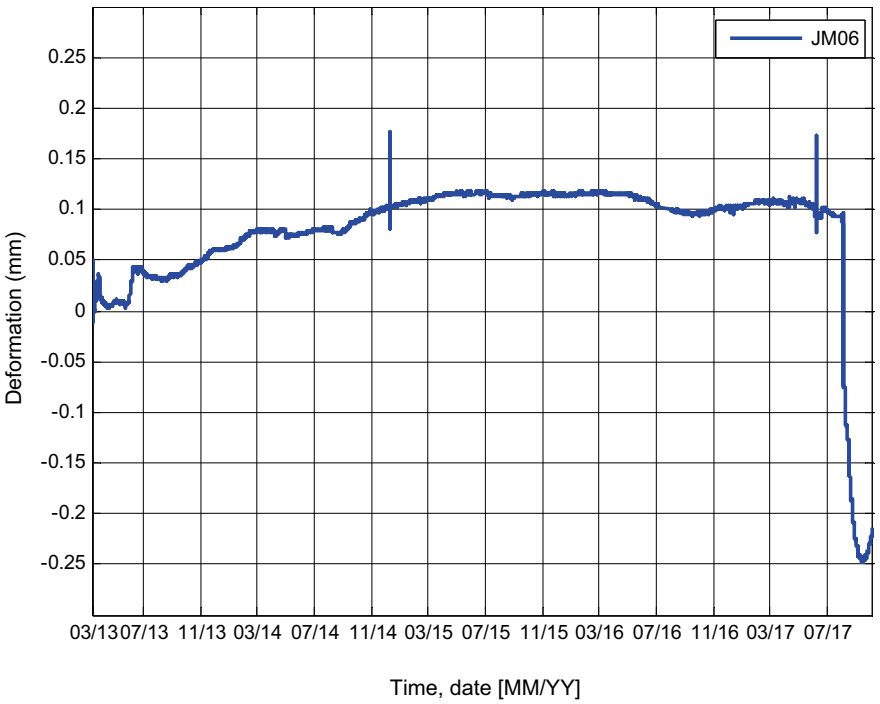

Figure A-34. *Variation in relative displacement, measured with JM06.*

Appendix B

Comparison between FE-simulations and measurements

B1 Strain

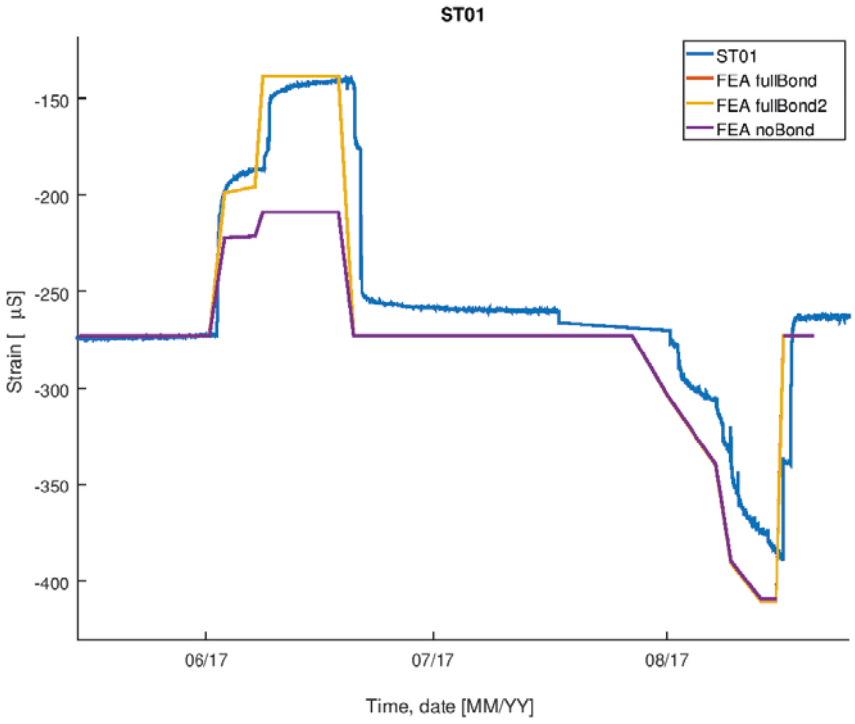

Figure B-1. *Comparison between strain gauge ST01 and FE-simulations.*

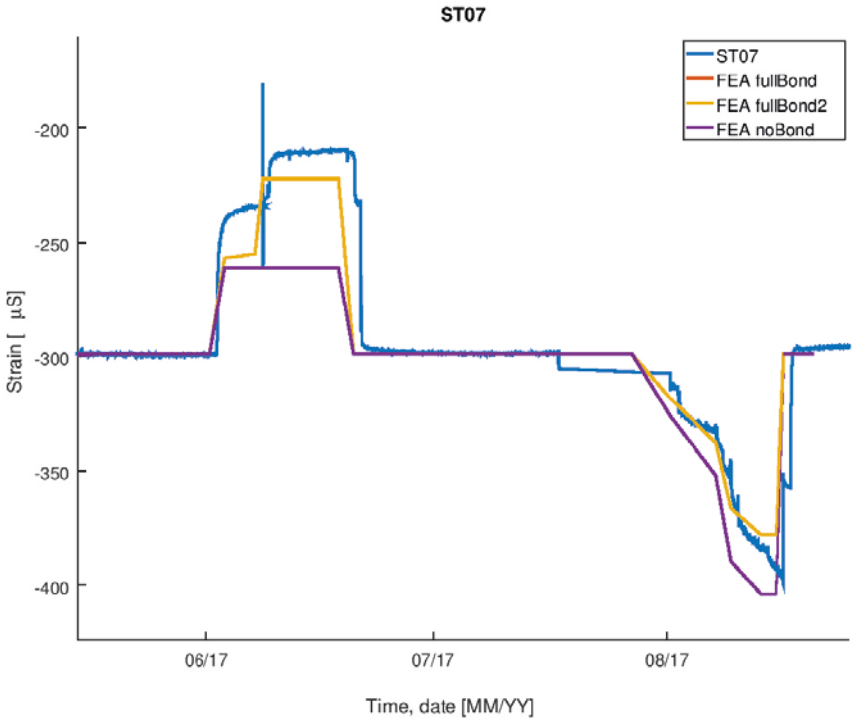

Figure B-2. *Comparison between strain gauge ST07 and FE-simulations.*

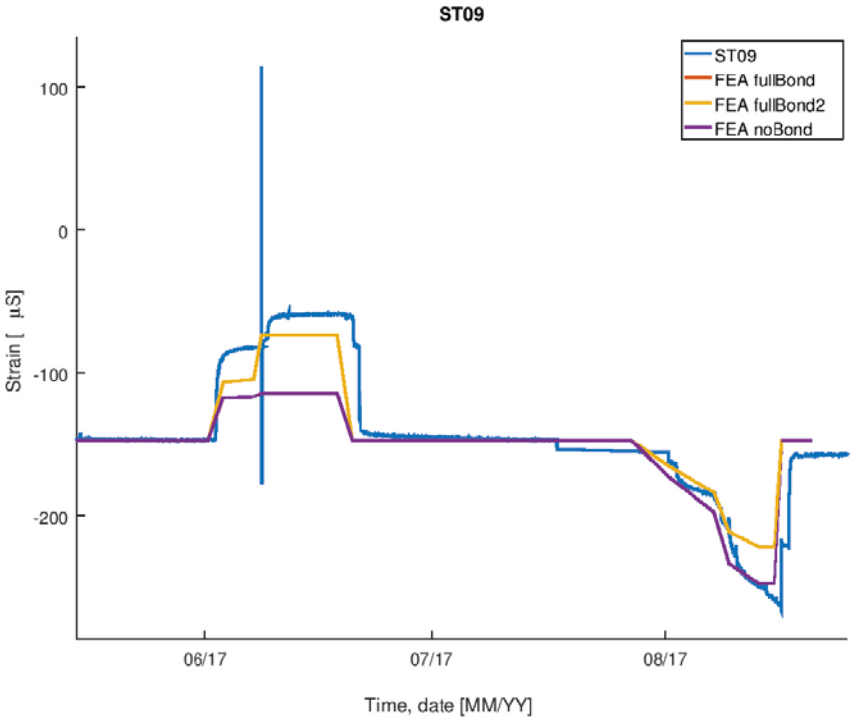

Figure B-3. *Comparison between strain gauge ST09and FE-simulations.*

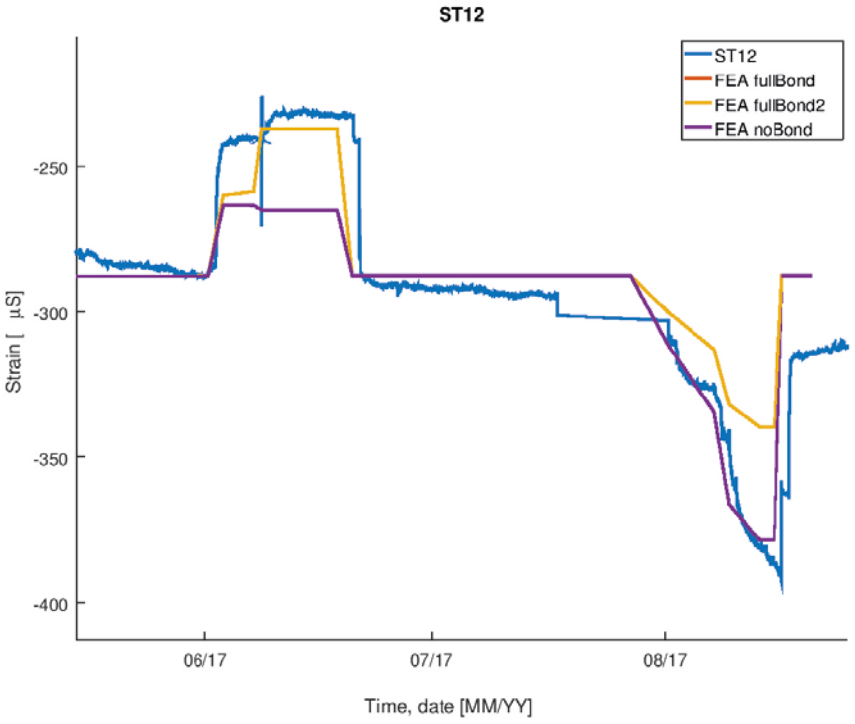

Figure B-4. *Comparison between strain gauge ST12 and FE-simulations.*

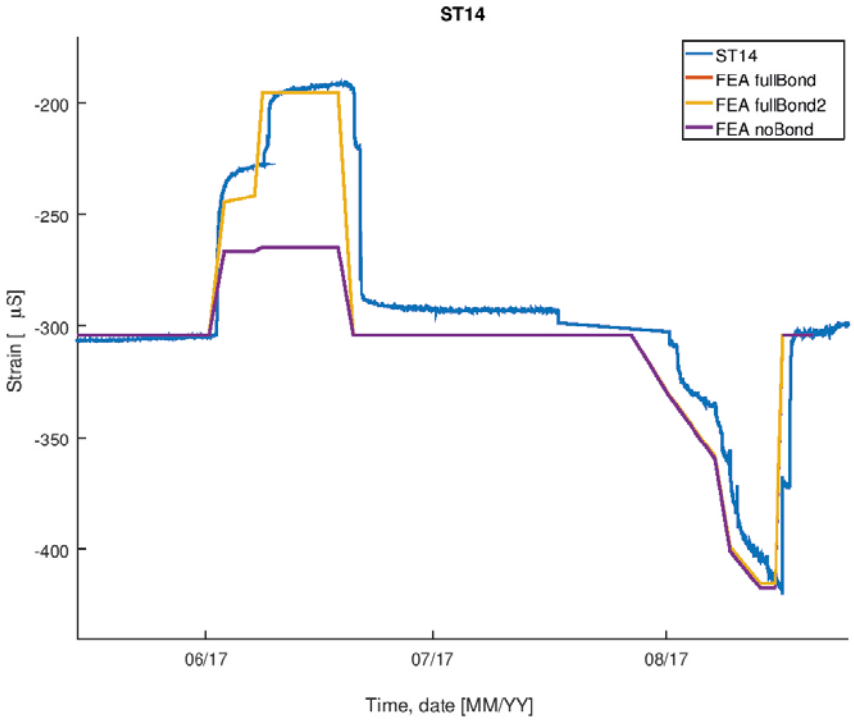

Figure B-5. *Comparison between strain gauge ST14 and FE-simulations.*

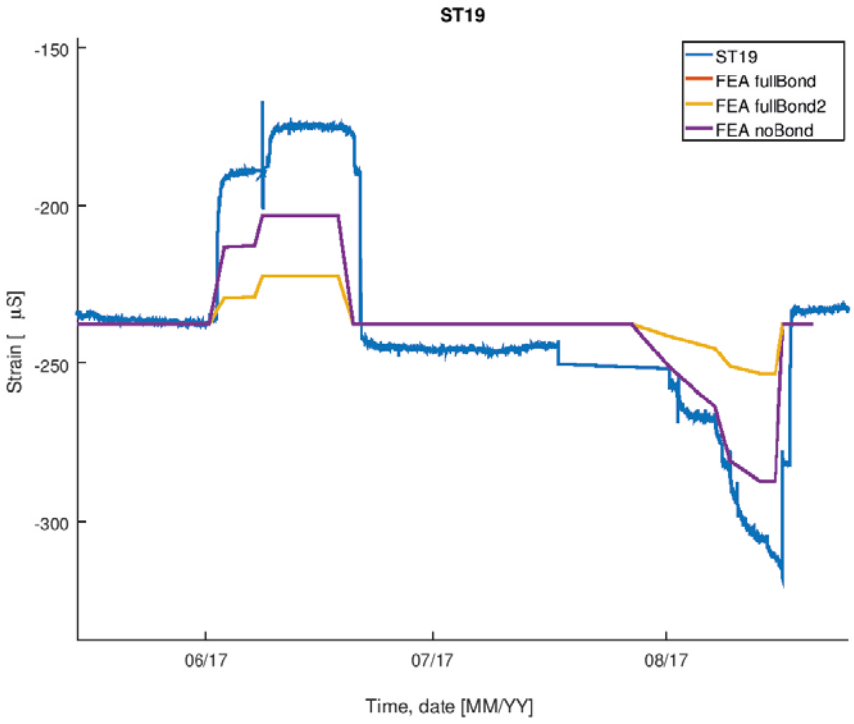

Figure B-6. *Comparison between strain gauge ST19 and FE-simulations.*

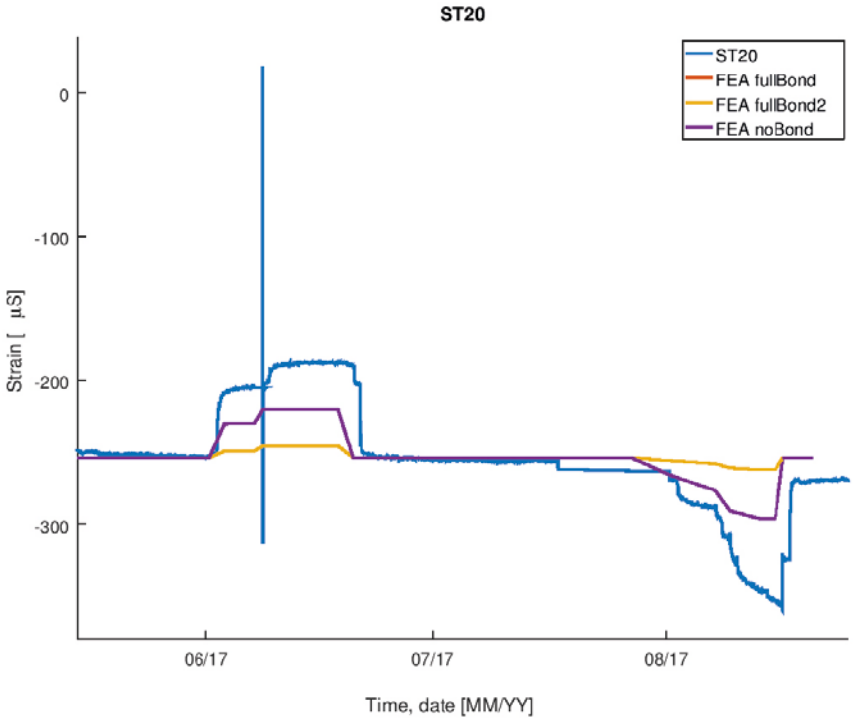

Figure B-7. *Comparison between strain gauge ST20 and FE-simulations.*

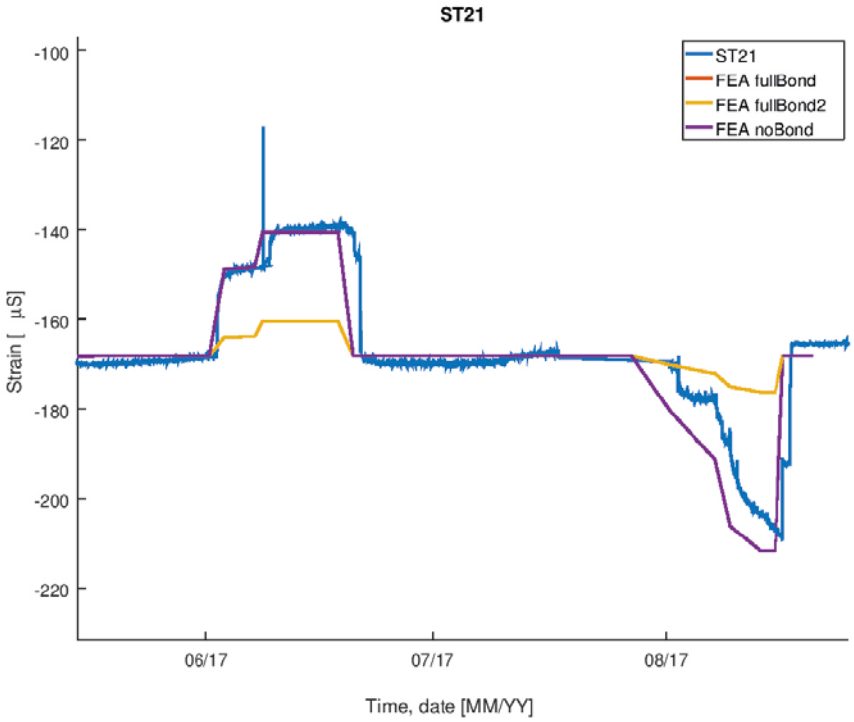

Figure B-8. *Comparison between strain gauge ST21 and FE-simulations.*

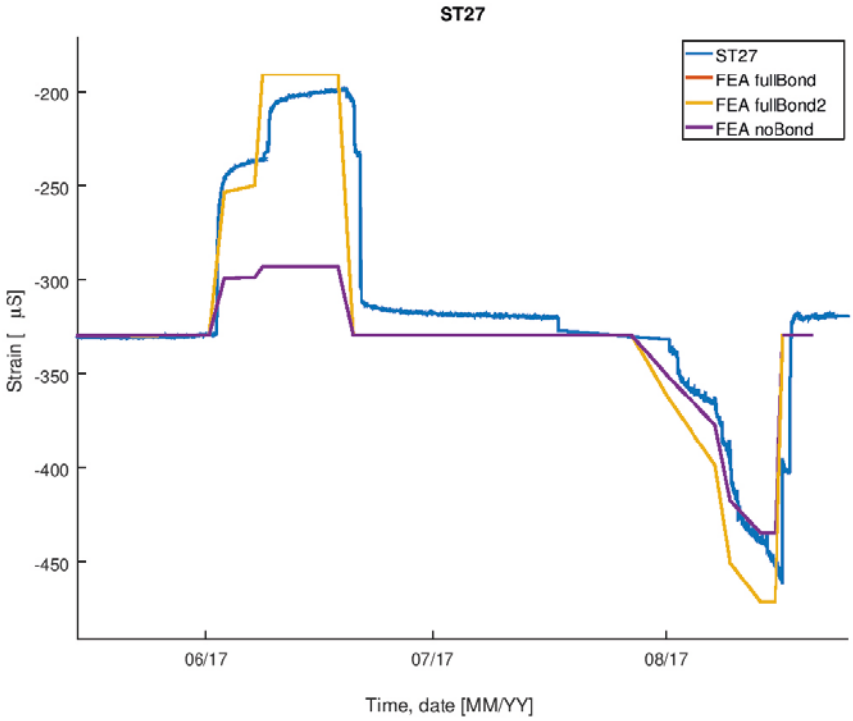

Figure B-9. *Comparison between strain gauge ST27 and FE-simulations.*

B2 LVDT

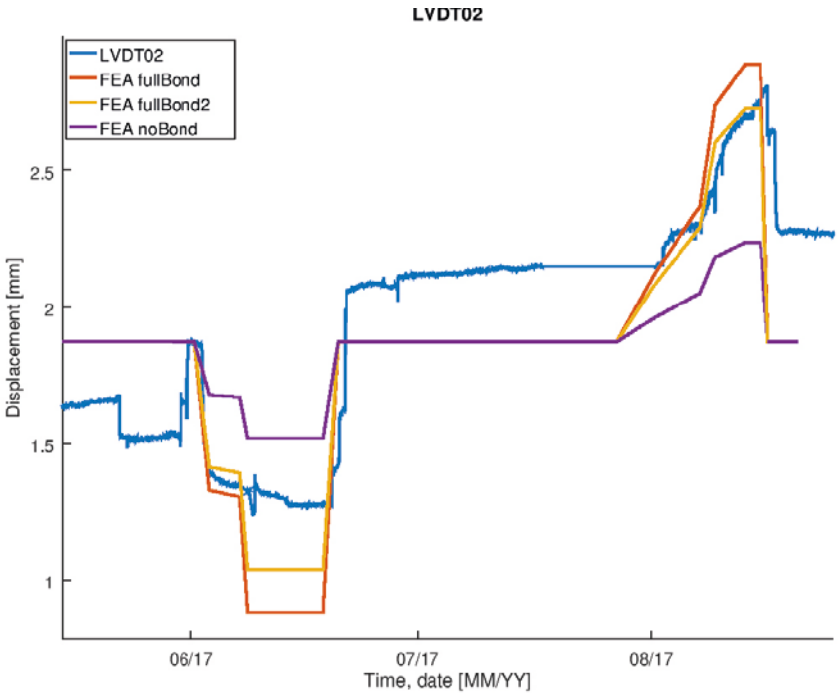

Figure B-10. *Comparison between LVDT-sensor LVDT02 and FE-simulations.*

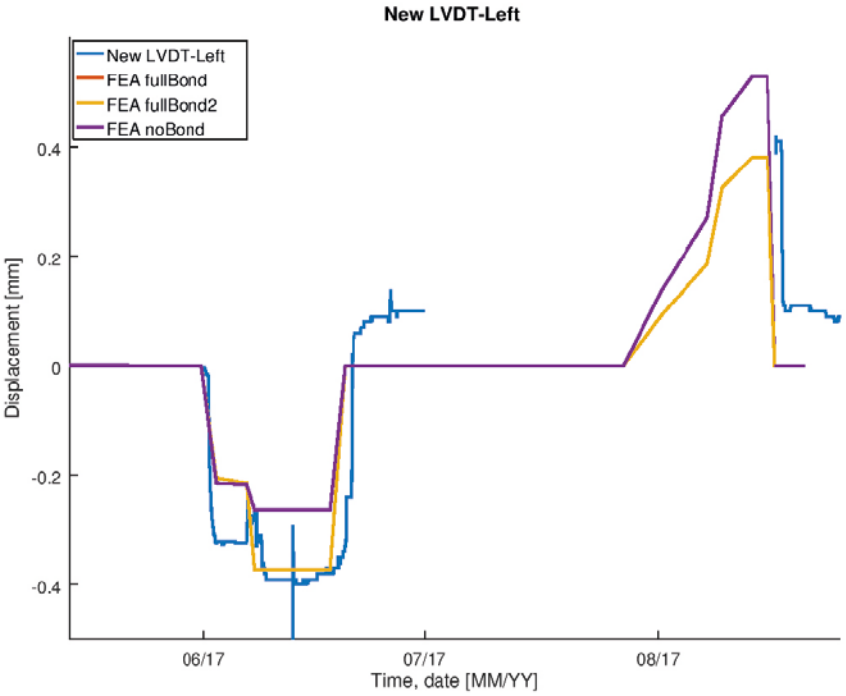

Figure B-11. *Comparison between LVDT-sensor LVDT-Left and FE-simulations.*

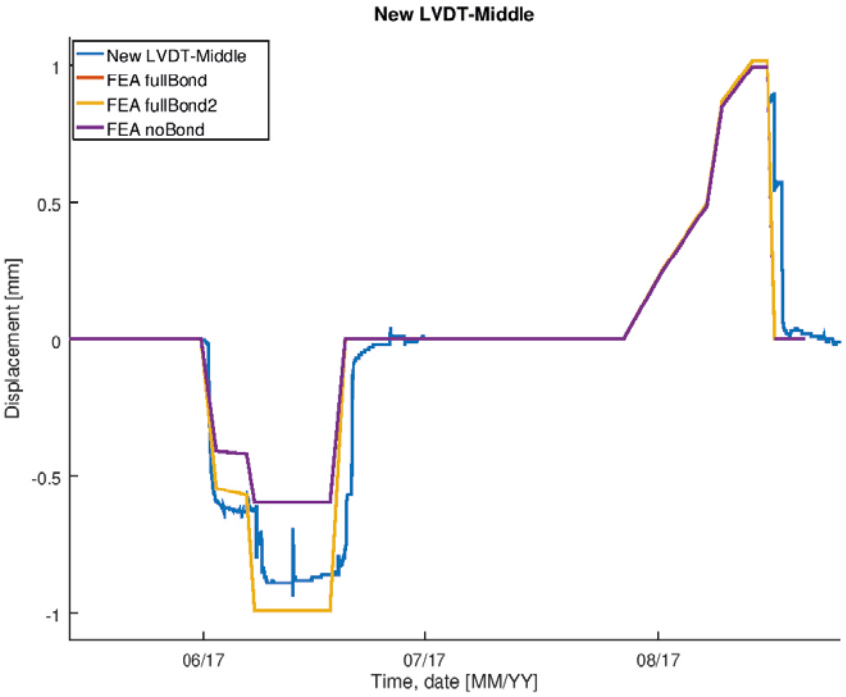

Figure B-12. *Comparison between LVDT-sensor LVDT-Middle and FE-simulations.*

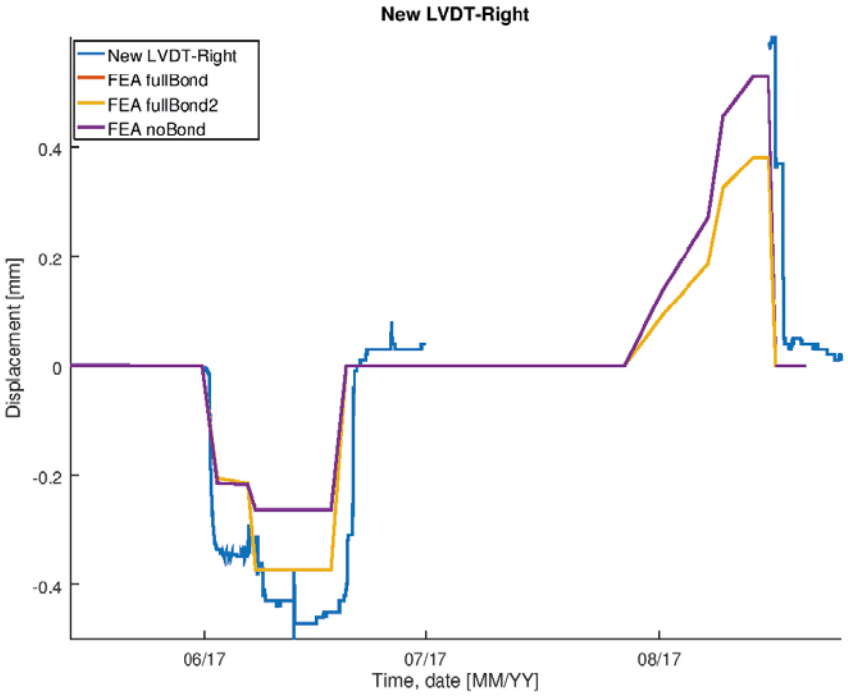

Figure B-13. *Comparison between LVDT-sensor LVDT-Right and FE-simulations.*

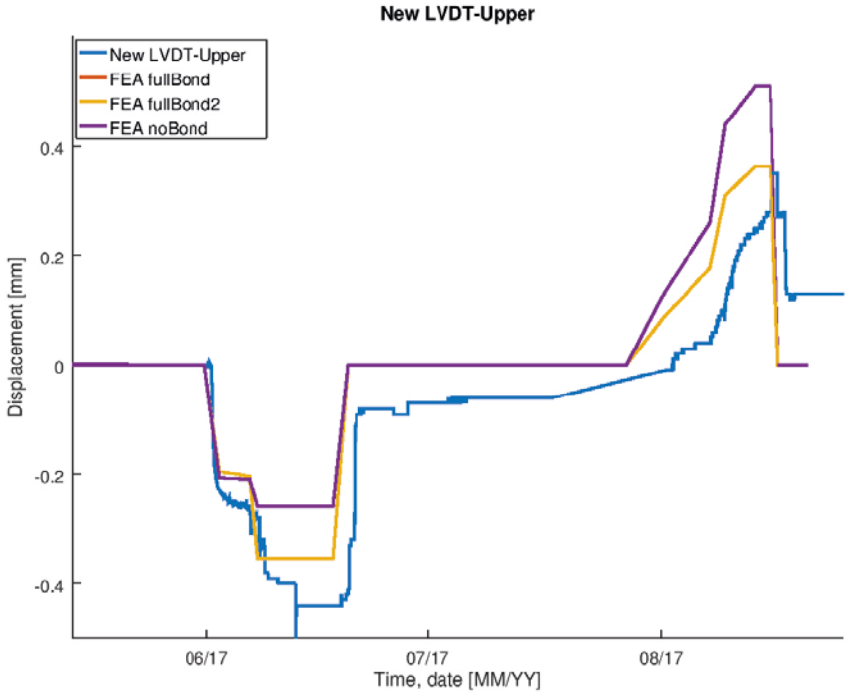

Figure B-14. *Comparison between LVDT-sensor LVDT-Upper and FE-simulations.*

Arkitektkopia AB, Bromma, 2019

SKB is responsible for managing spent nuclear fuel and radioactive waste produced by the Swedish nuclear power plants such that man and the environment are protected in the near and distant future.

skb.se